High Pressure Surface Plasmon Spectroscopy

Dissertation zur Erlangung des Grades

„Doktor der Naturwissenschaften"

am Fachbereich

Chemie und Pharmazie der

Johannes Gutenberg - Universität Mainz

vorgelegt von

Thomas Jakob

geboren in Bayreuth

Mainz, 2002

Contents

1. Introduction

In thermodynamics pressure is the complementary quantity to temperature. For example, both, temperature and pressure can trigger the volume phase transition occurring in N-isopropylacrylamide gels [1]. Some technically important processes like the liquefaction of gases even rely on a combination of temperature and pressure changes. Another example from industry is the extraction of caffeine from coffee beans or tea by means of supercritical carbon dioxide [2], a phase that exists only above 31 °C and 7.4 MPa. In general, pVT phase diagrams play an important role in the selection of materials where specific properties are of interest. However, pVT diagrams that describe the bulk characteristics of materials are not reliable when considering thin coatings. Since the number of molecules at an interface is not negligible anymore the actual geometry of the adjacent surfaces influences the thermodynamic behaviour of the thin film to a great extent. For example, the glass transition temperature of thin polymer films is substantially lowered as compared to the corresponding bulk material [3]. Here, technical and scientific research interests coincide. The modification of surfaces by means of thin polymer layers is essential in the fabrication of e.g. compact discs or in the processing of microchips. Thin lubricant layers prevent the sensor tip of a hard disc to crash onto the spinning magnetic disc; thus a more reliable operation and higher storage capacities can be obtained as the tip can be adjusted closer to the surface.

In order to further develop and characterise thin dielectric films methods have to be applied that are sensitive to changes in the properties of such layers systems. Within this context, surface plasmon resonance and waveguide spectroscopy provide a sensitive tool to probe the optical properties of thin films. Both methods make use of evanescent waves that are restricted to an interface. The former method takes advantage of the interaction of light with the quasi-free electrons in a metal. The resulting electromagnetic field is confined to the vicinity of the metal surface. If the optical properties of the dielectric

adjacent to the metal change the evanescent field will be altered. This change can be monitored, which makes surface plasmon spectroscopy especially sensitive to processes close to metallic surfaces. In waveguide spectroscopy light is guided under certain conditions in an optical medium with higher refractive index than the material surrounding it. At the interface its evanescent field interacts with the molecules of the second medium. Here, the boundary conditions vary when the optical properties of the second material change. Therefore, the light coupled out from the waveguide can be used to monitor e.g. binding reactions of molecules to the surface of the waveguide.

The aim of this study is to extend the high-pressure surface plasmon spectroscopy established by G. Kleideiter [4] with other measurement techniques and to introduce supercritical pressure media to this field of optical characterisation. Therefore, emphasis has to be put on the results of the material systems investigated but also on the aspect of the measurement technique and instruments developed.

Surface plasmon spectroscopy is restricted by its need for a noble metal/dielectric interface in order to generate the evanescent electric field that probes the dielectric. Material systems that can for example be spin-coated onto the surface can easily be analysed. In most cases, though, e.g. adsorption processes or supramolecular architectures are of interest. Thiol-based self-assembly techniques work well with noble metals and are usually sufficient to generate supramolecular architectures, which can then be further functionalised for e.g. potential biosensing applications. However, in certain cases, such a thiol immobilisation strategy is not suitable and the use of other complex coupling chemistries is required. Silane coupling chemistries on silicon dioxide substrates are commonly used in many applications like e.g. in genomic research. In order to create a platform onto which silanes can couple a sol-gel chemistry approach (cf. chapter 4) is proposed for the generation of stable silicon oxide films on noble metals that can then be easily functionalised for sensing purposes.

The application of such silicon oxide films to N-isopropylarcrylamide hydrogels that are fixed on the films via silane chemsitry is reported in chapter 4.2. Gels are materials that combine liquid- and solid-like properties. In the swollen form a liquid, e.g. water, makes up most of the volume of the gel. When the volume phase transition of the gels is triggered by stimuli such as pH [5], temperature [6], magnetic fields [1], or electric fields [6] their state drastically changes from a solvent swollen to a collapsed state and vice versa.

The transition temperature in the presented thermoresponsive hydrogels results from a delicate balance of hydrophobic and hydrophilic groups within the polymer. Applying hydrostatic pressure has similar effects on the gel as for example ionisable co-monomers in that the hydrogen-bonding environment is disrupted and the characteristics of the transition changes. Moreover, the constraint of the gel being fixed to the surface in order to study it with surface plasmon spectroscopy additionally affects the transition temperature.

Dynamic light scattering and UV absorption spectroscopy represent the most widespread measurement techniques to characterise the stability of DNA duplexes at elevated pressures. However, the values determined in this way will not correlate to the ones of immobilised DNA on sensor chips since there the geometry and the surface potential plays an important part. Although the majority of biological processes occur at ambient conditions, temperature and pressure dependent studies represent the only way to thermodynamically characterise the molecular interactions contributing to the stability of DNA double helices. In order to perform these stability experiments the surface plasmon enhanced fluorescence technique [7] is extended to high pressures. Surface plasmon spectroscopy alone is not sensitive enough to detect low molecular weight adsorbates with low surface coverage. The indirect method of using fluorescent labelled target DNA, which is excited in the surface plasmon evanescent field, increases the sensitivity many-fold. In chapter 5 all layers of the supramolecular binding architecture are studied one after each other at elevated pressures and temperatures in order to verify their stability before the actual hybridisation reactions are investigated.

Supercritical fluids as solvent and reaction medium have attracted very much attention recently. They possess several advantages to conventional solvents especially with respect to the phisico-chemical properties, environmental inertness and in economic aspects. Due to the fact that in supercritical fluids no phase transition between liquid and gas exists the density and the transport properties can be varied continuously by changing temperature and pressure. As only a number of high and several low molecular weight substances are solvable in supercritical carbon dioxide most of the polymerisations are of heterogeneous nature. Along these lines, the thermodynamic behaviour of glassy polymer-gas systems is of general interest. The excellent solving characteristics of compressed gasses can lead to extensive swelling [8] and significant lowering of the glass transition temperatures [9]. The

technological application of e.g. polymerisation reactions therefore requires the knowledge of material parameters at elevated temperatures and pressures. Related to this problem chapter 6 presents studies of the swelling behaviour of polymethylmethacrylate films in carbon dioxide and carbon dioxide/methylmethacrylate films.

In chapter 7 a newly designed high-pressure cell is presented that combines high-pressure surface plasmon spectroscopy with electrochemical techniques. Electrochemical methods at elevated pressures provide information on volume changes and are particularly useful for studying reactions in which changes of charge and corresponding changes of electrostriction occur. In combination with surface plasmon spectroscopy all types of electrochemical reactions can be studied that result in optical changes of the dielectric medium. This includes e.g. supported bilayer lipid membranes [10] or electro-polymerisable monomers that form polymers on the metal surface [11]. The electrochemical cell is initially studied on the well characterised potassium hexacyanoferrate(III)-(II) system in order to verify the ability to perform accurate electrochemical measurements and the results are discussed. Thereafter, first results of experiments on the polymerisation of thiophene at elevated pressures are presented.

2. Introduction to the Basic Principles

2.1 Evanescent Wave Optics

The term 'evanescent wave optics' is derived from the latin verb 'evanescere', to vanish. It summarises a number of optical phenomena related to electromagnetic waves decaying perpendicular to the interface between two media of different optical properties. If, for example, a plane wave falls onto the interface between a high and a low refractive index medium from the high refractive index side the wave will be totally reflected at the interface from a certain angle of incidence - the so-called angle of total reflection θ_c on. The rigorous theoretical treatment of this problem shows that the electric field along the propagation direction at the interface is still oscillating as usual whereas its component perpendicular to the interface is decaying exponentially. The decay length d is of the order of the wavelength λ of the incident light and is described by the following equation:

$$d = \frac{\lambda}{2\pi n_2} \left(\frac{n_1^2}{n_2^2} \sin^2 \theta_i - 1 \right)^{\frac{1}{2}}, \quad \theta_i > \theta_c \tag{2.1}$$

Here n_1 and n_2 denote the refractive indices of the two media ($n_1 > n_2$) and θ_i represents the angle of incidence as measured from the normal to the surface. Such surface-bound, decaying waves are the basis for many experimental techniques that characterise surface properties. Changes in the optical properties of the medium within the decay length of the field cause a response in the properties of the same. This response is exploited by various types of spectroscopies as for example by total internal reflection fluorescence spectroscopy [12]. In the case of this work two extensions of the above stated simple phenomenon are used. The first one is concerned with plasmon surface polaritons, excitations at the interface between a noble metal and a dielectric. The second one deals with guided optical waves, which can be observed once a minimum thickness of the middle of a three layer system is reached. In this section some fundamental concepts needed for the following

discussions are outlined. A major part of this work is concerned with the excitation of surface waves and their interaction with the dielectric media they are associated with. Therefore, the mathematical description of electromagnetic waves and their interaction with an interface is introduced first. Then, the case of one of the two media forming the interface being a metal is presented. Two different ways of exciting surface plasmons, namely prism and grating coupling, are addressed. Thereafter, thick intermediate layers, which are able to guide optical modes, are discussed. Finally, the transfer-matrix method, which is able to describe the optical transmission and reflection behaviour of multilayer systems is introduced.

2.1.1 Plane Waves at Interfaces

Material properties and the geometry of the media influence the propagation of light through different materials. Mathematically, the description is based on the Maxwell equations, which form the basis of classical electrodynamics. Baring in mind that evanescent optical waves occur at interfaces between two dielectric media the most important processes at such an interface, i.e. refraction, reflection and transmission, are addressed.

2.1.1.1 Maxwell Equations and Plane Waves

With the simplification of isotropic, homogenous media electromagnetic radiation is described by Maxwell's equations without any source terms.

$$\nabla \cdot \mathbf{D} = 0 \qquad \nabla \times \mathbf{E} = -\frac{\partial \mathbf{B}}{\partial t}$$
$$\nabla \cdot \mathbf{B} = 0 \qquad \nabla \times \mathbf{H} = \frac{\partial \mathbf{D}}{\partial t} \tag{2.2}$$

Here, $\mathbf{E}$ is the electric field, $\mathbf{B}$ the magnetic induction, $\mathbf{H}$ the magnetic field and $\mathbf{D}$ the electrical displacement. The relations between $\mathbf{D}$ and $\mathbf{E}$ on one side and $\mathbf{B}$ and $\mathbf{H}$ on the other side are given by

$$\mathbf{D} = \underline{\varepsilon} \cdot \mathbf{E}$$
$$\mathbf{B} = \underline{\mu} \cdot \mathbf{H} \tag{2.3}$$

where the dielectric constant $\underline{\varepsilon}$ and the magnetic permeatibility $\underline{\mu}$ are generally complex tensors of second rank. However, for isotropic materials as considered here those tensors reduce to simple scalars $\epsilon\epsilon_0$ and $\mu\mu_0$, with ϵ_0 being the permittivity of vacuum and μ_0 being

the permeability of free space. Then the solution of Maxwell's equations as a function of time t at point $\mathbf{r}$ are plane waves, which are characterised by their electric field amplitude $\mathbf{E_0}$, their wavevector $\mathbf{k}$ and their angular frequency ω.

$$\mathbf{E}(\mathbf{r}, t) = \mathbf{E}_0 \cdot \exp\left[i\left(\mathbf{k} \cdot \mathbf{r} - \omega t\right)\right] \tag{2.4}$$

The interpretation of the above equation is that only the real part of the complex quantity has a physical meaning and the orientation of $\mathbf{E}_0$ is orthogonal to $\mathbf{k}$. For each pair of $(\mathbf{k},\omega)$ two mutually orthogonal electric field amplitudes exist, spanning the plane to give all possible polarisations. Besides the electric field, also the magnetic field (with the corresponding mathematical notation) contains the full information about the plane wave. Both representations may be transformed into each other by use of

$$\begin{aligned} \mathbf{H}(\mathbf{r}, t) &= \frac{1}{\mu\mu_0\omega} \cdot \mathbf{k} \times \mathbf{E}(\mathbf{r}, t) \\ \mathbf{E}(\mathbf{r}, t) &= \frac{1}{\varepsilon\varepsilon_0\omega} \cdot \mathbf{k} \times \mathbf{H}(\mathbf{r}, t). \end{aligned} \tag{2.5}$$

The dispersion equation relates the modulus $|\mathbf{k}|$ of the wavevector to a given angular frequency ω

$$\frac{\omega^2}{|\mathbf{k}|^2} = \frac{1}{\mu\mu_0\varepsilon\varepsilon_0} = \frac{c^2}{n^2}. \tag{2.6}$$

Here, the refractive index n is defined as the ratio of the speed of light c in vacuum and in matter. Making the assumption of a nonmagnetic material ($\mu = 1$) the dispersion equation can be further simplified to give

$$|\mathbf{k}| = \omega \cdot \sqrt{\varepsilon\varepsilon_0\mu_0} = k_0\sqrt{\varepsilon} = k_0 \cdot n. \tag{2.7}$$

2.1.1.2 Fresnel Equations

Figure 2.1 introduces and summarises the effects that can occur when a plane electromagnetic wave of fixed wavevector $\mathbf{k}_i$ and frequency ω falls onto a flat interface between two dielectric, homogenous media of refractive indices n_1 and n_2. At the interface the incident wave is subject to reflection and transmission, the wave being refracted. One characteristic of all these processes is the conservation of the wavevector $k_{||}$ parallel to the interface. However, the modulus and direction of the wavevector itself are changed. For the reflected beam this means that the angle of incidence equals the angle of reflection. For transmission, this conservation is mathematically expressed in Snell's law

$$n_1 \sin\theta_i = n_2 \sin\theta_t \tag{2.8}$$

where θ_i and θ_t are the angles of incidence and transmission, respectively, measured with respect to the surface normal. The conservation of $k_{\parallel}$ is also the reason why the electromagnetic field in a multilayer system can be decomposed into two components in each layer: An upward and a downward propagating plane wave that completely describe the whole system (see section 2.1.3).
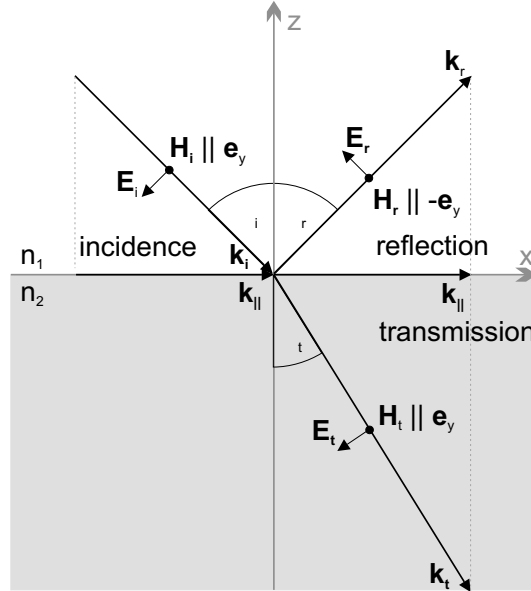
Figure 2.1: Schematic picture of a reflected and transmitted transverse magnetic polarized plane wave at an interface between two different dielectric media. The plane of incidence is spanned between the wavevector of the incident light beam and the surface normal. The in-plane components of the wavevectors are equal for all contributions.

The geometric configuration of a planar surface leads to a straightforward choice of orthogonal polarisation vectors which are needed to fully describe a plane wave with $(\mathbf{k}, \omega)$ and that don't change their state of polarisation upon reflection or transmission. On the one hand, this is the transverse electric (TE) polarisation or s-polarisation having its only electric field component perpendicular to the plane of incidence, that is spanned by the wavevector $\mathbf{k}_i$ and the normal to the surface. On the other hand, it is the transverse magnetic (TM) mode (or p-polarisation) that possesses its only non-vanishing magnetic field component perpendicular to the plane of incidence. In general, all polarisations may now be described by the linear superposition of the above mentioned two orthogonal polarisations.

In an experiment, usually the wavelength of light, the polarisation and the intensity of the incident beam are known. If such a beam impinges on an interface to another medium the analysis of the reflected or transmitted beam intensity gives insight into the properties of the material. Such a reflectivity spectrum, i.e. intensity of the reflected beam versus angle of incidence, can be calculated by using the Fresnel formulas. There are two different sets of formulas of reflection ratios r^{refl} and transmission ratios r^{trans} for the two different polarisations:

$$r^{refl}_{s-pol} = \frac{E_r}{E_i} = \frac{n_2 \cos\theta_i - n_1 \cos\theta_t}{n_2 \cos\theta_i + n_1 \cos\theta_t} \qquad r^{trans}_{s-pol} = \frac{E_r}{E_i} = \frac{2n_1 \cos\theta_i}{n_2 \cos\theta_i + n_1 \cos\theta_t}$$
$$r^{refl}_{p-pol} = \frac{E_r}{E_i} = \frac{n_2 \cos\theta_t - n_1 \cos\theta_i}{n_2 \cos\theta_t + n_1 \cos\theta_i} \qquad r^{trans}_{p-pol} = \frac{E_r}{E_i} = \frac{2n_1 \cos\theta_i}{n_2 \cos\theta_t + n_1 \cos\theta_i} \tag{2.9}$$

However, since only intensities are detected in an experiment the reflectivity R and the transmission T, that means the ratio of the respective intensities, can be written as

$$R = \frac{I_r}{I_i} = \frac{|\mathbf{E}_r|^2}{|\mathbf{E}_i|^2} = \left(r^{refl}\right)^2 \qquad T = \frac{I_t}{I_i} = \frac{|\mathbf{E}_t|^2}{|\mathbf{E}_i|^2} = \left(r^{trans}\right)^2 . \tag{2.10}$$

The deduction of the Fresnel equations follows the route of first setting up the appropriate plane wave equations for the incident, reflected and transmitted beams and then demanding that at $z = 0$ the fields (and therefore exponentials) have to be equal. This results in the equality of the angles of incidence and reflection and Snell's law. The requirement that the tangential components of $\mathbf{E}$ and $\mathbf{H}$ have to be continuous leads then to the Fresnel equations themselves.

2.1.1.3 Total Internal Reflection

The situation of light passing through medium 1 with a refractive index n_1, which is then reflected at medium 2 with a refractive index n_2 that is smaller than n_1 gives rise to a special feature: Beginning at an angle of incidence θ_1 of zero the transmission angle θ_2 can be determined according to Snell's law. The increase of θ_1 leads to an increase of θ_2 up to the point where θ_2 reaches a value of 90°. Then the so-called critical angle θ_c is reached. At that point the reflectivity reaches a value of $R = 1$, i.e. light is reflected, and any further increase of θ_1 has no influence on the reflectivity anymore (cf. figure 2.2). However, at such high angles the component of the field normal to the surface is not longer oscillatory but decays in an exponential way as given by equation (2.1). This is the regime of evanescent waves.
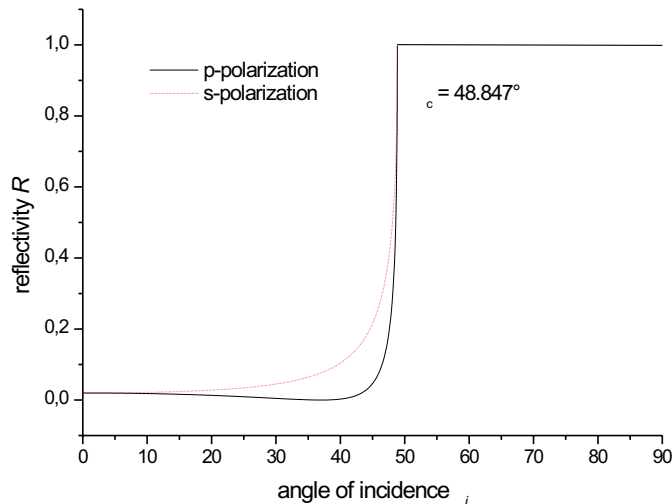
Figure 2.2: Calculated reflectivity as a function of the angle of incidence for the system sapphire ($n_1 = 1.769$) / water ($n_2 = 1.332$). Depicted are both, s- and p-polarisation for T = 25 °C and $\lambda = 632.8$ nm.

2.1.2 Plasmon Surface Polaritons

Before moving on to the theoretical description of plasmon surface polaritons, or surface plasmons for short, a brief, descriptive understanding of surface polaritons is given. The way in which surface plasmons are technically excited is then presented. There are mainly two methods, the prism and the grating coupling, available, which are considered here in detail. Finally, the focus is drawn on the question how the system responds if extra layers are added to the dielectric.

Wave-like electromagnetic modes that propagate along an interface between two media and whose amplitudes decrease exponentially normal to the surface are called surface polaritons, i.e. surface electromagnetic modes involving photons coupled to surface electric-dipole and/or magnetic-dipole excitations [13]. A plane wave of transverse electric-dipole excitation propagating along the x-axis in an optically isotropic medium is now considered as shown in figure 2.3a. Since the macroscopic polarisation **P** is transverse and $\nabla \cdot \mathbf{P}$ = 0 there are no volume polarisation charges and, thus, no electric field exists. Now a non-dispersive dielectric medium is introduced with a surface normal parallel to **P** (figure 2.3b). As a result of the discontinuity in **P** a periodic surface charge density is established

at the surface giving an electric field with components along x and z. Due to the fact that the surface charge density alternates in sign the magnitude of the fields decreases exponentially in the direction normal to the surface. Furthermore, the surface charge density is the only source of the electric field and thus its z-components at equidistant points from the interface are opposite in sign. However, since the normal components of the electric displacement $\mathbf{D}$ at the interface in both media have to be continuous it follows that the dielectric constants $\epsilon_1(\omega)$ and $\epsilon_2(\omega)$ have opposite sign (cf. eqn. (2.16)). This is the basic condition for the existence of surface electric-dipole excitations. When such an electrostatic field is coupled to 'surface photons' a so-called surface polariton is created, the total electric field of which consists of a superposition of the constituting electrostatic and electromagnetic fields. Since the coupling photon has to provide for the surface charge density the surface polaritons are TM modes.
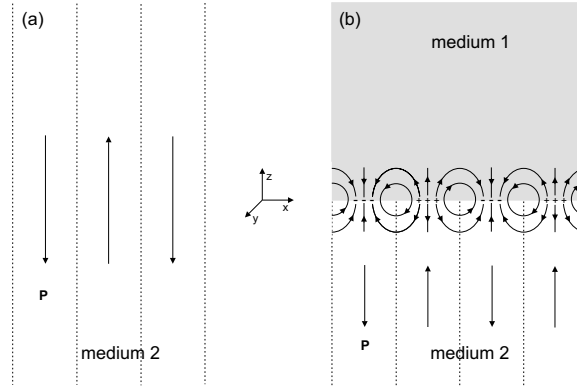
Figure 2.3: Schematic diagram of (a) a plane wave polarized along y and propagating in medium 2 along the x axis. (b) shows the surface charge density and the resulting electric field when a new medium 1 is introduced in the x-y plane.

2.1.2.1 Solving the Maxwell Equations

Again, the interface between two media of different frequency-dependent, but this time complex dielectric functions

$$\varepsilon_1 = \varepsilon_1' + i \cdot \varepsilon_1''$$
$$\varepsilon_2 = \varepsilon_2' + i \cdot \varepsilon_2''$$

$$(2.11)$$

is examined. The link between the complex dielectric constant ϵ and the complex refractive index $(n + i\kappa)$ is given by

$$(n + i\kappa)^2 = \varepsilon' + i\varepsilon'' = \varepsilon$$
$$\varepsilon' = n^2 - \kappa^2 \quad\quad\quad (2.12)$$
$$\varepsilon'' = 2n\kappa.$$

The real part n is called refractive index whereas the imaginary part κ is the absorption coefficient, i.e. responsible for the attenuation of an electromagnetic wave. The magnetic permeabilities μ_1 and μ_2 are considered to be equal to 1.

As explained above, there only exist surface polaritons for transverse magnetic polarised incident plane waves. Thus, the solution to the problem will have the general form of

$$\mathbf{A}_1 = \mathbf{A}_{01} \cdot \exp\left[i\left(k_{x1}x + k_{z1}z - \omega t\right)\right]$$
$$\mathbf{A}_2 = \mathbf{A}_{02} \cdot \exp\left[i\left(k_{x2}x + k_{z2}z - \omega t\right)\right] \quad\quad\quad (2.13)$$

for $\mathbf{A}$ either being the electric field $\mathbf{E}$ or the magnetic field $\mathbf{H}$. k_{x1} and k_{x2} are the wavevectors in x-directions and k_{z1}, k_{z2} the ones along the z-axis. The numbers 1 and 2 are references to the two media involved for $z > 0$ and $z < 0$, respectively. The continuity of the tangential components of $\mathbf{E}$ and $\mathbf{H}$ at the surface, i.e. $E_{x1} = E_{x2}$ and $H_{y1} = H_{y2}$, accounts for

$$k_{z1}H_{y1} = \frac{\omega}{c}\varepsilon_1 E_{x1}$$
$$k_{z2}H_{y2} = \frac{\omega}{c}\varepsilon_2 E_{x2}. \quad\quad\quad (2.14)$$

On the other hand, inserting equation (2.13) into Maxwell's equations (2.2) gives

$$k_{x1} = k_{x2} = k_x. \quad\quad\quad (2.15)$$

This leads to the only nontrivial solution if

$$\frac{k_{z1}}{k_{z2}} = -\frac{\varepsilon_1}{\varepsilon_2}. \quad\quad\quad (2.16)$$

This equation states that surface electromagnetic modes can only be excited at such interfaces where both media have dielectric constants of opposite signs, as has already been shown above. If one of the two media is a dielectric with a positive dielectric constant ϵ_d then the above relation can be fulfilled by a whole variety of possible elementary excitations if and only if their oscillation strength is large enough to result in a negative

dielectric constant ϵ. For excitations like phonons or excitons the coupling to a surface electromagnetic wave leads to phonon surface polariton or exciton surface polariton modes, respectively. Another type of excitation that can couple to surface electromagnetic waves is the collective plasma oscillation of a nearly free electron gas in a metal around the charged metal ions, called plasmon surface polaritons.

In dielectrics the electrons are bound tightly to the nuclei resulting in a small, positive and real dielectric constant. In metals, however, the electrons are quasi-free and may be moved easily by an external force. The classical Drude model [14], which considers the electrons to be free, already derives a highly negative, complex dielectric constant:

$$\varepsilon(\omega) = 1 - \frac{\omega_p^2}{\omega^2}. \tag{2.17}$$

The plasma frequency ω_p usually lies in the UV range for metals . The above equation is valid for frequencies ω from 0 up to a maximum frequency ω_{max}, which is given by

$$\omega_{\max} = \frac{\omega_p}{\sqrt{1 + \varepsilon_d}}. \tag{2.18}$$

For metals the dielectric function, ϵ_m, is in general complex with a negative real part and a small positive imaginary part.

Continuing the above deduction of the very distinct wavevector of a surface plasmon, the wavevectors in the direction of the z-axis can be calculated from the equations (2.2) and (2.14):

$$k_{zd} = \sqrt{\varepsilon_d \left(\frac{\omega}{c}\right)^2 - k_x^2} \quad \text{and} \quad k_{zm} = \sqrt{\varepsilon_m \left(\frac{\omega}{c}\right)^2 - k_x^2}. \tag{2.19}$$

Finally, with equation (2.16) this leads to the dispersion equation for surface plasmons at a metal/dielectric interface:

$$k_x = k_x' + i k_x'' = \frac{\omega}{c} \sqrt{\frac{\varepsilon_m \cdot \varepsilon_d}{\varepsilon_m + \varepsilon_d}}. \tag{2.20}$$

In conclusion, the complex nature of the wavevectors in x- and z-direction leads to an exponentially decaying wave in z and an attenuated wave along the x-axis. A finite propagation length L_x

$$L_x = \frac{1}{k_x''} \tag{2.21}$$

can be defined, which extremely influences the lateral resolution and is especially important in surface plasmon microscopy applications. For a gold/air interface with ϵ_m = -12 + i·1.3 and λ = 632.8 nm the propagation length is in the range of 10 μm.

2.1.2.2 Excitation of Surface Plasmons

Another aspect of the dispersion relation of surface plasmons (2.20) is summarised in the following equation:

$$k_{x,SP} = \frac{\omega}{c} \sqrt{\frac{\varepsilon_m \cdot \varepsilon_d}{\varepsilon_m + \varepsilon_d}} \quad \geq \quad \frac{\omega}{c} \sqrt{\varepsilon_d} = k_{x(\max),ph}. \qquad (2.22)$$

Clearly, one result of this equation is, as already stated above, that the z-component of the surface plasmon wavevector is purely imaginary (cf. eqn. (2.19)). Thus, the surface plasmon is a nonradiative evanescent wave with a maximum field amplitude at the interface. It decays exponentially into the dielectric and the metal. Another consequence is that a light beam incident from the dielectric with the maximum wavevector $k_{x(max),ph}$ at the interface (grazing incidence, i.e. the angle of incidence is 90° and, therefore, $\sin\theta_i = \sin 90° = 1$) cannot excite a surface plasmon with the wavevector $k_{x,SP}$ since its momentum is not sufficiently large. Figure 2.4 presents these details graphically. Although the light line of free photons (a) approaches asymptotically the dispersion curve of surface plasmons (SP I) there is no intersection of both curves and the x-component of the wavevector of incident light is always smaller than the one for surface plasmons. Among the developed methods to increase the momentum of the light in order to couple to surface plasmons there are for example nonlinear coupling [13] or coupling by means of a rough surface [15; 16]. By far the most predominant coupling techniques, however, are the prism coupling and the grating coupling, both of which will be discussed in the following.

2.1.2.2.1 Prism Coupling

As already pointed out, prism coupling represents one way of increasing the wavevector of the incident light and hereby the x-component of the wavevector, which only couples to the surface excitations. Figure 2.4(b) shows the corresponding dispersion relation if the refractive index of the prism n_p is larger then the one of the dielectric n_d. The momentum is increased, the curve more tilted and therefore at a given laser wavelength ω_l, coupling to surface plasmons (2, 3) can be obtained. However, since at point (4) the momentum of the light beam is too large it has to be tuned to the one of the surface plasmon by varying the angle of incidence ($k_{x,ph} = |k_{ph}| \cdot \sin\theta_i$).

There exist two different configurations with which to excite surface plasmons by use of a high refractive index prism. The one that was proposed first is the so-called Otto

configuration [17] (compare figure 2.5a). Here, the laser beam is reflected off the base of a prism (common geometries are half-spheres, half-cylinders or 90° prisms). A gap of low refractive index, less than a few radiation wavelengths thick (for visible $< 2 \ \mu$m) provides for a tunnel barrier across which the evanescent radiation couples from the totally internally reflecting base of the prism to the bound surface field of the surface plasmon. Experimentally, the resonant coupling is observed by monitoring the reflected light beam
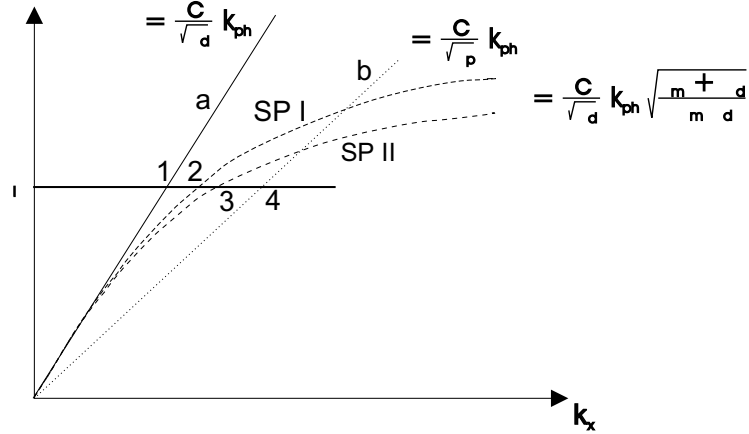

Figure 2.4: Dispersion relation of free photons in a dielectric (a) and in a coupling prism (b) with $n_p > n_d$, compared to the dispersion relation of surface plasmons at the interface between metal and dielectric before (SP I) and after (SP II) the adsorption of an additional dielectric layer. At a given laser wavelength ω_l the energy and momentum match of the photons impinging from a dielectric with the surface plasmon is not achieved (1) whereas for the photons incident through a prism, which is increasing the photons momentum, it is attained (2, 3).

as a function of the angle of incidence. However, there is a major technical drawback to this type of configuration as one has to fulfil the need of providing a gap of approximately 200 nm for efficient coupling. Even a few dust particles can act as spacers preventing a controlled assembly of the coupling system.

Fortunately, there is another method for coupling light to surface plasmons by means of a high refractive index prism - the Kretschmann configuration [18]. In this excitation scheme the light does not couple through a dielectric layer yet, alternatively, through a thin metal layer, which is directly evaporated onto the base of the prism. At the momentum matching condition a surface plasmon is then excited at the interface between

the metal and the dielectric, as depicted in fig. 2.5b. However, in contrast to the above derived mathematical description the surface plasmons are not restricted to two half-spaces anymore. Quantitatively, one has to take the finite thickness of the metal layer into account, which allows in particular that some of the surface plasmon light is coupled out through the metal and the prism. This new, additional radiative-loss channel, however, can be considered a minor disturbance to the surface plasmon electromagnetic wave [18; 19]. In any case, it is clear that there exists an optimum thickness of the metal: Taken
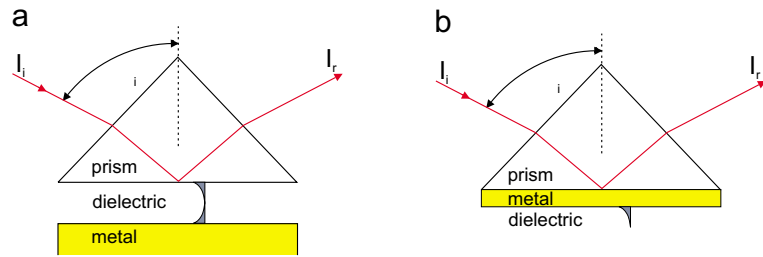

Figure 2.5: Coupling geometries for high refractive index prisms. (a) shows the Otto configuration whereas (b) the Kretschmann configuration. In both cases the surface plasmon propagates along the metal/dielectric interface. Coupling is only possible if the refractive index of the prism is higher than that of the dielectric.

that the metal film is too thin additional damping of the surface plasmon wave will occur due to the radiative loss channel back through the metal film and the prism. If the metal layer is too thick the tunnel barrier is too large and only little light will couple to surface plasmons at the metal/dielectric interface. For both, gold and silver, the optimum thickness for a laser wavelength of $\lambda = 632.8$ nm lies between 45 nm and 50 nm, which can be easily controlled by evaporation.

2.1.2.2.2 Grating Coupling

If there is no need to stick to a planar interface then another coupling geometry exists that is not restricted to the use of a prism. While there is on the one hand the possibility of utilizing a roughened surface to provide for the coupling conditions [16] the better alternative is to employ a sinusoidally modified interface of a specific and well-known wavelength Λ and groove depth. The grooves in the grating surface break the translational invariance of the interface and allow the wavevector $k_{x,out}$ of the outgoing wave to differ

from that of the incoming wave, $k_{x,in}$.

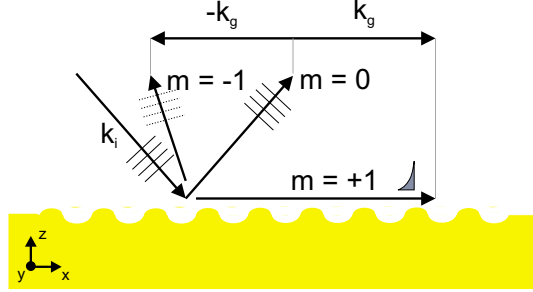$$k_{x,out} = k_{x,in} \pm m \cdot k_g \tag{2.23}$$

Figure 2.6: Sketch of the different diffraction orders induced by a surface grating.

The difference comes from the additional pseudo-impuls $m\hbar k_g$ with $k_g = 2\pi/\Lambda$ and m being the diffraction order, an integer. In case of sufficiently shallow gratings (depth $<< \Lambda$) the wavevector of the surface plasmon will be little changed from that on planar surfaces. Thus, the following equation can be applied:

$$k_{x,SP} = k_{x,in} \pm m \cdot k_g \tag{2.24}$$

The grating configuration allows direct excitation of surface plasmons from the dielectric half-space as depicted in figure 2.6. Sinusoidally corrugated interfaces as considered here can be described by a functional dependence $z(x)$.

$$z(x) = z(x + \Lambda) = \sum_{j=0}^{\infty} A_j \cdot \sin\left(\frac{360°}{\Lambda} \cdot j \cdot x + \varphi_j\right) \tag{2.25}$$

The periodicity of $z(x)$ allows for a Fourier representation with the amplitudes A_i and phases ϕ_j. The Floquet-Bloch theorem then states that the electric field outside the modulated area due to the reflected beam is given by

$$\mathbf{E}(x,t) = \sum_{m=-\infty}^{\infty} E_{TM}^m \cdot \mathbf{p}_{TM} \cdot \exp\left[i\left(k_m x - \omega t\right)\right] + E_{TE}^m \cdot \mathbf{p}_{TE} \cdot \exp\left[i\left(k_m x - \omega t\right)\right] \tag{2.26}$$

with two orthogonal unit polarisation vectors $\mathbf{p}_{TM}$ and $\mathbf{p}_{TE}$ and complex amplitudes of the electric field E_{TM}^m and E_{TE}^m. Additional diffraction orders are introduced by this

equation and the wavevector of the m'th diffracted order is written as

$$\mathbf{k}_m = \begin{pmatrix} k_x + m \cdot k_g \\ k_y \\ \pm\sqrt{(n \cdot k_0)^2 - (k_y)^2 - (k_x + m \cdot k)^2} \end{pmatrix}. \qquad (2.27)$$

The z-component of $\mathbf{k}_m$ is derived from the x- and y-components and the dispersion of light. Yet, it has again to be stressed that this equation is only valid for locations outside the grooves, only in the case of shallow gratings - the Rayleigh assumption - it may be used inside the grooves as well [20; 21]. Figure 2.6 shows the additional contributions to the electromagnetic field that arise from the presence of a surface relief grating. As already pointed out, in addition to the directly reflected beam with $m = 0$ new beams appear with an in-plane wavevector, which is modified by a multiple integer of the reciprocal grating vector. The -1st diffracted beam has a z-component (cf. eqn. (2.27)), which is the square root of a positive number. Therefore, it is a plane wave, as indicated in figure 2.6 by the parallel wave planes. In the case of the $+1^{st}$ diffracted beam, however, the z-component is purely imaginary and, as a consequence, the wave in z-direction is exponentially damped and bound to the surface. In x- and y-direction the oscillatory character of the wave is conserved. Generally, the solution of the electromagnetic problem of a plane wave falling onto a surface grating cannot be decomposed into two linearly independent orthogonal waves being excited either by TM or TE polarised light like on plane interfaces. Only in the so-called classical mount, i.e. $\mathbf{k}_i$ is incident perpendicular to the grooves, which means in x-direction, the solutions remain independent, as it is the case for the presented study. A more complete introduction to the electromagnetic theory of gratings is given in the book edited by Petit [20].

2.1.2.3   Addition of Dielectric Layers

So far the theoretical description of surface plasmons and their excitation methods have been presented. In this subsection an example of a surface plasmon resonance curve is shown and discussed. Some insight into the dependence of the surface plasmons on the type of metal is given and the differences between prism and grating excitation are briefly mentioned. Subsequently, the question is addressed what changes arise due to additional thin dielectric layers. The section closes with a discussion about consequences

of a transition from thin to thick dielectric layers and the mathematical description of the latter.

2.1.2.3.1 Bare Metal Reference

As high refractive prisms are used for the excitation of surface plasmons in the examples of figure 2.7, the momentum of the incident light beam in the plane of the interface exceeds the one needed for the excitation. Thus, it is possible to tune the system into resonance by simply changing the angle of incidence, as $k_x = k_0 \cdot \sin \theta_i$. At low angles, the reflected intensity increases as described by the Fresnel formulas. Then, from a certain angle, the angle of total reflection θ_c, onwards it reaches a plateau. Note, firstly, that the reflectivity before θ_c is rather high compared to the type of interface shown in fig. 2.2. This is due to the evaporated metal film that acts as a mirror reflecting most of the incident light. Secondly, the maximum reflected intensity never reaches unity (also as compared to
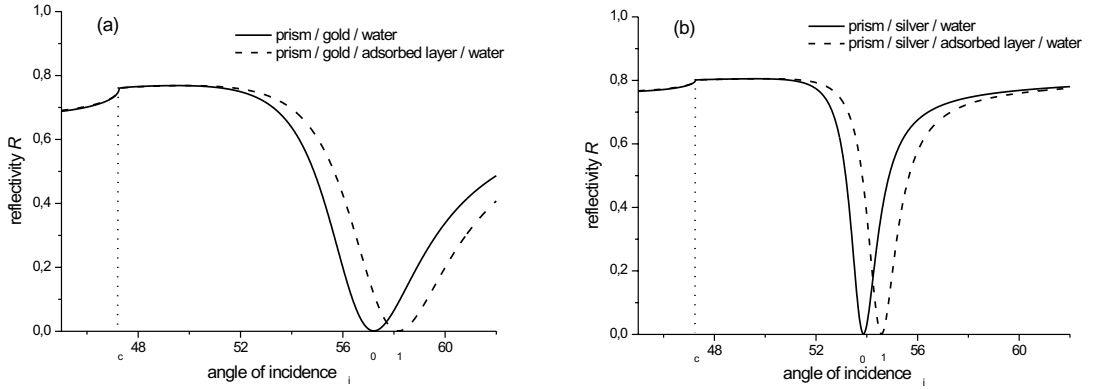
Figure 2.7: Reflectivity as a function of the angle of incidence for the system prism/gold/(adlayer/)water (a) and prism/silver/(adlayer/)water (b). θ_c is the angle of total reflection and θ_0, θ_1 are the angles of the surface plasmon resonance without and with additional dielectric layer, respectively. As basis for the calculations the following parameters are used: $n_{prism} = 1.845$, $\epsilon_{gold} = -12 + \text{i} \cdot 1.2$, $\epsilon_{silver} = -17 + \text{i} \cdot 0.7$, $n_{adlayer} = 1.5$, $d_{adlayer} = 5$ nm, $n_{water} = 1.332$.

fig. 2.2) since the photon energy is partly dissipated in the metal layer. Lastly, the position of the critical angle only depends on the substrate and superstrate, i.e. prism and water, and is not influenced by any of the intermediate layers. If the projection of $\mathbf{k}_i$

to the interface matches $k_{x,SP}$ resonance occurs and a surface plasmon is excited. This condition is given at the intersection 2 of figure 2.4. Once the system is in resonance surface electromagnetic waves are excited, which can be observed as a dip in the reflected intensity. The minimum is denoted by θ_0 (angle of incidence inside the prism θ_0') and is given by

$$\theta_0' = \text{asin}\left(\sqrt{\frac{\varepsilon_m \cdot \varepsilon_d}{(\varepsilon_m + \varepsilon_d) \cdot \varepsilon_p}}\right) \tag{2.28}$$

with ϵ_p being the dielectric constant of the prism. As mentioned above, for real metals there is resistive scattering and hence damping of the oscillations created by the incident electric field. (If not the surface plasmon resonance would be infinitely sharp and have an infinite propagation length.) The imaginary part of the dielectric constant of the metal causes the damping and the dispersion relation for surface plasmons can be rewritten as

$$k_x = k_x' + ik_x'' = \frac{\omega}{c}\sqrt{\frac{(\varepsilon_m' + i \cdot \varepsilon_m'') \cdot \varepsilon_d}{(\varepsilon_m' + i \cdot \varepsilon_m'') + \varepsilon_d}} \approx \frac{\omega}{c}\sqrt{\varepsilon_d}\left(1 - \frac{\varepsilon_d}{2\varepsilon_m'}\right) + i \cdot \frac{1}{2}\frac{\omega}{c}\frac{\varepsilon_m''(\varepsilon_d)^{3/2}}{(\varepsilon_m')^2}. \tag{2.29}$$

Thus, the shift of the surface plasmon is inversely proportional to ϵ_m' whereas the width, which is related to k_m'', depends on ϵ_m'' and is inversely proportional to $(\epsilon_m')^2$. While at first sight it might therefore be beneficial to have a small imaginary part of the metal dielectric constant the real part is of even higher significance. An example of this finding

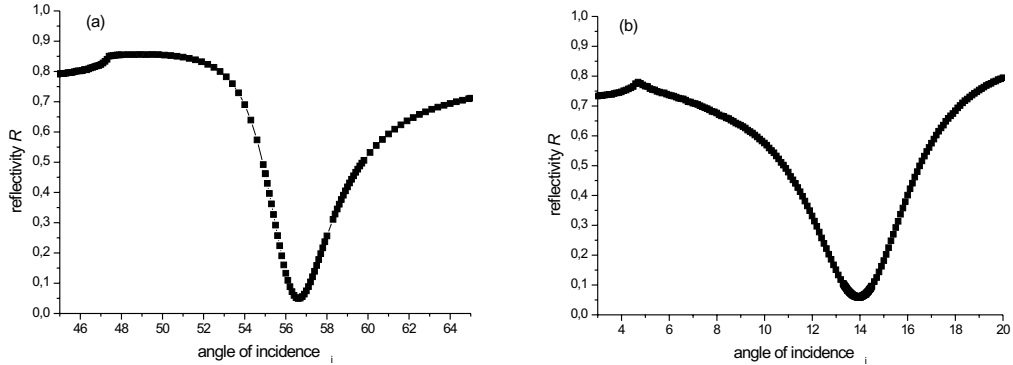**Figure 2.8:** Comparison of typical reflectivity vs. angle of incidence scans of a prism coupling (a) and a grating coupling (b) configuration. (As prism material LaSFN$_9$ glass is chosen.)

is given in figure 2.7 where surface plasmon resonance curves for gold and silver, ϵ_{gold} = -12 + i·1.2, ϵ_{silver} = -17 + i·0.7, are compared to each other. Clearly, silver with the

higher absolute value of ϵ'_m and the smaller imaginary part can be identified having a much sharper resonance.

At this point it has to be mentioned that there of course exists a difference between the shape of surface plasmons excited at a plane interface and at a surface grating. Figure 2.8 compares the different properties. For the prism coupling the actual position of the surface plasmon resonance depends strongly on the refractive index and, consequently, the type of glass of the prism (in this case LaSFN$_9$ glass, cf. fig. 2.4). The slope of the dispersion curve of light in a medium depends inversely on the square root of the dielectric constant of the material. A high refractive index of the prism, consequently, shifts the whole resonance curve to lower angles of incidence. The shape of the resonance curve, however, is calculated using Fresnel's formulas. On the contrary, the position and shape of grating coupled surface plasmons depends on the shape of the surface relief. Hence, it varies from grating to grating. The position of the edge of total reflection is a function of the wavelength of the grating and the coupling strength is dictated by the groove depth, as is the clarity of the edge of total reflection. This last parameter, though, is not as easily controlled as the evaporation thickness.

2.1.2.3.2 Thin Additional Films

The advantage of surface plasmon spectroscopy lies in its sensitivity to surface processes due to its evanescent field. This means, on the one hand, that a change of the superstrate, i.e. ϵ_d in equation (2.20), leads to either a drop or an increase of the wavevector of the surface plasmon resonance, depending on the sign of the change. For example, the resonance angle θ_0 for air and water can be found at low and high angles, respectively. On the other hand, the addition of a thin layer ($d << 2\pi/k_{zd}$) of a second dielectric to the already existing triggers a changed surface plasmon response and the corresponding shift of the dispersion curve is equivalent to a change of the overall refractive index integrated over the evanescent field. The net effect is a slight shift of the surface plasmon dispersion curve as can be seen in fig. 2.4 for an additional layer with higher refractive index than the one of the reference dielectric. At the same energy $\hbar\omega$ of incident light the dispersion curve of the surface plasmon intersects with the light line at higher wavevectors (point 4 in fig. 2.4). In terms of the reflectivity as a function of the angle of incidence the minimum is therefore shifted to higher angles.

When adding a layer to the existing system two parameters are of interest, the refractive index and the thickness of the film. In order to separate these two parameters at least two distinct features that are correlated to the addition are needed. Yet, the surface plasmon resonance only provides one. Consequently, only a set of parameters (n, d) can be derived from such reflectivity curves, provided both parameters are unknown. If one of them is known the other one can be obtained from fits to the curves. Several methods resolve the ambiguity of this problem: Firstly, resonance curves can be taken at different laser wavelengths [22]. This method, however, does not resolve the ambiguity of the unknown dispersion behaviour of the refractive index of the coating. Secondly, the contrast of the experiment can be varied [23], i.e. the surface plasmon curves are measured in at least two solvents with different refractive indices. The minimum shift does not depend on the absolute value of n but rather on the contrast, i.e. the refractive index difference between the layer and the surrounding medium. In both of the presented methods a set of at least two different curves of n vs. d is obtained, the intersection of which determines the correct refractive index and thickness of the additional layer. Finally, if the aim of the study and the chemicals allow the preparation of thick films, waveguide modes can be excited [24; 25]. If the film is sufficiently thick and an adequate number of modes is available, n and d can be evaluated separately and even the indicatrix may be obtained.

2.1.2.3.3   Waveguide Modes

Probably the most prominent example of guided optical waves are those which propagate in an optical fiber. By now most of the 'electronic traffic' across the oceans is conducted through bundles of optical fibers. Nevertheless, there exist other geometries, for example various types of channel waveguides or, as it is used in this work, planar slab waveguides. One requirement connects all different types of waveguides architectures: The totally internally reflected light is guided by a geometrically restricted volume of material with a refractive index larger than the ones surrounding it. With the system given in figure 2.9a this demand is phrased as

$$n_2 \geq n_1 \quad \text{and} \quad n_2 \geq n_3. \tag{2.30}$$

The condition for total internal reflection requires that the angle of the reflected light at the interfaces is larger than the respective critical angle, i.e.

$$\sin\theta \geq \frac{n_2}{n_{1,3}}. \tag{2.31}$$

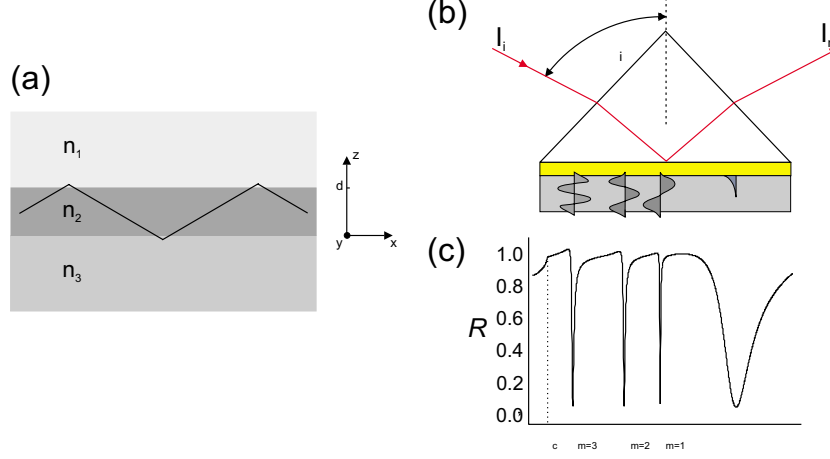In this picture of totally reflected light rays the well-known eigenvalue equation for

Figure 2.9: Geometry of a planar waveguide (refractive index n_2, thickness d) with superstrate (n_1) and substrate (n_3). Note the ray optic description of the guided light (a). In (b) the excitation scheme is shown where the light couples through a high refractive index prism and a metal film into the waveguide. Here, the optical field distribution along the y-axis is also given for the modes $m = 0$, 1, 2, 3. (c) Model $R(\theta)$ curve for a slab waveguide in the Kretschmann-configuration. The light is p-polarized.

waveguide modes can be derived [26]. Here, the eigenvalue equation will be determined starting from Maxwell's equations. As the light is only guided in layer 2 the following formulation of the electric and magnetic fields, represented by the amplitudes A, in the different layers will be made. The geometry again allows a separation into TM and TE modes.

$$
\begin{aligned}
A_{1y} &= A_1 \cdot \exp\left[-k_{1z}(z-d)\right] \quad z \geq d \\
A_{2y} &= A_2^+ \exp(ik_{2z}z) + A_2^- \exp(-ik_{2z}z) \quad 0 \leq z \leq d \\
A_{3y} &= A_3 \cdot \exp\left[k_{3z}z\right] \quad z \leq d
\end{aligned}
\tag{2.32}
$$

At this stage, the continuity relations for the tangential components of $\mathbf{E}$ and $\mathbf{H}$ have to be fulfilled, which gives for $z = 0$

$$A_3 = A_2^+ + A_2^-$$
$$\kappa_{3z} A_3 = \kappa_{2z}(A_2^+ - A_2^-) \tag{2.33}$$

and for $z = d$

$$A_2^+ \exp(ik_{2z}z) + A_2^- \exp(-ik_{2z}z) = A_1$$
$$-\kappa_{1z} A_1 = i\kappa_{2z} \left\{ A_2^+ \exp(ik_{2z}z) - A_2^- \exp(-ik_{2z}z) \right\}. \tag{2.34}$$

κ is defined for the layer j as

$$\kappa_{jz}^{TM} = \frac{k_{jz}}{\varepsilon_{jz}} \quad \text{and} \quad \kappa_{jz}^{TE} = k_{jz}. \tag{2.35}$$

The reflection coefficients r^{refl} are defined for both interfaces as the transversal field reflected at the interface divided by the one that is incident.

$$r_{23}^{refl} = \frac{A_2^+}{A_2^-} = \frac{i\kappa_{2z} + \kappa_{3z}}{i\kappa_{2z} - \kappa_{3z}}$$
$$r_{21}^{refl} = \frac{A_2^- \exp(-ik_{2z}d)}{A_2^+ \exp(ik_{2z}d)} = \frac{i\kappa_{2z} + \kappa_{1z}}{i\kappa_{2z} - \kappa_{1z}} \tag{2.36}$$

For both polarisation modes the boundary conditions result in the same condition for the existence of guided waves in a film:

$$r_{21}^{refl} \cdot r_{23}^{refl} \cdot \exp(i \cdot 2k_{2z}d) = 1 \tag{2.37}$$

The magnitude of the reflected beam cannot be larger than that of the incident wave and both reflection coefficients have therefore unit absolute value, which can be written as $r^{refl} = \exp(i\beta)$; $1 = \exp(m \cdot 2\pi i)$ with m being an integer. This reshaping of the formula leads to the eigenvalue equation for waveguide modes of the order m for non-adsorbing materials:

$$2k_{2z}d + \beta_{21} + \beta_{23} = m \cdot 2\pi. \tag{2.38}$$

The meaning is that guided modes can only exist if the phase changes due to reflectance at the interfaces β_{21} and β_{23} and the phase shift $2k_{2z}d$ accumulated during travelling add up resulting in an integer multiple of 2π. For a given set of materials and hence refractive index combinations the only variable in the mode equation that is not fixed is the thickness d. Thus, the number of eigenvalues, i.e. waveguide modes, only depends on the thickness of the waveguide. The characteristic wavevector of a guided mode is given

by k$_2$sinθ_i indicating that only for discrete angles of incidence light (of both polarisations) can be optically guided. A detailed analysis of Maxwell's equation also yields the optical field amplitudes for each eigenmode. The field distributions for different modes along the y-axis are depicted in figure 2.9b.

For coupling light into a waveguide the same techniques as for the excitation of surface plasmons, i.e. prism and grating coupling, can be used. In a configuration where one of the layers is a gold layer, through which the light is coupled the mode with $m= 0$ is the surface mode, the surface plasmon. Its intensity peak sits at the metal/waveguide interface and decays usually completely in the guiding film since the waveguide thickness is typically 1 μm or more as compared to the decay length of a surface plasmon of a few hundred nanometers. Thus, the angular position of it only depends on the refractive index n_{2z} and not the thickness of the layer. The other waveguide modes can be excited by p- and s-polarised light and depend in general on all three refractive indices n_{2x}, n_{2y}, n_{2z} as well as on the thickness. In a typical reflectivity vs. angle of incidence curve they are found in between the edge of total reflection and the surface plasmon resonance in falling mode order m (compare figure 2.9c).

2.1.3 Transfer Matrix Evaluation Method

The quantitative description of the transmission and reflection behaviour of every planar layer system discussed so far is based on the Fresnel equations. The mathematical methods use either a recursion formula procedure or a matrix formalism for solving the Fresnel equations in the case of multilayer systems. The latter approach, known as the transfer matrix method [27; 28], will be discussed here.

Due to the continuity of the tangential components of the wavevectors the complete electric and magnetic field in a multilayer system can be calculated by using only two partial waves propagating in positive (field amplitudes $(E_j^+,\ H_j^+)$) and negative (field amplitudes $(E_j^-,\ H_j^-)$) z-direction (cf. section 2.1.1.2), as shown in figure 2.10. The translational symmetry accounts again for the possibility to separate the solutions into TM and TE modes, both being represented by the amplitude A. A general solution of the introduced system in the z-direction yields the following expression:

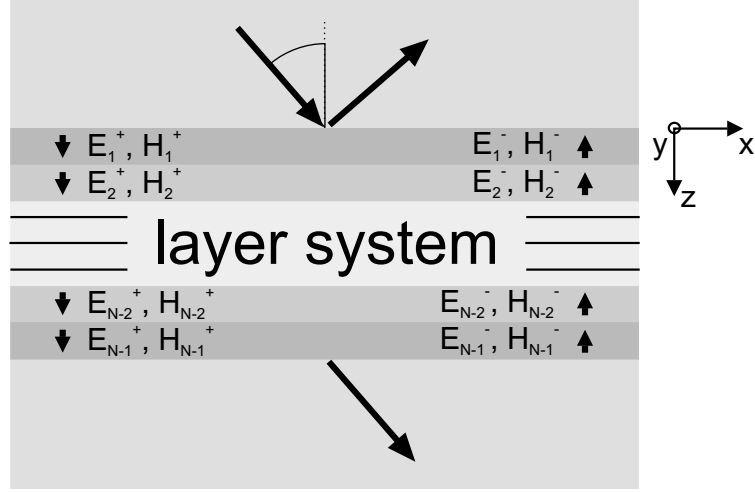$$A_j(z) = A_j^+ \exp(ik_{z,j}z) + A_j^- \exp(-ik_{z,j}z). \tag{2.39}$$

Figure 2.10: The multilayer system is composed of N+1 layers (the first and last one are omitted for clarity) each characterised by a dielectric constant ϵ_j and a thickness d_j. Within these layers the electric and magnetic field may be described completely by two plane waves propagating in positive (E_j^+, H_j^+ field amplitudes) and negative (E_j^-, H_j^--) z-direction.

As the lateral momentum $k_x = k_0 \sin \theta_i$ is constant throughout the system, the components of the wavevector $k_{z,j}$ are given by

$$k_{z,j} = \sqrt{\varepsilon_j \left(\frac{\omega}{c}\right)^2 - k_x^2}. \tag{2.40}$$

The propagation of a planar wave in one layer can now be described by the a matrix equation of the form

$$\begin{pmatrix} A_j^+(z_j) \\ A_j^-(z_j) \end{pmatrix} = \begin{pmatrix} p_j^{-1} & 0 \\ 0 & p_j \end{pmatrix} \begin{pmatrix} A_j^+(z_j + d_j) \\ A_j^-(z_j + d_j) \end{pmatrix} = P_j \begin{pmatrix} A_j^+(z_j + d_j) \\ A_j^-(z_j + d_j) \end{pmatrix}. \tag{2.41}$$

Here, the left side describes the field at the upper edge of the layer j and is connected through the propagation matrix P_j to the field at the lower edge of the same layer. The quantity p_j is given by

$$p_j = \exp(ik_{z,j}d_j). \tag{2.42}$$

Recruiting again the statements that the tangential components of the electric and magnetic field and the normal components of the dielectric displacement and the magnetic

induction are continuous at an interface it follows that

$$\begin{pmatrix} A_j^+(z_j + d_j) \\ A_j^-(z_j + d_j) \end{pmatrix} = \frac{1}{2} \begin{pmatrix} 1 + \kappa_j & 1 - \kappa_j \\ 1 - \kappa_j & 1 + \kappa_j \end{pmatrix} \begin{pmatrix} A_{j+1}^+(z_{j+1}) \\ A_{j+1}^-(z_{j+1}) \end{pmatrix} = Q_{j \to j+1} \begin{pmatrix} A_{j+1}^+(z_{j+1}) \\ A_{j+1}^-(z_{j+1}) \end{pmatrix}$$
(2.43)

where the matrix $Q_{j \to j+1}$ is called Fresnel matrix and connects the amplitudes of the electric and magnetic fields on both sides of the interface. It completely describes the reflection and transmission processes at the material transition. κ_j is given by

$$\kappa_j^{TM} = \frac{\varepsilon_{j+1} k_j}{\varepsilon_j k_{j+1}} \quad \text{and} \quad \kappa_j^{TE} = \frac{k_j}{k_{j+1}}.$$
(2.44)

The transfer matrix T then summarises the different contributions of all the interfaces and acts as an intermediary between both infinite half-spaces with $j = 0$ and $j = N+1$.

$$\begin{pmatrix} A_0^+(z_0) \\ A_0^-(z_0) \end{pmatrix} = Q_{0 \to 1} P_1 Q_{1 \to 2} P_2 \cdots Q_{N-1 \to N} P_N \begin{pmatrix} A_N^+(z_N) \\ A_N^-(z_N) \end{pmatrix} = T \begin{pmatrix} A_N^+(z_N) \\ A_N^-(z_N) \end{pmatrix}$$
(2.45)

At given refractive indices and thicknesses of the separate layers the transfer matrix is unambiguously determined if the angle of incidence and the wavelength of light are known. Therefore, a reflectivity vs. angle of incidence curve can easily be calculated even in the case of anisotropic media where the dielectric constants have to be replaced by tensors. Since in the presented geometry no reflected beam in the lower half-sphere exists, the reflection coefficient r^{refl} is normalized to 1 and equation (2.45) simplifies to

$$\begin{pmatrix} A_0^+(z_0) \\ A_0^-(z_0) \end{pmatrix} = T \begin{pmatrix} 1 \\ 0 \end{pmatrix}.$$
(2.46)

The reflectivity and transmission are calculated to be

$$R = \left| r^{refl} \right|^2 = \left(\frac{A_0^-(z_0)}{A_0^+(z_0)} \right)^2 = \left(\frac{T_{21}}{T_{11}} \right)^2 \quad \text{and} \quad T = \left| r^{trans} \right|^2 = \left(\frac{A_N^-(z_N)}{A_0^+(z_0)} \right)^2 = \left(\frac{1}{T_{11}} \right)^2.$$
(2.47)

2.2 Refractive Index as Thermodynamic Function

Surface plasmon spectroscopy studies yield the refractive indices of the surrounding medium and the refractive index and thickness of additional dielectric layers between the metal surface and the superstrate. If temperature and pressure vary the refractive index and

the specific volume of the substances under investigation respond. This section provides an introduction to the question how refractive index and specific volume are linked to the thermodynamic parameters temperature T and pressure p.

2.2.1 Lorenz-Lorentz Equation

The refractive index n is defined as the ratio of the speed of light c in vacuum and in matter. Consequently, the refractive index of any material is measured with respect to the refractive index of vacuum, which is defined to be equal to 1. Its value is therefore larger than 1. Thus, it strongly depends on the number and type of molecules that are present in the material. This means that every theory describing the refractive index has to contain the density ρ in its calculations and when the density is decreased it has to approach the value 1. The description of the refractive index, however, gets complicated when the density is that high that the molecules start to disturb each other. Moreover, temperature or pressure changes might not only have an effect on the density but also on other molecular properties, which in turn influence the speed of light in the material and hence its refractive index.

In consequence there are two different types of models: One type assumes that all microscopic parameters, as for example the polarisability, remain constant. The other also tries to include microscopic parameters in addition to the density into the calculations to better understand the material's response. All theories that relate the dependence of the refractive index upon temperature or pressure changes only to density changes conclude that the refractive index is a function of the density and the molecular properties of the material. This can be expressed as

$$f(n) = R \cdot \rho \tag{2.48}$$

where the constant R, the specific refraction or refractivity, is a function of the properties of the material. The connection between the refractivity and the refractive index varies for different theories:

The Lorenz-Lorentz equation is based on the Debye equation, which relates the microscopic quantities dipole moment μ and polarizability α characterizing the permanent and induced displacement of the electrons with respect to the nuclei to the macroscopic di-

electric constant.

$$\frac{\varepsilon^2 - 1}{\varepsilon^2 + 2} = \frac{N}{3\varepsilon_0} \left\{ \alpha + \frac{\mu^2}{3k_B T} \right\} \tag{2.49}$$

Here, N is the density of molecules and k_B the Boltzmann constant. Since the molecules themselves are heavy they cannot follow electromagnetic stimulation from a certain frequency on. Thus, the dipole moment part of the Debye equation can be neglected for frequencies above approximately 10^{11} Hz resulting in the Clausius-Mossotti equation. For optical frequencies (10^{14} - 10^{15} Hz) the dielectric constant can be replaced by the square of the refractive index ($\epsilon = n^2$) yielding the Lorenz-Lorentz equation found in 1880 [29; 30]:

$$\frac{n^2 - 1}{n^2 + 2} \cdot \upsilon(p, T) = \frac{N_A \alpha}{3\varepsilon_0} \tag{2.50}$$

In this equation the specific volume $\upsilon = \rho^{-1}$ has been introduced via the equation $N = N_A \rho M^{-1}$, where N_A is Avogadro's number and M is the molar mass. Typically, the Lorenz-Lorentz equation is presented in the following way

$$R_{LL} = \frac{n^2 - 1}{n^2 + 2} \cdot \upsilon(p, T) = \text{const.} \tag{2.51}$$

stressing the fact that the microscopic parameters are assumed to be constant and that the connection between the refractive index and the specific volume is of importance. Other semi-empirical equations that fall into the first category of theories are for example the Beer-Landolt or Gladstone-Dale equation [31]

$$R_{GD} = (n - 1) \cdot \upsilon(p, T) = \text{const.} \tag{2.52}$$

or the Eykman equation [32]

$$R_E = \frac{n^2 - 1}{n^2 + 0.4} \cdot \upsilon(p, T) = \text{const.} \tag{2.53}$$

The great number of publications dealing with the relation between refractive index and specific volume reveals the importance of the problem to which, even up till now, only semi-empirical formulas exist. For each of the given formulas experimental data are available that either confirm or contradict the theory [33; 34]. In reality none of the given equations completely mirrors the truth but only to some extend. Some publications - especially in the case of supercritical carbon dioxide - therefore go further and replace the constant refractivity by a virial expansion [35; 36].

$$\frac{n^2 - 1}{n^2 + 2} \cdot \frac{1}{\rho(p, T)} = A_R + B_R \cdot \rho(p, T) + C_R \cdot \rho^2(p, T) \tag{2.54}$$

Here, A_R, B_R and C_R are the virial coefficients. Another equation that does not treat the refractivity as a constant is the one introduced by H. Eisenberg [37] to give a very accurate description of water in the temperature range from 0 °C to 60 °C and pressures up to 110 MPa.

$$f(n) = \frac{n^2 - 1}{n^2 + 2} = A\rho^B \exp(-CT) \tag{2.55}$$

A, B and C are parameters that are fit to the experimental data and reproduce it with an extraordinary low error of $\Delta n = 10^{-7}$. Other approaches take a theoretical instead of an empirical or engineers pathway and to relate macroscopic with microscopic quantities. Such methods get an extension to the Lorenz-Lorentz equation by taking density fluctuations calculated from dipole-dipole interactions in liquids into account [38].

In this study the refractivity is considered constant except for the measurements in supercritical carbon dioxide where equation (2.54) is used. The error accompanied with the assumption of a constant refractivity is of the order of $\Delta n = 10^{-4}$ for the temperature and pressure range employed. On the other hand, the high-pressure spectrometer that is used has a precision of approximately $\Delta n = 10^{-3}$. Therefore, the description of the measured data with one of the given equations is sufficient.

In an ideal mixture the volumes of the individual components add up to the total volume and any volume changes upon mixing are neglected. The refractive index n_m of such a mixture consisting of i components can be calculated, based on the Lorenz-Lorentz equation, by summation of the refractivities $R_{LL,i}$ of the components times their volume fraction υ_i:

$$\frac{n_m^2 - 1}{n_m^2 + 2} = \sum_{n=1}^{i} R_{LL,i} \cdot \upsilon_i \tag{2.56}$$

In case of non-ideal mixtures the volume fractions of the components have to be replaced by

$$\upsilon_i = \frac{V_i}{V_m} = \frac{p_i}{\rho_i} \cdot \frac{\rho_m}{p_m}, \tag{2.57}$$

where p_i and p_m are the weight fractions of component i of the mixture and V_i and V_m are the respective volumes. In a similar fashion, the other expressions like the Gladstone-Dale equation can be extended to cover mixtures as well.

2.2.2 Tait Equation

All the semi-empirical equations for the refractive index assume that the temperature and pressure dependences are covered completely by the variations of the density with respect to these two quantities. Therefore, the density has to be established as a function of temperature and pressure. For closed systems the mass is a constant, thus, the density and density changes can be described by volume and volume changes. Volume and specific volume, however, are from the mathematical point of view equivalent. In general, the specific volume changes with pressure and temperature according to

$$v\left(p, T\right) = v_0 \left[1 + a\left(T\right) + k\left(p\right)\right], \tag{2.58}$$

where v_0 is the specific volume at standard conditions ($p_0 = 1.013 \times 10^5$ Pa, $T_0 = 25$ °C), $a(T)$ is the isobaric thermal expansion and $k(p)$ is the isothermal compression. The latter two parameters rely on the particular equation of state (EOS) and can, in the simplest case of the ideal gas equation, be written as

$$a_T\left(T\right) = \frac{1}{v_0} \cdot \left.\frac{\partial v}{\partial T}\right|_{p=p_0} \cdot \left(T - T_0\right) = \alpha_T \cdot \left(T - T_0\right) \tag{2.59}$$

and

$$k_p\left(T\right) = -\frac{1}{v_0} \cdot \left.\frac{\partial v}{\partial p}\right|_{T=T_0} \cdot \left(p - p_0\right) = \kappa_p \cdot \left(p - p_0\right) \tag{2.60}$$

with α_T being the thermal expansion coefficient and κ_p the bulk compressibility. The equation of state serves to accurately describe the experimental PVT data, i.e. specific volume as a function of temperature and pressure. Yet, it also allows the calculation of physical properties such as the thermal expansion coefficient or the compressibility at various (T, p) sets. As in the case of the refractive index, there are two different types of EOS: Empirical descriptions and those based on theoretical considerations. An example of the former type is the Tait equation [39; 40]. Although it was originally derived to describe the isothermal compressibility of fresh and seawater between 0 °C and 15 °C it has been successfully applied to polymers in the glassy, semi-crystalline and melt state as well as to liquids [41]. It has also found widespread application because of its simplicity and often rather accurate description of PVT data and has undergone modifications that allow e.g. for the dependence of the volume on the cooling rate in amorphous polymers [42]. In the case of the ideal gas equation the thermal expansion coefficient and the bulk

compressibility are constant and not coupled. Tait found that the compressibility itself is a function of pressure and temperature

$$\kappa_p(T, p) = \frac{dk_p}{dp} = \frac{C}{B(T) + p}. \tag{2.61}$$

$C = 0.0894$ is a constant [43; 44] and $B(T)$ is the temperature-dependent Tait parameter. For the case $p = 0$ the bulk compressibility κ_0 is

$$\kappa_0(T, 0) = \frac{C}{B(T)}. \tag{2.62}$$

The integration of (2.61) then gives together with (2.62) the compression $k_p(T, p)$

$$k_p(T, p) = C \ln\left(\frac{B(T) + p}{B(T) + p_0}\right) = \kappa_0 B(T) \ln\left(\frac{B(T) + p}{B(T) + p_0}\right) \tag{2.63}$$

which can be reformed by the introduction of a power series according to Yamashita [45] to give

$$k_p(T, p) = 1 - \kappa_0 B(T) \ln\left(1 + \frac{p}{B(T)}\right). \tag{2.64}$$

Inserting this equation into (2.58) yields

$$v(T, p) = v_0(T, 0)\left\{1 - \kappa_0 B(T) \ln\left(1 + \frac{p}{B(T)}\right)\right\}. \tag{2.65}$$

For the Tait parameter usually an exponential behaviour with the parameters B_0 and B_1 is assumed

$$B(T) = B_0 \exp(-B_1 T) \tag{2.66}$$

whereas for the zero-pressure isobar $v_0(T, 0)$ either a polynomial or an exponential expression are taken

$$v_0(T, 0) = v_0 \exp(v_1 T). \tag{2.67}$$

or

$$v_0(T, 0) = v_0 + v_1 \cdot T + v_2 \cdot T^2 + ... \tag{2.68}$$

Here, v_0, $v1$ and v_2 are constants.

For the borderline case of very small pressures $p << B(T)$ the expansion into a series of $\ln(1+x) = x - x^2/2 + x^3/3 - ...$ leads to $k_p = \kappa_0 \cdot p$, the expression for the ideal gas equation. At very small temperatures the equations (2.67) and (2.68) $(\exp(x) = 1 + x + x^2/2! + ...)$ give $v_0(T, 0) = v_0(1 + \alpha_T \cdot T)$ The thermal expansion coefficient and the compressibility are now calculated to be

$$\alpha_T(T, p) = \frac{1}{v_0} \cdot \left.\frac{\partial v}{\partial T}\right|_p = \alpha(0, T) - pB_1\kappa(T, p) \tag{2.69}$$

and

$$\kappa_p\left(T,p\right) = -\frac{1}{v_0} \cdot \left.\frac{\partial v}{\partial p}\right|_T = \left[\frac{C}{B(T) + p}\right]\left[1 - C\ln\left(1 + \frac{p}{B(T)}\right)\right]. \qquad (2.70)$$

Within the Tait EOS these two variables are not constant as compared to the ideal gas equation but still remain a function of temperature and pressure. Despite attempts to theoretically interpret the parameters C and $B(T)$ [46] the shortcoming of the Tait equation is that the material dependent parameters lack a rigorous molecular interpretation. On this ground other EOS theories have been developed, one of the most successful equation being the Simha-Somcynsky EOS theory [47; 48]. This theory is based on a quasi-lattice where molecules of different chemical repeat units and sections occupy only a fraction of the lattice sites. It has been successfully applied to homopolymers as well as polymer solutions and blends in the melt state [41; 49].

2.3 Fluorescence

Surface plasmon resonance spectroscopy allows the characterization of adsorption processes at a metal surface by means of a change of optical properties of the evanescent field. The evaluation of the data is based on a shift of the resonance minimum that depends on the amount of material that is adsorbed onto the surface. As a consequence, the detection of small molecules or a very loosely packed layer may fall under the resolution limit of this type of spectroscopy. One way to overcome this problem is to take advantage of fluorescence methods. These techniques are widely used in chemical as well as biochemical research featuring extraordinary sensitivity and low response times. The combination of these two methods then leads to an increase of surface sensitivity [7].

Fluorescence is defined as a photon-active transition from an electronically excited singlet state to the (singlet) ground state [50]. Since these transitions are quantummechanically allowed the decay rates are of the order of 10^8 s^{-1}. The Jablonski diagram (figure 2.11) gives a simplified view of what may happen when molecules get excited and relax. A fluorophore, often characterised by strongly delocalised electrons in conjugated double bonds or aromatic systems, has a number of electronic states, two of which are depicted here (singlet S_0 and S_1). Each of these electronic levels is further distinguished by various vibrational states, which are populated according to the Boltzmann distribution. Hence, at room temperature most of the molecules will reside in the lowest vibrational level of S_0.

Upon absorption of light the molecule is excited to one of the vibrational levels of a higher singlet state, e.g. S_1, in a time scale of a femtosecond, giving some information about the excited states of the molecule. Once in the excited state the fluorophore relaxes by internal
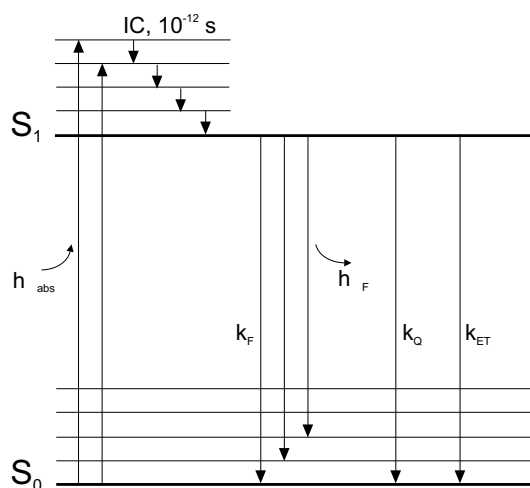

Figure 2.11: Simplified Jablonski diagram. The energies of some electronic (S_0 and S_1) and vibrational states of a molecule are sketched. Absorption of light results in an excited molecule that relaxes due to internal conversion (IC) and further through fluorescence (k_F), quenching (k_Q) or resonant energy transfer (k_{ET}) channels.

conversion (IC) typically within picoseconds to the lowest vibrational state of S_1. Since the fluorescence relaxation is of the order of 10 nanoseconds the photonic relaxation starts from the lowest vibrational level of S_1 and ends in one of the vibronic states of S_0. The relaxation, therefore, reveals some information about the vibronic states of the ground state S_0. Due to the internal conversion in the excited electronic state and the relaxation into one of the higher vibrational levels of the ground state the emitted light has a lower energy (it is red-shifted) than the exciting light, an effect which is referred to as Stokes' shift. This loss of energy enables an easy separation between the exciting and emitted light by means of a filter and a low background level can be obtained in experiments. Given an excited state S_1 the fluorophore has optionally, in addition to the emission of fluorescence light with a rate k_F, also other, radiationless, energy dissipation channels leading to a depopulation of S_1. Electronic transitions to triplet states by intersystem crossing (k_{ISC}) as well as quenching processes (k_Q) and resonant energy transfer (k_{ET})

result in a decrease of the quantum efficiency Φ, i.e. the ratio of emitted to absorbed photons:

$$\Phi = \frac{k_F}{k_F + (k_{IC} + k_{ISC} + k_Q + k_{ET})} \tag{2.71}$$

Quenching effects that decrease the fluorescence intensity by e.g. complex formation, energy transfer, excited state reactions or collision quenching can be divided into dynamic and static processes. Collision quenching falls into the first category and describes the effect that the quenching species hits the fluorophore and thereby returns it into its ground state. The collision probability increases with temperature. With static quenching, the complex formed between quencher and fluorophore is itself non-fluorescent. Formed complexes are expected to be less stable and therefore static quenching is reduced upon increasing the temperature. Another effect that influences the fluorescence behaviour of a molecule is the environment the fluorophore is facing. The polarity of the solvent giving rise to interactions between the dipole moments or the pH resulting in chemical reactions such as hydrogen bonding or acid-base chemistry can alter for example the fluorescence intensity and emission wavelength.
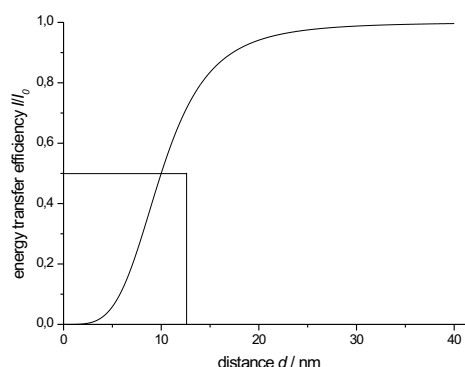

Figure 2.12: Energy transfer efficiency dependent on the donor-acceptor distance d. The Förster radius is the distance at which half of the absorbed energy is transferred to the acceptor.

Due to the requirement of surface plasmon excitation to have a metal surface involved another type of quenching has to be considered: In the vicinity of metal substrates or, in general, any molecules resonant energy transfer between donor and acceptor, treated as classical dipoles, can occur [51; 50]. Depending on the geometry of the two involved species

(i.e. molecule-molecule, molecule-line of molecules or molecule-surface of molecules) different energy transfer efficiencies $\Phi_{ET}(d)$ can be calculated. For the case of a molecule close to a surface it is given by [52].

$$\Phi_{ET}(d) = \frac{I(d)}{I_\infty} = \left[1 + \left(\frac{d_F}{d}\right)^4\right]^{-1}. \tag{2.72}$$

Here, $I(d)$ denotes the intensity which is emitted at a certain distance d of the molecule from the surface. I_∞ is the fluorescence intensity with out a surface nearby and d_F is called the Förster radius. It is the distance from the surface at which half of the maximum intensity I_∞ is radiated and has a value of approximately 10 nm for the discussed metal surface (see fig. 2.12). In addition to this dissipation channel the fluorescent light excited in the evanescent field of a surface plasmon can couple back to a surface wave and is then re-emitted at a slightly lower angle than the exciting light as the wavelength of the fluorescent light is red-shifted [53]. In conclusion, there are several dissipation channels for a fluorophore excited by a surface plasmon. Depending on the distance from the metal surface it may be quenched by resonant energy transfer and energy dissipation in the metal, it might excite another surface plasmon wave or, if it is sufficiently far from the surface, emit a free photon.

2.4   Langmuir Adsorption

In the case when a surface is thought of as a sensor that serves as a platform to immobilise analyte molecules through specific adsorption in a gaseous or liquid environment a fundamental understanding of the interaction between molecules and surfaces is of vital importance. The characterisation of adsorption processes may lead to an improvement of known detection schemes and an optimisation of the reaction protocols. In general, the free and immobilised molecules are in a dynamic equilibrium. The surface coverage Θ of the surface depends on the concentration of analyte molecules and the variation of Θ with concentration at constant temperature is called adsorption isotherm. The understanding of surface processes is based on the assumption that there is only a limited number of binding sites available that can be occupied by binding species up to complete coverage of all binding sites at the surface. The simplest physical plausible theory is the Langmuir isotherm [54] that is based on three assumptions:

- All sites are equivalent and the surface is uniform, i.e. perfectly flat.

- The binding does not depend on the occupation of neighbouring sites.

- Adsorption cannot proceed beyond monolayer coverage.

If these conditions are met the dynamic equilibrium is given by

$$A_{gas,liquid} + M_{surface} \rightleftharpoons AM_{surface} \tag{2.73}$$
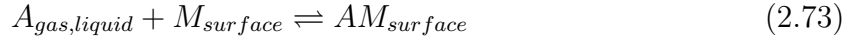
with an adsorption rate constant k_{on} and a rate constant k_{off} describing the desorption process. The change of surface coverage with time due to adsorption depends on k_{on}, the concentration c_0 of molecules A in solution, and the number of vacant sites (1 - Θ)

$$\frac{\partial \Theta}{\partial t} = c_0 k_{on}(1 - \Theta) \tag{2.74}$$

whereas the change of Θ due to desorption solely depends on k_{off} and the surface coverage

$$\frac{\partial \Theta}{\partial t} = -k_{off}\Theta. \tag{2.75}$$

According to these equations the surface will be further loaded until all binding sites are occupied, with a faster rate as c_0 is increased. The addition and successive integration of both equations with the initial condition $\Theta = 0$ and $t = 0$ yields

$$\Theta(t) = \frac{c_0 k_{on}}{c_0 k_{on} + k_{off}} \{1 - \exp\left[-(c_0 k_{on} + k_{off})t\right]\}. \tag{2.76}$$

Experimentally, the desorption process can be followed separately. The analyte solution is exchanged with a pure buffer solution with $c_0 = 0$. The first term of eqn. (2.76) then equals to zero and only the desorption term remains. The desorbed molecules are also prevented from re-adsorption by continuous rinsing with pure buffer.

At the point of equilibrium there is no net change of the surface coverage. Therefore, the sum of eqns. (2.74) and (2.75) equals zero and the solving for Θ gives the Langmuir isotherm

$$\Theta = \frac{c_0 K}{1 + c_0 K}. \tag{2.77}$$

According to this equation the equilibrium constant $K = k_{on}/k_{off}$ of the reaction can be established from the experimentally determinable analyte concentration and the surface coverage. In the case of fluorescence measurements Θ is given by the detected normalised fluorescence intensity over the maximum signal at complete surface coverage.

Usually this idealised picture of a Langmuir adsorption behaviour is not met by experimental results. The assumptions of monolayer formation or the independence of the binding process from neighbouring molecules are not fulfilled. As a consequence other models like the BET or Temkin isotherms, which take such deviations from the Langmuir picture into consideration, have been developed.

2.5 Cyclic Voltammetry

Cyclic voltammetry (CV) provides a completely different sight on the processes that occur at a metal surface, which then operates as working electrode. CV has the advantage that the product of the electron transfer reaction that took place in the forward scan can be probed again in the reverse scan. In addition, it is a powerful tool for the determination of formal redox potentials, detection of chemical reactions that precede or follow the electrochemical reaction and evaluation of electron transfer kinetics. Especially useful and complementary to surface plasmon measurements is its ability to determine the surface coverage of a certain species.
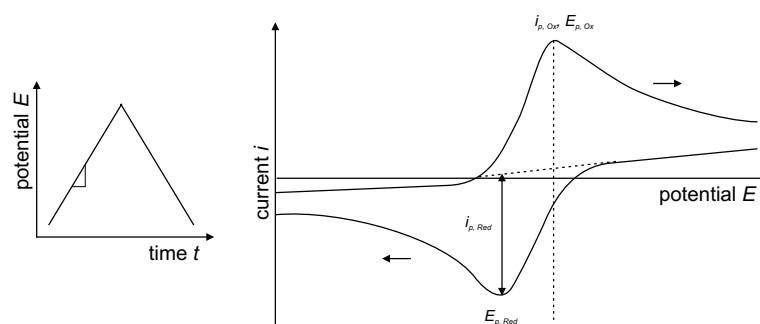

Figure 2.13: Scheme of the potential wave form and the cyclic voltammogram. The important quantities have been labelled.

A typical cyclic voltammetry experiment is conducted in a three-electrode configuration consisting of a working electrode at which the reaction takes place, a counter electrode that closes the electrical circuit, and a reference electrode that is current-free electrode and serves to measure the voltage between itself and the working electrode. Counter electrodes should be therefore so-called non-polarisable electrodes, e.g. Pt-electrodes, which allow for charge transfer to take place in a wide potential range. Contrary to the

counter electrodes non-polarisable electrodes of the second kind keep a constant potential irrespective of the current. Thus, reference electrodes should be non-polarisable electrodes of the 2nd kind, one of which is the Ag/AgCl, sat. KCl electrode.

Fundamental to all electrochemical methods is the study of the charge transfer at the interface between an electrode and electrolyte. The simplest electrochemical redox reaction is described by the following equation:

$$Ox + ne^- \rightleftharpoons Red. \tag{2.78}$$
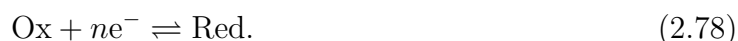
Here, Ox and Red are the oxidised and reduced form of the molecule under investigation and n is the number of electrons e^- transferred. The cyclic voltammogram of such a reaction would look similar to the one shown in figure 2.13. After the establishment of the initial set potential, which has to be substantially more negative than the reduction potential of the redox pair, a non-faradaic charging current flows, which charges the electric double layer at the electrode/electrolyte interface. As the voltage is scanned at constant rate in the positive direction, the reduced compound is oxidised at the electrode surface and an anodic, faradaic current flows. At a particular set value the scan direction is reversed and the material that was oxidised in the outward excursion is then reduced. Once the voltage is returned to the initial value the experiment can be terminated. As can be seen in the basic shape of the current response for a cyclic voltammetry experiment (c.f. fig. 2.13 right), at the start of the experiment the solution only contains the reduced form of the redox couple and there is no net conversion of Red into Ox. However, as the potential approaches the redox potential the anodic current increases exponentially. The anodic peak of the curve corresponds to the point when all reduced molecules at the surface are immediately converted into their oxidised form and diffusion controls the current, which decreases as concentration gradients for Red and Ox are established. Upon reversal of the scan the same processes occur in the cathodic part of the voltammogram. The most important quantities that describe a cyclic voltammogram are the peak currents $I_{p,Ox}$ and $I_{p,Red}$ as well as the respective peak potentials $E_{p,Ox}$ and $E_{p,Red}$. From the peak potentials the half-way potential

$$E_{1/2} = \frac{E_{p,Ox} + E_{p,Red}}{2} \tag{2.79}$$

can be determined, which is very close to the thermodynamic redox potential E^0. As

already mentioned, two different types of current, non-faradaic and faradaic, can be distinguished in general. Non-faradaic currents are solely electrostatic nature and are not connected to any electrochemical reaction but rather result from the reorientation of the electrolyte at the electrode interface. The charging of the so-called Helmholtz double layer is such an example. Faradaic currents summarise processes that comprise an electrochemical reaction. According to Faraday's law the electric current flowing through the electrode due to the application of a potential is proportional to the amount of electrochemical reactions at the electrode. In the example mentioned above the Faradaic current is controlled by the heterogeneous electron transfer across the interface and the material transport to and from the surface.

In general material transport is controlled by the three mechanisms diffusion, migration, and convection. The migration (movement of particles along a potential gradient) however can be minimised by an appropriate cell construction and the addition of sufficient electrolyte salt. The influence of convection can also be substantially reduced when restricting to short experiments at constant temperature and negligible mechanic agitation. The only contribution to mass transport is then diffusion that is described by Fick's laws. The heterogeneous electron transfer is given by the Butler-Volmer equation

$$i = nFAk_0 c_{Ox} \cdot \exp[-\frac{\alpha nF}{RT}(E - E^0)] - c_{Red} \cdot \exp[-\frac{(1-\alpha)nF}{RT}(E - E^0)], \qquad (2.80)$$

where k_0 is the standard rate constant, α is an average factor, R is the gas constant, F is the Faraday constant, and E^0 is the standard potential. Depending on the relative magnitude of the rate constants of the material transport k_{MT} and the heterogeneous charge transfer k_{CT} one distinguishes:

$\mathbf{k_{CT}} >> \mathbf{k_{MT}}$: Processes where the charge transfer is much faster than the material transport are called reversible. They are diffusion controlled and if the system is in equilibrium ($i = 0$) the Butler-Volmer equation simplifies to the Nernst equation

$$E = E^0 + \frac{RT}{nF} \ln \frac{c_{Ox}}{c_{Red}}. \qquad (2.81)$$

The following parameters characterise the cyclic voltammogram of such processes:

- The peak potential separation $E_{p,Ox} - E_{p,Red}$ is equal to $59/n$ mV at 25 °C for all scan rates where n is the number of electron equivalents transferred during the redox process.

- The peak current ratio $I_{p,Ox}/I_{p,Red}$ is equal to 1.

- The peak current increases linearly as a function of the square root of the sweep rate ν and are given by the Randles-Ševčik equation

$$i_p = (2.69 \cdot 10^5) \cdot n^{3/2} A c_0 \cdot \sqrt{D}\sqrt{\nu}, \qquad (2.82)$$

where D is the diffusion coefficient.

- The peak potential E_p does not depend on the sweep rate ν.

In practice, complete Nernstian systems are difficult to find as electron transfer between an electrode and a redox-active molecule is often quite slow. The experiments can be made more Nernstian, though, by reducing the scan rate. Moreover, a peak separation of $59/n$ mV is often hard to achieve it depends strongly on the electrode preparation.

$\mathbf{k_{CT}} << \mathbf{k_{MT}}$: Those processes are called irreversible. For this as for all intermediate cases (quasi-reversible systems) both, i_p and E_p are a function of ν and α and the peak separation is larger than $59/n$ mV.

3. Experimental Methods

3.1 Sample Characterization Techniques

The major part of this work deals with the characterisation of thin polymer films and surface modifications including the online recording of adsorption or desorption of analytes. Surface Plasmon Spectroscopy (SPS) as a prominent optical method for the characterisation of dielectrics at surfaces and method of choice in this study permits the detection of such processes on metal substrates and is therefore described in some detail. Since the properties of materials all depend on the thermodynamic parameters temperature and pressure PVT diagrams, for example, are indispensable selecting materials for special applications. Baring this in mind, a high-pressure extension of the normal SPS (HPSPS) is discussed where both, temperature and pressure, may be varied. One disadvantage of the simple SPS is that the sensitivity is not sufficient to characterise small molecular weight adsorbates or samples with low surface coverage. In this case, a simultaneous detection of the fluorescence signal of labelled molecules helps to increase the detection limit (HPFSPS). The combination of HPSPS with cyclic voltammetry (HPCVSPS) provides electrochemical information about the system in addition to its optical properties. However, SPS is only qualitatively able to give some insight into the topology of a surface. For this type of surface characterisation either atomic force microscopy (AFM) or x-ray reflectometry are two techniques that may be employed.

3.1.1 Surface Plasmon Spectroscopy

In the following some experimental issues of surface plasmon spectroscopy are presented beginning with the different types of measurement modes. Starting from the basic angular measurement as already discussed above the time dependent modus is sketched with which adsorption kinetics, molecular switching behaviour or other time dependent surface

processes can be studied. The second part is concerned with the experimental set-up of the normal SPS version and its various extensions.

3.1.1.1 Measurement Modes

3.1.1.1.1 Angular Dependent Measurements

As already explained in chapter 2.1.2 the basic measurement mode is represented by the resonance spectrum, i.e. normalised reflectivity versus angle of incidence, also referred to as scan curve. The angle range of such a scan is important, as it has to cover the edge of total reflection, from which the refractive index of the medium can be determined, and the resonance minimum. The maximum range is limited by the geometry of the high-pressure cells. In the case of the prism cell a maximum range form $\theta_i =10°$ to $\theta_i = 73$ is accessible, for the grating coupling set-up it is $\pm[0.5°; 30°]$ where between -0.5° and +0.5° the detector moves through the laser beam blocking it. The design of the cyclic-voltammetry high-pressure cell only allows for an angle range of $\pm[0.5°; 23°]$. Yet, only a fraction of the maximum angle range needs to be covered in order to get a complete surface plasmon scan. This fraction depends on the refractive index of the prism and the surrounding medium or, in the case of grating coupling, the grating wavelength and pitch amplitude. An advantage of the grating coupling scheme is that the plasmon resonances are close to 0° (normal incidence) and that they can therefore be easily detected in both, negative and positive angle ranges. This eases the alignment procedure in that the features of a scan curve are symmetric with respect to the zero angle position. Experimentally, once the alignment is completed a scan curve can be recorded where in addition to the reflected intensity and the angle of incidence also the parameters temperature and pressure (as well as counts in the case of fluorescence measurements and time in time-dependent studies) are collected automatically by the computer. All necessary equipment is controlled and read by the computer program *Wasplas* written by Andreas Scheller at the *MPIP*, Mainz The obtained scan curves are then fitted according to Fresnel's formulas in order to obtain the thickness and/or refractive indices of the metallic and dielectric layers. The calculations are based on the transfer-matrix method, which is implemented in the software *Winspall* developed in our group. The parameters that have to be provided for the program are the measured reflectivity, the angle of incidence, the thickness and the

dielectric constants of all layers as well as the laser wavelength and the geometry of the coupling prism. By iterative optimisation of the parameters the simulation is fitted to the measured scan curve to determine the optical constants of the involved layers. As already mentioned the thickness and the refractive index of a layer cannot be determined separately for a surface plasmon curve. However the refractive index of the surrounding medium can always be extracted by fitting the edge of total reflection.
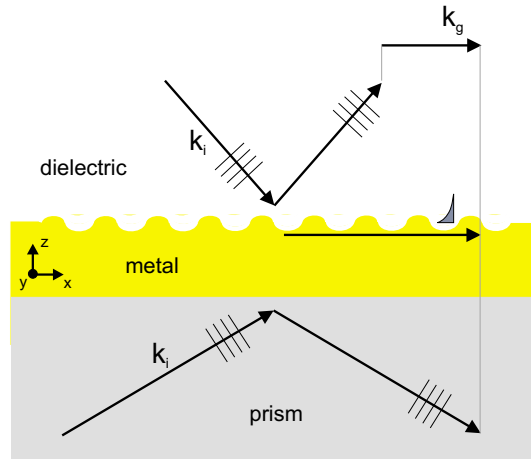

Figure 3.1: Sketch of two techniques to excite surface plasmons on a metal dielectric interface: grating and prism coupling.

Considering surface plasmon spectroscopy as a standard method in biochemistry mostly the prism configuration is implemented in commercially available systems. This is due to several reasons: A flat surface is a well-defined geometry for chemical reactions that are to be investigated. Frequently, the specific binding or adsorption behaviour of molecules is of special interest. In the case of prism coupling the electric field of the surface plasmon and not the one of the incident light interacts with the solvent. The exciting light impinges from the prism side and tunnels through the thin gold layer into the medium to be probed. The optical response of the probed medium, e.g. a flat multilayer system, can easily be calculated using the transfer-matrix method. On the other hand, there are certain cases where the excitation of surface plasmons via gratings is favourable: By choosing an appropriate grating pitch the resonance is observed only a few degrees off from normal incidence. This is an advantage designing high-pressure cells [55; 56]. The use of high refractive index liquids or substrates, which do not have the required optical

properties (e.g.when simultaneously investigating optical and rheological properties of thin films with quartz microbalances) represents another example. However, one of the major disadvantages of the grating coupling technique is the analysis of the data. The rigorous simulation of data is based on the complete characterisation of the grating as already outlined in chapter 2.1.2.2.2. This procedure is time consuming and requires much computer power. An easier, yet less accurate procedure is to convert the data, measured by means of grating coupling, to fictive prism coupling data, which can then be easily evaluated with the transfer-matrix method. As depicted in figure 3.1, the excitation of a surface plasmon requires momentum matching of the coupling light and the surface excitation and does not depend on the way (prism, grating) the momentum of the light is produced. Assuming that the coupling with the surface plasmon does not change the momentum of the light the only change in momentum due to a dielectric layer is the same for both experimental methods. The angles of incidence $\theta_{grating}$ of a grating experiment obtained in the first diffracted order of the grating can then be converted to those of an introduced fictive prism experiment θ_{prism}:

$$k_g + n_d \cdot k_0 \cdot \sin \theta_{grating} = k_{x,SP} = n_{prism} \cdot k_0 \cdot \sin \theta_{prism} \qquad (3.1)$$

k_g is the absolute value of the reciprocal grating vector, n_d and n_{prism} the refractive indices of the dielectric and the prism, respectively, and k_0 is the absolute value of the wavevector of light in vacuum. In reality additional loss channels due to the finite thickness of the gold layer cannot be neglected. However, Maximilian Kreiter showed [57] that despite this fact the conversion evaluation method still gives the right values within an error of less than 1% if the amplitude of the grating is sufficiently small.

3.1.1.1.2   Time Dependent Measurements

Time dependent measurements or, for short, kinetic measurements represent the second type of measurement modus. Here, the changes of the refractive index and/or the thickness with time are monitored. Two different kinds of modi each with advantages and disadvantages can be distinguished:

The first type records the reflectivity at a fixed angle (cf. fig. 3.2). In order to get meaningful data. It is important that the reflectivity R around the fixed angle is a linear function of the angle of incidence θ_i. Therefore, the fixed angle has to be chosen to be in

the linearly decreasing part of the resonance curve. Two assumptions are made: Firstly, a change of the refractive index as well as a change in thickness of the dielectric or an additional layer causes a linear shift of the resonance angle. Secondly, the resonance curve itself does not change its form but is only shifted to a different angle. If these assumptions are satisfied the change in reflectivity can be converted into refractive index or thickness changes and the initial and final values can be determined from scan curves prior and after a kinetic measurement. The advantage of this type of measurement is the high time resolution. Since the angle of incidence is kept fixed the resolution only depends on the integration time of the lock-in amplifier and typical values are 0.4 s to 5 s.
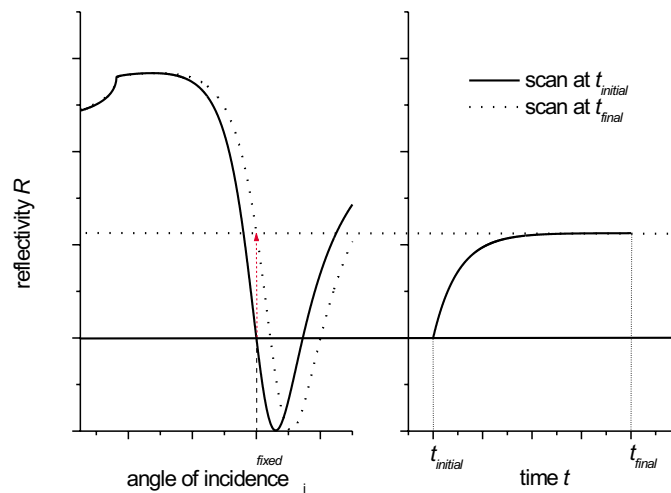
Figure 3.2: The left graph shows two scan curves measured before and after adsorption, the right one, a possible adsorption process at a fixed angle θ_{fixed}.

In the second mode the reflectivity is not measured at a fixed angle but rather at the angle of the minimum of the resonance curve (cf. figure 3.3). An algorithm determines the reflectivity at an angle, which is pre-set and supposed to be the minimum angle. Afterwards two reflectivity values equally distant from the first angle are taken. Through these three points a parabola is fitted. The angle for the minimum of the parabola serves as starting angle at which the next data point is taken. In case of very fast processes a correction algorithm ensures that the goniometer moves further on to lower reflectivities until a parabola fit is feasible. Thus, the method follows the actual minimum of the

resonance curve and the fitting parabola additionally gives some information about the half-width of the resonance. Furthermore, the procedure does not require the assumption of linearity as it is necessary in the first method. Another advantage is that any angle shift can be recorded whereas the former method is restricted to shifts not larger than the half-width of the resonance minimum. In comparison with the fixed-angle measurement the disadvantage of this method is the low time resolution. For each value three angle positions have to be adjusted and the lock-in amplifier always has to be read out. Depending on the hardware (motors, amplifier and detector) this may take up to 5 s - 8 s.
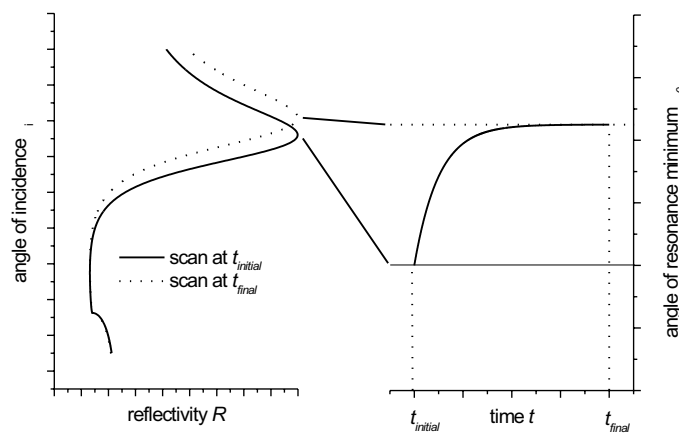
Figure 3.3: Left graph: Angular scans at $t_{initial}$ and t_{final}. Note that the axis have been swapped. Right graph: Typical adsorption plot for a dielectric recorded at the resonance minimum.

3.1.1.2 Measurement Setup

All variations of the SPS set-up discussed in this section are based on one fundamental set-up scheme, which will be referred to as normal SPR set-up. Starting from this normal set-up different extensions will be introduced in the respective subsections.

3.1.1.2.1 Surface Plasmon Spectroscopy

Figure 3.4 depicts the basic surface plasmon spectroscopy set-up including two minor extensions. In general, a HeNe laser with a wavelength of $\lambda = 632.8$ nm (*Uniphase*) is used. The beam is lead through various apertures, firstly, to ensure a safe set-up and,

secondly, to aid the alignment of the laser beam. Then, it passes through a chopper (*PerkinElmer*), which is set at best to a reference frequency chosen to be a prime number in the kHz range. The frequency of the periodically modulated laser light can be separated from all other frequencies so that a reliable measurement with additional background light sources like for example daylight is possible. Before the mirror (*Owis*), used to compact the set-up, re-directs the light it goes through two polarisers (*Bernhard Halle*). The first one regulates the intensity whereas the second one fixes the plane of polarisation; i.e. in the case of surface plasmon excitation p-polarisation is chosen. The laser beam is then focussed by a lens (focal length $f = 200$ mm, *Owis*) and hits the sample (prism or grating) mounted on top of the inner table of a θ-2θ goniometer (*Huber*). The inner table sets the
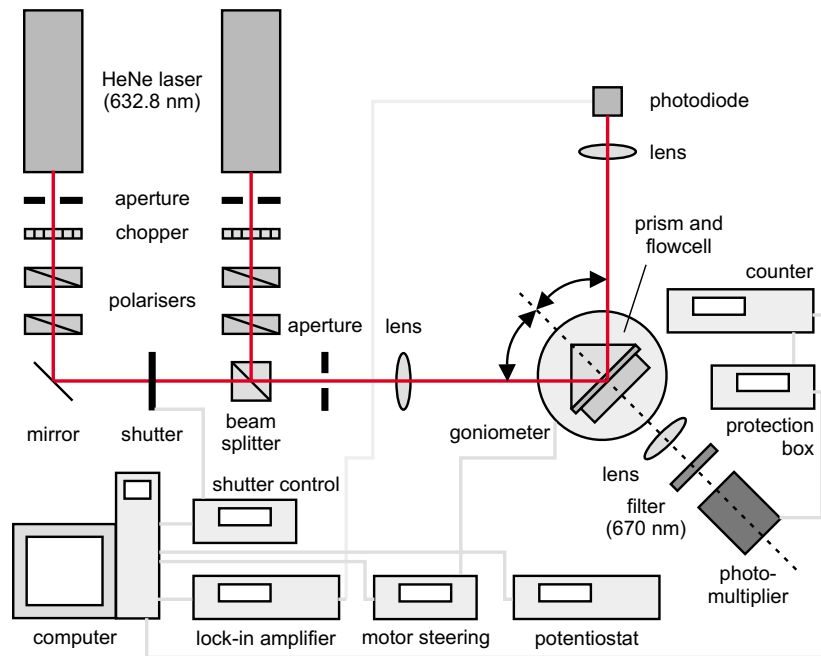
Figure 3.4: Sketch of a surface plasmon spectrometer set-up including various extensions. The position of the high-pressure cell is symbolised by a prism.

angle of incidence θ. The outer table of the goniometer adjusts the 2θ angle relative to the direction of the impinging light necessary to detect the reflected beam. It also serves as platform for the mounting of the detector (Si-photodiode). The goniometer is controlled by two 5-phase step-motors (*Berger-Lahr*), which provide for a $1°/1000$ resolution. In the case of a prism sample the 200 mm lens is replaced by an lens with a focal length of 50 nm (*Owis*), which is placed immediately in front of the detector. (In a grating set-up

such a lens would distort the measurement in that it blocks the laser light at crucial angles, i.e. near the edge of total reflection.) A lock-in amplifier (*PerkinElmer*) finally reads out the signal of the detector, which is directly proportional to the intensity of the reflected light, integrating over many oscillations. (Typical integration times are $\tau = 50$ - 250 ms.) Light from an optional second laser is superimposed on the light from the first one by means of a beam splitter (*Bernhard-Halle*) after it has passed through an aperture, a chopper, and two polarisers. The second laser, also a HeNe laser ($\lambda = 632.8$ nm) serves as a source for s-polarised light or light at a different wavelength. Since surface plasmons can only be excited by p-polarised light this extension to the normal set-up is used for simultaneous recording of reflectivity scans measuring waveguide modes in s- and p-polarisation. When dealing with fluorophores, excited at a surface by means of a surface plasmon resonance, another set of supplements extends the versatility of the standard set-up. The emitted fluorescence light is collected behind a flow cell constructed of quartz glass (*Herasil, Schott*) [58]. A lens ($f = 200$ mm, *Owis*) focuses the light through an interference filter ($\lambda = 670$ nm, *LOT*) onto a photomultiplier tube (*Hamamatsu*). The tube is connected to a protection box (*MPIP*) from where the pulsed signal is lead to a counter (*Hewlett Packard*) whose DC-signal is then read by the computer.

All standard surface plasmon experiments are usually performed with a LaSFN$_9$ glass prism and an LaSFN$_9$ sample glass slide ($n = 1.845$). The metal-coated side of the sample is facing the cavity of a flow cell and the contact sample/cell sealed by an O-ring made of Viton. The other side of the sample is index matched to the coupling prism. This prevents an increased and undesirable reflection of the exciting light at the two glass/air interfaces between both glasses. The refractive index of the index-matching fluid ($n = 1.700$, *Cargille*) is a compromise between optimum index matching properties and minimum volatility.

3.1.1.2.2 High-Pressure Surface Plasmon Spectroscopy

In terms of optics nothing changes when switching from normal to high-pressure SPS. The only difference consists of the high-pressure cell, which replaces the normal prism/sample/ flow cell construction. Again there are the two possibilities to excite surface plasmons, namely prism and grating coupling. For both methods Gerd Kleideiter [56; 4; 59] constructed during his Ph.D. thesis in co-operation with the mechanical workshop at the

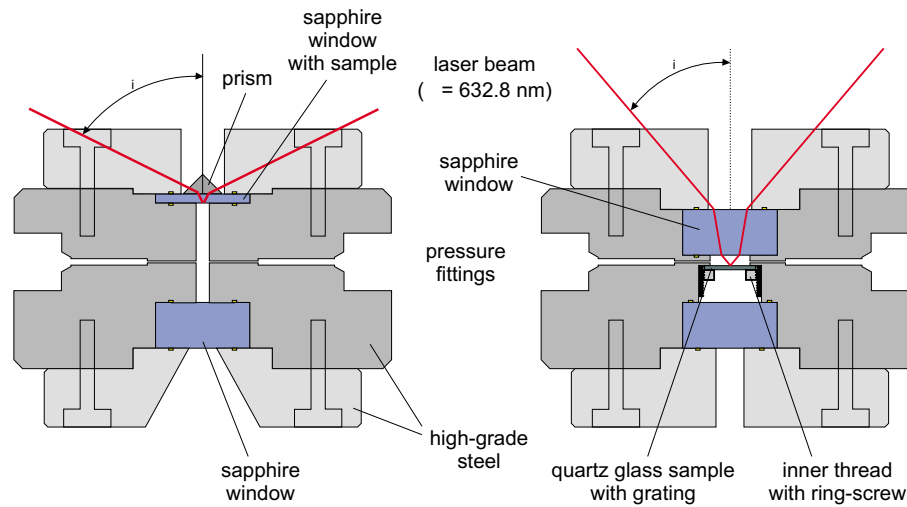Universität Osnabrück high-pressure cells, which are both shown in figure 3.5.

Figure 3.5: Cross-section of two high-pressure surface plasmon spectroscopy cells. The left panel shows a prism-coupling cell, the right one a grating-coupling cell. Both cells have a slit in the upper flange (opening angle range 150° and 62°, respectively) to let the light beam fall onto the sample. The sealing is done by means of gold or Viton O-rings in-between the cell body and the sapphire windows.

A sort of standardised cell body (90 mm × 90 mm) is produced in special tensile-strengthened high-grade steel (type 1.4057). Different internals and flanges then provide for the details of the two cells. The optical windows are made of sapphire (diameter = 24 mm, thickness $d = 2.5$ mm (prism cell) and $d = 12$ mm (grating cell); *Kelpin*). Due to the birefringence of sapphire the thin windows have C-plane cut (optical axis perpendicular to the surface) and the thick ones A-plane cut (optical axis parallel to the surface). Due to the different thicknesses of the windows the prism cell can only be operated up to 100 MPa whereas the grating-coupling cell withstands pressures up to 200 MPa. The windows are sealed using gold O-rings of different sizes and a torus diameter of 1 mm. Although there is the option of inner (between cell body and window) and outer (between window and flange) sealing usually the inner one, especially in the case of the prism-coupling cell, is used. To accomplish experiments of varying temperature there is a heating jacket, which fits around the cell. The mass of the cell amounts to approximately 4.5 kg to 5 kg plus an additional 5 kg of the heating jacket. The heating jacket has 4

heating cartridges (200 W), controlled by a PT100 temperature sensor, built in, which are connected to a temperature-controlling unit (*MPIP*). This unit does not only control the heating devices but also measures the temperature (PT100, *Pressure Technology GmbH*) and the pressure inside the cell volume. The values are sent to the computer. The pressure sensors (*Pressure Technology GmbH*) can probe a maximum pressure of $p = 400$ MPa or $p = 100$ MPa and have an absolute accuracy of $\Delta p = \pm 2$ MPa or $\Delta p = \pm 0.25$ MPa (class 0.5 or 0.25), respectively. The wiring of the presure sensors is solved by using HP-fittings. Additionally, the cell has a fitting used to apply pressure.
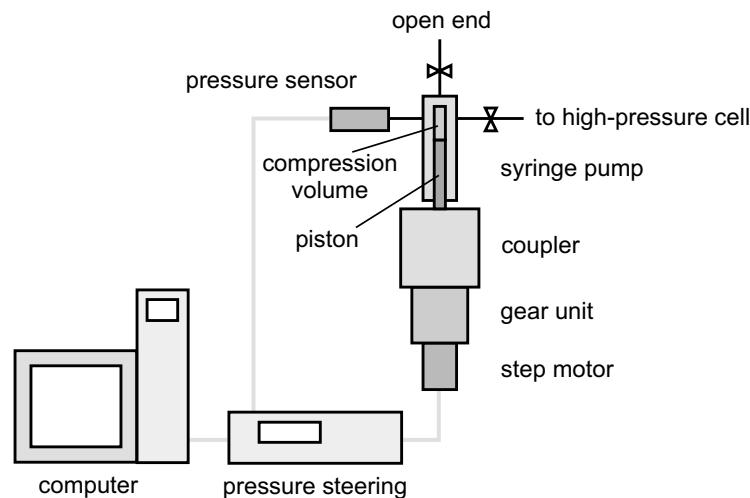
Figure 3.6: Sketch of the pressure generator. The syringe pump and the pressure steering are designed for a maximum of p = 400 MPa.

The assembly of both cells follows different routes: Since in the prism cell the sample itself acts simultaneously as one of the windows it has to be exchanged and again resealed before each measurement. The prism is positioned on top of the sample using a drop of index-matching fluid and its position is fixed with respect to the cell using a special fixing device. In the case of the grating cell the front window stays fixed with the optical axis perpendicular to the plane of incidence. The grating (sample size: diameter = 12.5 mm, $d = 2$ mm) is replaced from the backside. The grating, fixed by a screw, is oriented such that the grating vector is parallel to the plane of incidence.

A syringe pump (*Nova Swiss*) generates the pressure (compare fig. 3.6). It is automatically driven by a stepper motor connected to a gear (reduction 1:64) and a coupling unit. A pressure sensor that is connected to the pump serves as input for the pressure

steering device (*MPIP*). However, pressure jumps due to mechanical relaxations etc. in the connection parts of the cell or the pump complicate the regulation of the pressure. Therefore, always a linear approach of the set pressure from lower pressures is chosen to circumvent sudden volume changes.
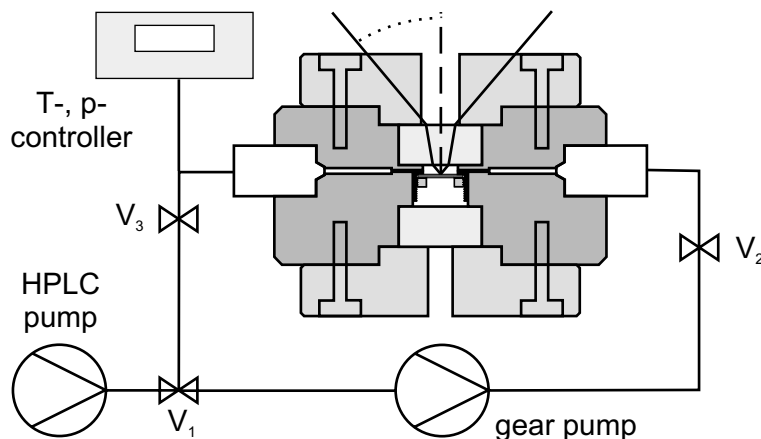

Figure 3.7: Diagram of the pressure generator and mixing unit for the PMMA-MMA-CO_2 interaction measurements. The HPLC pump pressurises the mixing circuit. The gear pump is the mixing unit. The whole circuit is kept at elevated temperatures by means of heating belts (not shown) to avoid temperature sinks in the circuit. The valves V_1, V_2 and V_3 disconnect the mixing circuit from the HPLC pump and the measurement cell.

In the case of the measurements in supercritical carbon dioxide and for the PMMA-MMA-scCO$_2$ interaction in particular a different type of pressure generation procedure is used. Since carbon dioxide comes in gas cylinder with an internal pressure of approximately 6 MPa a syringe pump is not suitable to compress the carbon dioxide that is still in the gas phase. CO_2 is gaseous at ambient conditions however gets fluid when cooled down to about 0 °C - 10 °C. It can then be compressed by a high-pressure liquid-chromatography pump (HPLC, PU1508 *Jasco*). If the pressure medium is pure carbon dioxide and high pressures (above 50 MPa) are required the HPLC is not powerful enough so that the syringe pump is filled with liquid carbon dioxide and cut off from the HPLC pump. Then, the normal pressure-generating set-up, as described above, is re-established and can be used as explained before.

For the measurements of the PMMA-MMA-CO_2 interaction (see 6.2) a different approach

has to be chosen. Since the MMA has to be mixed vigorously with the carbon dioxide to get a homogeneous solution a high-pressure circuit, as shown in figure 3.7, is built up. The right amount of MMA is injected into the gear pump, which is disconnected from the measurement cell by a set of valves. Then carbon dioxide is added, the HPLC pump disconnected and the mixture stirred at elevated temperatures by the gear pump. The tubes leading to and from the cell are heatable in order to avoid temperature sinks while mixing. To increase the pressure additional CO_2 is fed into the circuit and the mixing procedure is resumed.

3.1.1.2.3 High-Pressure Surface Plasmon Enhanced Fluorescence Spectroscopy

The extension of the high-pressure surface plasmon set-up to allow fluorescence detection is straight-forward. All modifications to be made are the mounting of a photomulitplier with a lens and a filter behind the pressure cell. The photomultiplier is connected via a
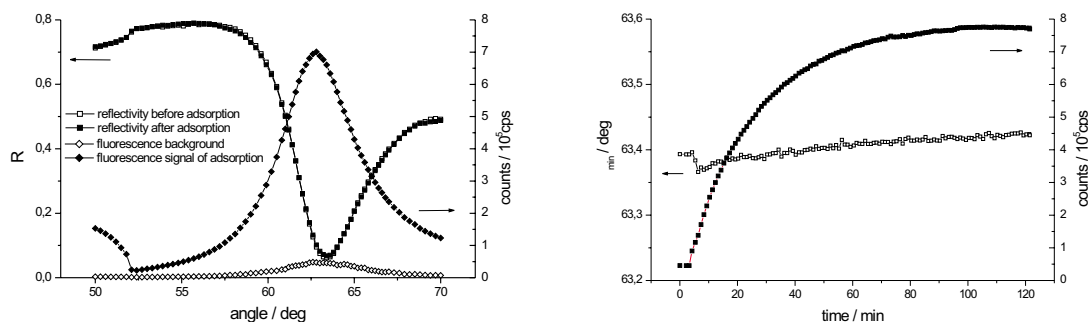
Figure 3.8: The adsorption of fluorescent labelled DNA targets onto a sensor surface. Counter scans (left panel) before and after the adsorption are plotted and the corresponding time-dependent minimum angle curves (right) are shown. Note that the SP minimum doesn't shift due to the low molecular weight of the target while the fluorescence signal increases in both scan and kinetic.

protection box and a counter to the computer. Since in the case of grating coupling a laser beam incident on the fluorescent labelled medium excites fluorophores in the solution and hereby produces a rather high background signal the coupling mean of choice is the prism. Thus, only the surface bound wave excites the fluorophores, which relax by emitting light. The fluorescent light is collected and amplified by the photomultiplier.

The other advantage of the prism cell is that it can be operated in 'transmission' mode. No spatial problems occur as compared to the grating coupling, where the fluorescence light is emitted in the same direction into which the incident laser beam is reflected.

The fluorescence extension is also fully computer controlled. A typical example for counter scans before and after the adsorption of DNA target oligonucleotide is shown in figure 3.8. Due to the low molecular weight of the analyte used virtually no change of the resonance minimum and the reflectivity can be found. Since the hybridisation is rather slow the kinetic mode, which follows the minimum, is chosen. Especially in high-pressure applications, where the whole resonance curve is shifted to higher angles due to the increased refractive index of the medium at elevated pressures this has to be the mode of choice. If the measurements were performed at a constant angle the resonance curve would shift and with it the fluorescence curve. This fact would make it difficult to distinct whether the final effect is caused by the shift of the fluorescence curve or the actual processes occurring in the system.

Before making the adsorption experiments a background scan with pure buffer solution is recorded. As can be clearly seen, the background scan shows a slight dependence on the angle of incidence. At low angles, smaller than the angle of total reflection, a slightly higher background is detected than for angles larger than the critical angle. The higher background for small angles can be explained by light transmitted through the interference filter whereas for larger angles all laser light is reflected and the background is low. The excitation of fluorophores in the surface plasmon field leads to a fluorescence intensity, which is increased after the adsorption of a labelled oligonucleotide. The maximum of the signal is located close to the resonance minimum, where the excitation of the surface waves is most pronounced [58; 7]. The background scan, though, also shows an increased intensity at the same position. One would assume the background to be more or less constant [58] but due to an increased adsorption of the analyte at the cell walls, which could not be completely removed with extensive cleaning, a comparatively high background fluorescence signal is still observed.

The right hand side of fig. 3.8 depicts the time-dependent measurement of the adsorption of the DNA target at the sensor surface. The fluorescence signal starts from the background signal of about 40000 cps and increases to a value about 20-fold higher (800000 cps) induced by the hybridisation reaction. The angle of the surface plasmon resonance

minimum does not change significantly so that the fluorescence extension clearly increases the sensitivity of surface plasmon spectroscopy. However, the measured intensity is not directly convertible to the number of adsorbed fluorophores. For this purpose the intensity would have to be calibrated using the thickness of the adsorption layer, which is not accessible due to a lacking shift of the surface plasmon resonance.

3.1.1.2.4   High-Pressure Cyclic Voltammetry Surface Plasmon Spectroscopy

Another extension to the normal SPR experiment is cyclic voltammetry. To be able to combine these two techniques another type of high-pressure SPR cell had to be constructed. It allows standard surface plasmon spectroscopy measurements at elevated
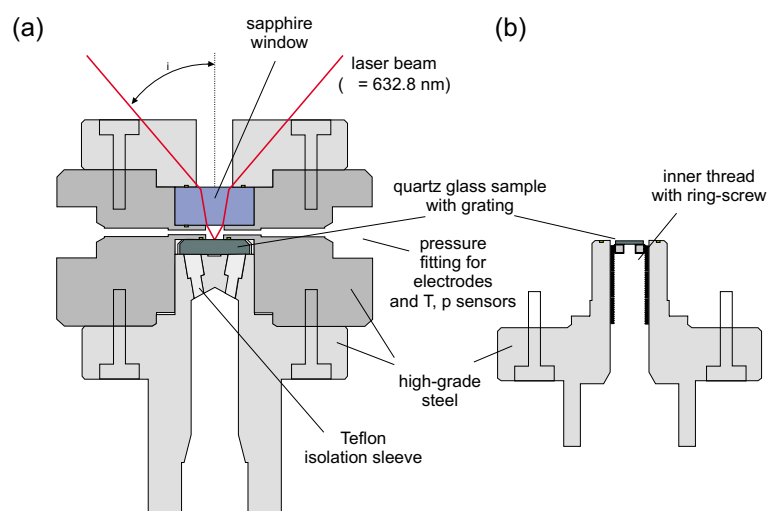
Figure 3.9: a) Sketch of the high-pressure electrochemistry surface plasmon cell. Note the four fittings for pressure setting, the temperature sensor and the counter and reference electrode. The sample is fixed on the backside flange, its evaporated gold working electrode contacted by means of a wire and the whole assembly then inserted into and attached to the cell body. b) An extra flange opens the opportunity to perform normal high-pressure experiments at up to 200 MPa as compared to the maximum 100 MPa of the electrochemistry version.

pressures and temperatures and additionally features the possibility to perform electrochemical experiments. This cell was built as well in co-operation with Prof. Dr. M. Lechner at the *Universität Osnabrück* and developed from a standardised body shape (c.f. figs. 3.9a and 3.5). A gold O-ring between the cell body and the thick sapphire

window seals the top part of the cell. Apart from the size and shape of the middle part the rest of the cell is changed in order to accommodate the electrodes.

In this grating-coupling cell the sample (diameter 15 mm, thickness 4 mm) is located in the middle of the cell body. However, in contrast to the previously described grating-cell version the backside of the sample must not get into contact with the pressure medium to avoid electrical contact with the wires that lead to the gold electrode. The sample is therefore sealed from the fluid cell by means of a Viton O-ring ($\emptyset$ = 6.5 mm, *Gottwald*). The gold surface is the working electrode and its slanted edges are contacted from the backside of the cell with simple electrical wires, which are pressed into contact with the gold surface by means of a Teflon fixture. As an alternative to the wire contacts commercially available spring contacts (*INGUN Prüfmittelbau GmbH*) can be used. The spring contacts require holes in the sample, which are filled with electrically conducting glue (Epo-Tek H20 E-frozen, *Polytec*).
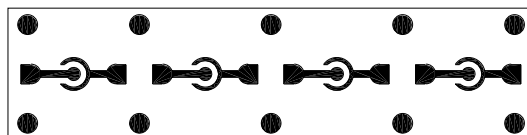
Figure 3.10: Sketch of an evaporation mask used to evaporate the working and optional counter electrode onto the sample.

There are also two options for the counter electrode: One is an additional electrode, which is evaporated onto the sample together with the working electrode by means of a mask (*Elaser*, c.f. fig. 3.10). It is contacted in just the same way as it is done in the case of the working electrode. The more simple approach is a commercially available electrical high-pressure contact (*Sitec*), which is attached to the cell through one of the four fittings leading to the fluid cell in front of the sample. The same kind of contact is also used for the reference electrode. In both cases either a platinum or a thin silver wire (*Chempur Feinchemikalien und Forschungsbedarf GmbH*) is soldered to the contact of the respective electrode. A temperature sensor occupies the third fitting in the main body of the cell and the fourth is used to apply pressure and to fix the pressure sensor. The volume in front of the sample is considerably smaller than in the former cell types (6 mm in diameter, 5 mm thickness). To make it easier to load the cell and check the contacts the sample is

fixed onto the inside of the backside flange, which is then attached to the cell.

A second backside flange (c.f. fig. 3.9b) allows measurements up to 200 MPa as compared to the maximum of 100 MPa for the electrochemical version. The sample (diameter 10 mm, d = 2 mm) is fixed inside of this second flange with a screw and the hole is finally sealed with a plug (*Sitec*). A remote controlled potentiostat (263A-2, *PerkinElmer Instruments*) sets the potential.

3.1.2 Atomic Force Microscopy

Atomic force microscopy (AFM) is a scanning probe microscopy technique [60]. It allows a rather non-destructive three-dimensional picture of the surface with a lateral resolution in the Angstrom range and a resolution perpendicular to the surface of 1 nm [60]. Since it does not require the surface to be conductive as it is the case of scanning tunnelling microscopy AFM has become a widespread method to characterise surfaces. Various materials including insulators, organic materials, biological macromolecules, polymers, ceramics, or glasses in different environments such as liquids, vacuum or low temperatures can be investigated.
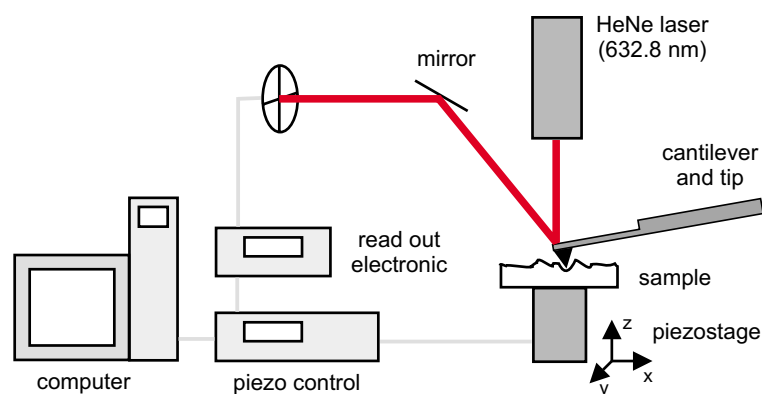
Figure 3.11: Sketch of an atomic force microscope.

The AFM consists basically of three parts (cf. figure 3.11): A fine tip at the end of a triangular or bar shaped cantilever spring serves as the probe. A scanner constructed of piezoelectric ceramic tubes moves the sample underneath the tip (or the tip over the sample) in all three directions. A laser beam is reflected off the backside of the cantilever and is then directed onto a two- or four-quadrant photodiode. This way small motions

(deflections and torsions) of the cantilever are amplified and the photodiode converts the motions into voltages.

AFM operates by measuring attractive or repulsive forces acting on the tip [60]. Principally, there are three detection modes: In the contact mode, the tip is in touch with the surface while the deflection of the cantilever is kept constant. Topological changes while scanning lead to deflections of the tip, which are then compensated by moving the piezo stage perpendicular to the surface (constant deflection mode). Therefore, a contour map of the sample surface is produced and a friction map may be constructed. The AFM pictures shown in this work, however, are taken in tapping mode. In contrast to the contact mode it is a dynamic method. The cantilever is excited slightly below its resonance frequency and the distance to the surface is adjusted such that it barely touches the surface at its turning point. As the measurements are performed in the regime of attractive forces the resonance frequency of the cantilever moves to higher values upon changes in the topography. The resulting lower amplitude is balanced by electronics and the feedback converted to a contour map. The advantage of the tapping mode is its minimised force on the sample.

3.1.3   X-Ray Reflectometry

X-ray reflectometry is a useful tool to study thin and ultrathin films and layer architectures from about 2 nm to 5000 nm. The typical x-ray wavelength used is of the order of an Angstrom (Cu: $K_\alpha = 1.54$ Å). Since the refractive index of the materials at very small wavelengths is slightly less than unity total external reflection occurs at very small angles of incidence (measured from the surface, compare fig. 3.12). At angles above the critical angle x-rays start to penetrate the material. At the interface between two layers the radiation is partly reflected partly transmitted (refracted) into the layer below. In this technique the behaviour of the radiation at the surface can be described with Fresnel's equations. Having a mono- or multilayer film on a reflective substrate the total film thickness is reflected in interference patterns called Kiessig fringes [61]. These Kiessig fringes can be fitted with Fresnel's formulas [62] to reveal information about the layer thicknesses (frequency of the oscillations), the surface roughness (attenuation of the fringe amplitude), electron density of the layers (also influences the amplitude of the resonances),

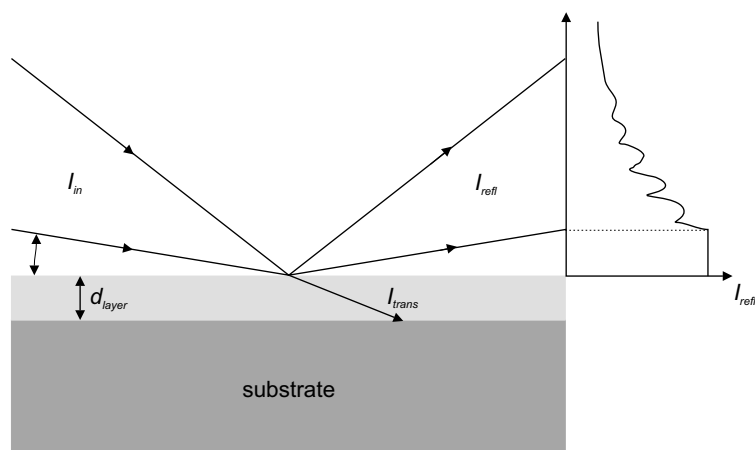and the density of the surface layer (position of the critical angle).

Figure 3.12: Simplified ray diagram of x-rays reflected from the substrate interfering constructively and destructively. A series of interference fringes develops with the fringe spacing being related to the film thickness.

The intensity range measured in a reflectivity curve typically covers six or more orders of magnitude so that a detector with a high dynamic range, usually a scintillation counter, is needed. In general, a line source of x-rays is used such that at gracing incidence a very large area (some cm^2) of the sample is illuminated. Conventional x-ray reflectometers employ the coupled motion of the sample and a point detector. More elaborate reflectometer models use line detectors instead of point detectors and no moving parts are necessary any more and the measurement gets considerably faster [63; 64].

3.2 Sample Preparation Techniques

In the following the techniques used to prepare and modify sample substrates are explained. Most of the surface plasmon measurements were performed in the grating-coupling mode. Therefore, the various steps needed to produce surface gratings are described. Once the grating modified sample has been made it can be re-used as substrate for many measurements, only the top layers like gold films and the dielectric layers to be studied have to be removed repeatedly. The techniques illustrated cover basic methods such as thermal evaporation, self-assembly of organic material and spin-casting. More elaborate surface modifications that are related to the different material systems presented

in this work will be discussed in the following section.

3.2.1   Fabrication of Gratings

The main steps for producing shallow gratings (depth-to-pitch ration smaller than 0.1) in a glass substrate as needed for surface plasmon spectroscopy are shown in figure 3.13. A grating structure is holographically written into a thin photoresist film that was spin-cast onto a fused silica glass substrate. For high-pressure applications round slides of dimensions 12.5 mm × 2 mm, 10 mm × 2 mm, or 15 mm × 4 mm are used depending on the measurement cell used. After the development of the photoresist the grating is transferred into the glass substrate by standard photolithographic techniques. The complete preparation of the surface gratings was done in the cleanroom (class 100) of the Max-Planck-Institute for Polymer Research in Mainz.
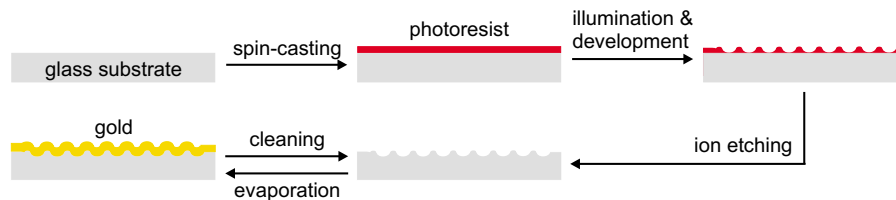
Figure 3.13: Fabrication procedure of shallow surface gratings.

Prior to any further modification the fused silica slide (optical quality, *Sico*, *Hellma*) was cleaned thoroughly using the procedure described below. Then the photoresist layer (*Shipley*, *Microresist Technology*) is deposited on the glass surface by spin-casting. Pre-treating the surface with liquid hexamethyldisilazane primer (*Shipley*) enhances the adhesion of the photoresist to the surface: First, the cleaned sample lying on the spin-coater is completely wetted by the primer. After 30 s without spinning the surplus of primer is spun off at 4000 rpm for another 30 s. Immediately afterwards a diluted solution of the photoresist (thinner, *Shipley*, *Microresist Technology*) is applied (Depending on the size of the sample usually 3 to 4 drops are applied to avoid bulges at the edge of the glass slides.) and spun off at 4000 rpm for 60 s. For symmetric grating structures photoresist thicknesses of around 100 nm are favoured because the enhanced stability of the photoresist. In order to remove the residual solvent, the film is annealed at 95 °C under vacuum (softbake)

before a grating structure is holographically written into the film.

Writing the gratings [65] requires the use of a TE-polarised HeCd laser ($\lambda_{HeCd} = 442$ nm, *Optilas*). The beam passes a spacial filter with a subsequent lens to produce a parallel beam with an area of a few cm^2. The homogeneously illuminated inner area of the beam is partly directed onto the sample and partly reflected from a mirror onto the sample. Depending on the phase difference between these two light paths there is either constructive or destructive interference on the sample. Ideally, the intensity distribution on the surface is sinusoidal with a period Λ of

$$\Lambda = \frac{\lambda_{HeCd}}{2 \cdot \sin \theta}. \tag{3.2}$$

The angle θ is defined as the angle between the optical axis and the normal to the sample surface. In order to reduce interference effects from laser light being reflected at the backside of the sample black adhesive tape is attached to the backside. The subsequent development of the film (*Shipley, Microresist Technology*) erodes the photochemically modified areas of the photoresist and leaves a surface relief grating. The optimum development depth is reached when the bare glass surface appears where the intensity maxima were located during the illumination process. Usually the development time is kept constant at 30 s and the illumination time is varied until the best result is achieved.

The photoresist grating is transferred into the glass substrate by means of exposure to an ion beam (ion mill, *Roth & Rau*). For symmetric gratings an etching angle of 0°, i.e. normal incidence of the ion beam onto the sample, is chosen. A mixture of the reactive gases O_2 and CF_4 is optimised for etching fused silica. The etching mechanism is a combination of mechanical ablation (sputtering) and chemical etching by the radicals of the reaction gases. The etching rate for photoresist is 20 nm/min and for fused silica 40 nm/min. Typical etching times are 25 s to 45 s.

3.2.2 Cleaning Procedure

Residual organic coating on the sample can be removed by exposure to piranha solution (H_2O_2 and H_2SO_4 in the ratio 1:2). Old metal films are easily removed by either aqua regia (HCl and HNO_3 in a ratio 3:1) or a iodine solution (40 g iodine, 40 g potassium iodide and 100 ml MilliQ water). If a chromium adhesion layer is used it can be removed in a solution of ammonium cerium (IV) nitrate (99%, 12 g in 50 ml water, *Aldrich*).

Once all organic or metal coatings have been removed the samples are further cleaned by the following procedure:

- 10× rinsing in purified water (MilliQ, *Millipore*)

- 15 minutes cleaning in an ultrasonic bath with a solution of 2% detergent (Hellmanex, *Hellma*) in MilliQ water

- 15× rinsing in purified water

- 5 minutes cleaning in an ultrasonic bath with ethanol (Chromasolv, *Riedel-de Haehn*).

- Drying of the glass samples in a flow of nitrogen

3.2.3 Thermal Evaporation of Metal Layers

The metals gold and silver needed for surface plasmon experiments are thermally evaporated [66] onto the sample in commercially available evaporation chambers (*Balzers*, *Biemtron*). For prism experiments layer thicknesses between 45 and 50 nm are evaporated, depending on the metal (purity 99.99%). For substrates with a grating coupler a thickness exceeding 150 nm is used in order to be able to consider the metal thickness as infinitely thick in the optical analysis. In both cases the evaporation is started at a vacuum pressure of around $5 \cdot 10^{-4}$ Pa and the evaporation rate is set to 0.1 nm/s to 0.2 nm/s. In order to enhance adhesion of gold or silver at the surface a thin intermediate layer of chromium (2 nm, 99.9%) can be evaporated first.

3.2.4 Self-Assembled Monolayers on Metals

Self-assembled monolayers (SAMs) are molecular assemblies that are formed spontaneously if an appropriate substrate is immersed into a solution of an active surfactant in a solvent [67; 68]. The popularity of these layers stems from the fact that well-defined and closely packed assemblies can very easily be prepared at ambient laboratory conditions and that the strong co-ordination of the head group of the surfactant to the metal yields a layer that is sufficiently stable to desorption. Moreover, the physico-chemical properties can be tailored by the choice of the end functional group as for example -COOH, -OH, -CH3, or -biotin and by varying the length of the alkyl chain. From a

thermodynamic point of view several parameters promote the assembly process on the surface: Chemisorption of the head-group of the surfactant leads to a strong attractive and exothermic interaction with the surface. Consequently, all available binding sites at the surface are occupied. Additionally, attractive van der Waals interactions between the alkyl chains of the molecules can stabilise the molecular assembly.

Prominent examples of self-assembled monolayers are alkanethiols on gold, silver and copper, several sulfides on gold, alcohols on platinum and carboxylic acids on aluminium oxide. In this work only thiols are used for the adsorption onto gold and silver surfaces. The sulphur groups exothermically bind to the surface whereas the alkyl chains are oriented uniformly at an angle of 30° to the surface normal [58] if an appropriate alkyl chain length, head group and dilution have been chosen.

3.2.5   Spincoating

The well-established technique of spin-casting is used to prepare thin polymer films in the thickness range of a few nanometers to micrometers. The material is dissolved in an appropriate solvent with, if possible, a rather high boiling point. The sample is then covered completely with this viscous solution and the spin-coater (*Headway Research*) is set to rotation speeds between 1000 rpm and 8000 rpm for 60 s. During the rotation the solution is distributed homogeneously over the surface whereas most of the solvent evaporates. The relation between viscosity of the solution and rotation speed sets the final thickness of the film. For the small, round samples that are used in the grating coupling configuration slightly higher speeds and less viscous solutions are preferable in order to get a homogeneous surface coverage.

Subsequent to every spin-coating process the samples are annealed under vacuum for at least 10 hours to let all the residual solvent evaporate. For that, the temperature is set to a value well above the boiling point of the solvent but below the melting point of the respective polymer. Before letting it cool off at a very slow rate to avoid residual stress in the spin-cast layer temperature is raised for some minutes above the glass transition point of the film in order to remove any anisotropies in the film.

3.3   Materials and Surface Modification Procedures

This section describes several types of surface modification techniques. Moreover, all studied systems are presented, i.e. this part is also some sort of an outline for the results chapters. First, a procedure to coat a metal surface with a silica film is presented. This is especially useful for surface plasmon experiments when the chemistry of the material to be studied favours silanol linkage to the surface. One such example deals with hydrogels bound to silica surfaces. In a different set of experiments, surface plasmon spectroscopy is used to characterise DNA hybridisation. In this case, a supermolecular architecture of biotinylated thiol, streptavidin, DNA probe and DNA target is chosen to monitor hybridisation processes as a function of temperature and pressure. Subsequently, the focus is set on supercritical carbon dioxide as pressure medium. Finally, the materials and the measurement procedures used in the cyclovoltametry experiments are illuminated.

3.3.1   Silica Film Preparation Employing Sol-Gel Techniques

One of the basic requirements of surface plasmon spectroscopy and in some cases also one of its major disadvantages is its demand for a metal surface. In some fields such as biochemistry and bioengineering the modification of the molecules in order to attach them to surfaces usually employs silane rather than thiol chemistry. To be able to still use the sensitivity of SPR to characterise these materials the metal surface has to be modified as to provide silanole linkage sites. The easiest method is to evaporate SiO_x thermally. A more stable alternative with respect to the stability in a buffer solution pursuing a sol-gel procedure is given in figure 3.14 [69; 70].

Thin silica films are prepared on metallic surfaces immediately after the Au or Ag deposition, using a combination of self-assembly and sol-gel techniques. During the initial self-assembly step (cf. fig 3.14.1), 3-(mercaptopropyl)trimethoxysilane (3MPT) layers are formed by immersing the substrates in a 20 mM solution of 3MPT (freshly vacuum distilled) in dry ethanol for 2 h (Ag) or 3 h (Au). These films are then rinsed with copious amounts of dry ethanol and Millipore Q-UV-purified water. Further hydrolysis and condensation of the 3MPT is induced immediately following these rinsing steps by immersing the samples in aqueous 0.1 M HCl for 0.5 h - 2 h [71; 72] (compare fig. 3.14.2). These 3MPT-modified surfaces are then rinsed again with copious amounts of water and
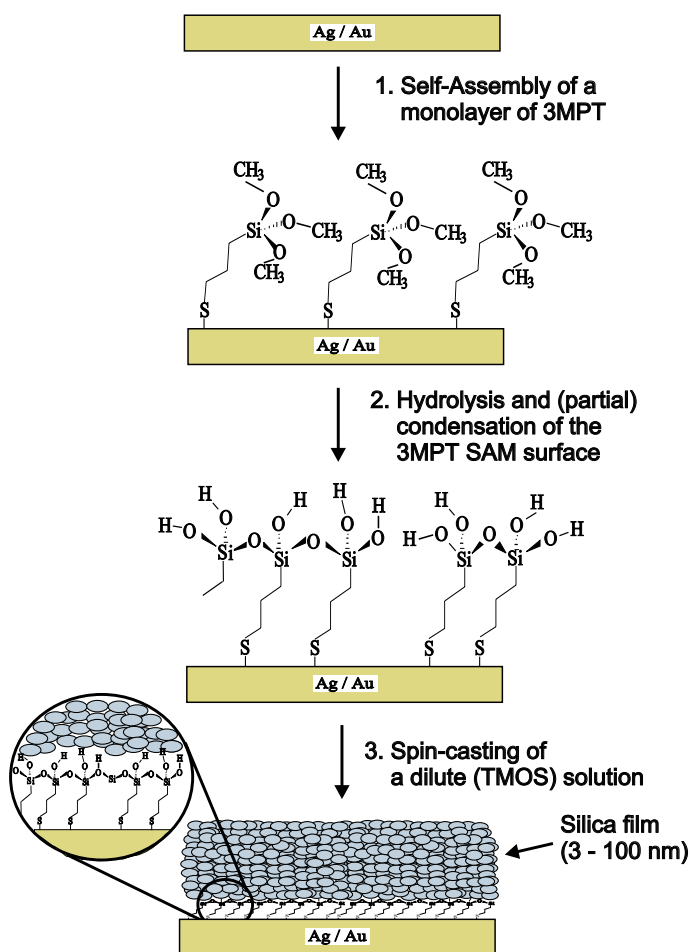
Figure 3.14: Fabrication steps of thin sol-gel silica films formed on metal substrates.

immediately placed on a spin-coater. Small volumes (approx. 45 μl/cm^2) of pre-mixed solutions of tetramethoxysilane (TMOS), methanol, water and 0.1 M HCl delivered on the surface then form silica films. The premixing is done about 30 min in advance to facilitate TMOS hydrolysis prior to deposition. The spin-coater is operated at 3400 rpm for 60 s. The prepared metal/3MPT/SiO$_2$ surfaces are stored in a desiccator at room temperature for a minimum of 2 days to complete the condensation process and to remove any residual solvent (cf. figure 3.14.3). Typical TMOS-solvent compositions and the resulting layer thicknesses are given in table 3.1 as measured by ellipsometry (ELL) [70] and SPR, assuming a refractive index of the film equal to that of dense silica ($n = 1.457$), [73]).

The drying progress of the SiO$_2$ films is studied with a waveguide (ASI2400, *ASI*) consisting of a sol-gel mixture of SiO$_2$ and TiO$_2$. The sol-gel, which sits on a glass substrate

($n = 1.525$), has a refractive index of 1.769 and a thickness of 185.9 nm. Light is coupled into the waveguide by a grating with a grating constant of 416.1 nm.

thickness (ELL)	thickness (SPR)	water	methanol	0.1 M HCl	TMOS
[μm]	[μm]	[μl]	[μl]	[μl]	[μl]
3	0.5	163	55	81	2
8	-	163	55	81	5
15	3.5	163	55	81	10
30	16.7	163	55	81	20

Table 3.1: Thickness/composition correlation of sol-gel films at constant spinning speed. The films characterised by ellipsometry are prepared on gold, the ones measured with the SPR on silver.

3.3.2 Hydrogels on Silica Surfaces

All materials employed are of research grade and are used as received unless indicated otherwise. N-isopropylacrylamide (NIPAAm, monomer), sodium acrylate (SA, ionisable co-monomer), N,N'-methylenebisacrylamide (BIS, crosslinker), ammonium persulfate (APS, initiator), N,N,N',N'-tetramethylethylenediamine (TEMED, accelerator), γ-methacryloxypropyltrimethoxysilane (bind silane), and dimethyldichlorosilane (repel silane) are purchased from *Sigma-Aldrich*, Germany.

The hydrogel is bound to the surface employing silane chemistry [74]. As described above the metal surface has to be modified with the sol-gel process to give a suitable platform for the binding of the initiator molecule to the metal. Consequently, a 15 nm layer of silica is deposited on the gold surface using the procedure described in section 3.3.1. Thin films of NIPAAm gel are cast onto the sol-gel layer using Teflon film spacers according to the procedure of Zheng et al. [75]. For short, this procedure comprises the self assembly of the bind silane on the sample surface and the assembly of a polymerisation cell consisting of the sample (bind silane facing inwards), a Teflon tape as spacer and a cover glass slide with repel silane on the inside surface. The bind and repel silanes are prepared in the following way:

- Bind silane: The pH of 50 ml MilliQ water is adjusted to 3.5 with acetic acid. 200μl bind silane are added, the solution is thoroughly mixed for 20 min, and the sample subsequently immersed in this mixture for 1 h. Then it is rinsed and let dry.

- Repel silane: 0.187 ml repel silane is thoroughly mixed in 1,1,1-trichloroethane. The samples are wiped with the solution and let dry. Remaining spots are removed by wiping the sample again with a dry tissue. Finally the sample is rinsed with water and ethanol and dried with nitrogen.
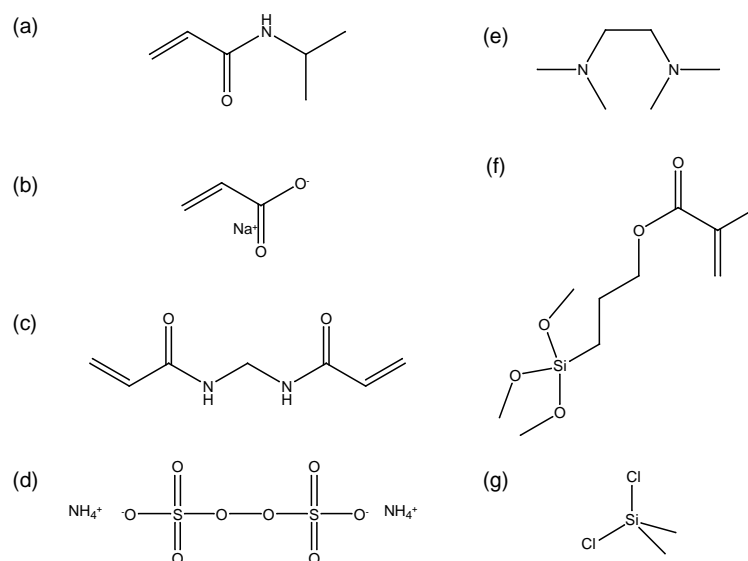
Figure 3.15: Chemicals needed for the NIPAAm film formation: (a) monomer N-isopropylacrylamide (NIPAAm, monomer), (b) ionisable co-monomer sodium acrylate, (c) crosslinker N,N'-methylenebisacrylamide, (d) initiator ammonium persulfate, (e) accelerator N,N,N',N'-tetramethylethylenediamine, (f) bind silane γ-methacryloxypropyltrimethoxy-silane, (g) repel silane dimethyldichloro-silane.

The whole assembly is then put into a small amount of pre-gel solution that is suck into the gap between the two glass plates by capillary forces. The pre-gel solution is prepared by dissolving recrystallised NIPAAm (700 to 630 mM), SA (0 to 70 mM), BIS (3.5 mM to 15 mM), and TEMED (20 μl) in 3 ml of MilliQ water. It is then degassed using at least three consecutive freeze-thaw cycles. 60 μl of a 40 mg/ml solution of APS in MilliQ water is added to initiate the polymerisation, which starts a few seconds after the addition of

the initiator and is let running for at least 1-2 h. The total gel concentration is kept constant, with the sum of the SA and NIPAAm concentrations equalling 700 mM.

The resulting gel films are 40 μm in the swollen state and 4 μm in the collapsed state, as determined by profilometry. This thickness is much larger than the decay length of the surface plasmons into the dielectric, so the surface plasmon mode is only sensitive to the gel-substrate interface and the gel can be modelled as an infinite medium.

3.3.3 Biotin, Streptavidin and DNA

The goal of this work is to study the pressure dependence of DNA hybridisation by means of high-pressure fluorescence surface plasmon spectroscopy. However, special care has to be taken when immobilising biological molecules, i.e. their biological function must be preserved. For this purpose a universal biding matrix consisting of biotin containing molecules and streptavidin is used. In the following an overview of the properties of the biotin-streptavidin binding, the basics of DNA hybridisation and the actual immobilisation of the binding matrix and the DNA will be given.

3.3.3.1 The Biotin-Streptavidin Interaction

The feature that makes the biotin-streptavidin binding such an important combination for diagnostic purposes is on the one hand its extraordinary high affinity and therefore extremely slow dissociation rate ($K_D = 10^{-15}$ M^{-1}) [76; 77], and on the other hand the simplicity of derivatisation of the biotin molecule (vitamin H). Streptavidin is a tetrameric protein (molar mass 4 $\times$ 15 kDa) [78] that is isolated from the bacterium *Streptomyces avidinii* and can bind up to four molecules of d-biotin. This protein and its homologous avidin serve as natural antibiotics by depleting their environment (e.g. egg white) of the vitamin biotin. Figure 3.16 shows the structure of steptavidin as determined by x-ray scattering [79; 76] (dimensions 5.6 nm $\times$ 4.2 nm $\times$ 4.2 nm [80]) including its four binding pockets where four biotin molecules are bound (black). Biotin (cf. fig. 3.16) is bound to the pockets via hydrogen bonding. It reaches 1-2 nm into the protein host molecule but the carboxylic group of the vitamin is still accessible from the outside of the protein. For this reason, biotinylated molecules such as DNA, peptides or proteins can easily be attached to streptavidin. However, it has been reported [81] that when the derivatives

of biotin are too bulky the binding affinities are reduced, which is mainly attributed to steric hindrance [79]. Due to the symmetry of streptavidin bulky ligands are not able to bind to all four binding pockets.
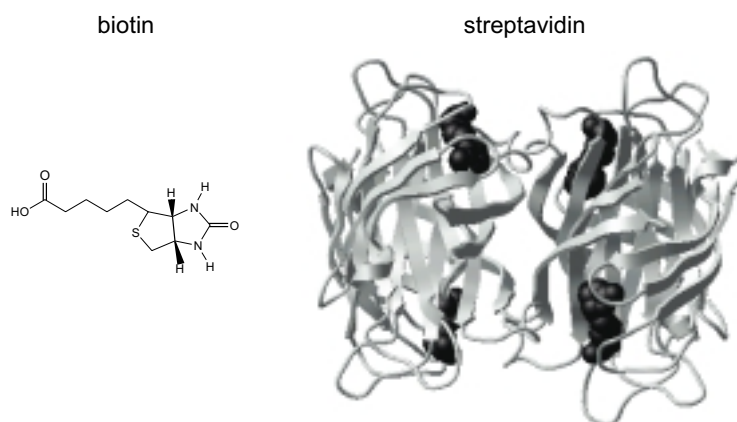

Figure 3.16: Biotin offers a carboxylic function that can be used to couple biological molecules. A maximum of four biotins bind (indicated in black) to the protein streptavidin with high affinity.

Nevertheless, the biotin-streptavidin system can be used to construct supramolecular architectures on surfaces [82; 83; 84] that may serve as universal binding matrices for further modification with e.g. DNA. To do so a two-layer approach is chosen [84; 58; 7]: Biotinylated thiols are simple to attach to a gold surface to form a SAM. This provides binding sites for streptavidin. There exists an optimal surface density of biotin molecules to establish the most suitable protein layer for the controlled adsorption of sensitive probe molecules. If too many biotin molecules are present at the surface the formation of a proper protein layer is sterically inhibited [83]. On the other hand, a low surface density of the SAM does not provide enough binding sites for the formation of a dense protein layer and therefore lessens the maximum number of binding pockets for further modification. It has been found [85; 58] that a mixing ratio of 10% of the biotinylated thiol biotinamino-capronacid-amidodioctyl-mercaptopropion-amid ($M_G = 575.8$ gmol^{-1}; see top of fig. 3.17) and 90% of the OH-terminated thinner thiol 2-mercaptopropionacid-[2-(2-hydroxyethoxy)]ethylamid ($M_G = 193.27$ gmol^{-1}; bottom molecule in fig. 3.17) leads to an optimum protein layer. One important result of the biotin-streptavidin matrix is that fluorescent labelled molecules are separated from the metal surface by at least

5 nm. Fluorescence surface plasmon spectroscopy can therefore be conducted with only
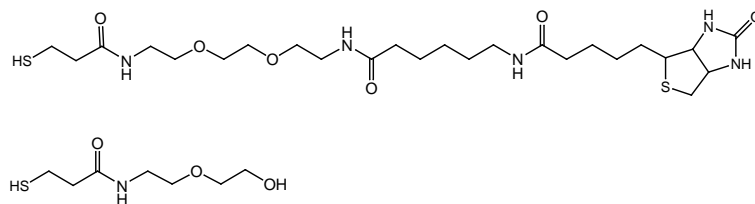
Figure 3.17: Structure formulas of the biotinylated (top) and OH-terminated (bottom) thiols that are used to bind streptavidin to the surface.

moderate losses of the fluorescence signal due to Förster quenching (compare section 2.3). Another consequence of this approach is that 53 % of the surface is covered by streptavidin molecules, corresponding to an area per protein of 44 nm^2. This leaves enough space for hybridisation experiments with a surface area of 3.1 nm^2 per double helix. Throughout this work the 10%/90% binary mixture is used as immobilisation matrix for the attachment of biotinylated DNA probes.

3.3.3.2 Deoxyribonucleic Acid

Deoxyribonucleic acid (DNA) serves as database for all genetic information of living organisms. The information is expressed in the way that DNA is transcribed into RNA (ribonucleic acid) and subsequently translated into amino acid sequences - proteins are synthesised. The DNA database, a biopolymer, is composed of units called nucleotides, which consists of a nitrogenous base, a pentose sugar, and a phosphate. The four nitrogenous bases are divided into the purines adenine (A) and guanine (G) and the pyrimidines cytosine (C) and thymine (T). As can be seen in figure 3.18 the nucleotide is built by a base that is bound to the C_1 atom of the deosyribose and a phosphate linked to the C_5 atom. The monomers are joined into linear polymers via the phosphate connecting to the C_3 atom of the next sugar. Therefore, one can distinguish between the 3' and the 5' end of a DNA strand. Single strand DNA (ssDNA) form double strands (dsDNA) by hybridisation, meaning that two ssDNA twist around each other in an anti-parallel direction. The so-called B-form of dsDNA with a distance between base pairs of 0.34 nm and a diameter of 2 nm is favoured. The resulting helix is partly held together by hydrogen bonding between opposite bases. The combinations (A, T) and (G, C) are are the only

stable combinations due to their similar dimensions (Watson-Crick base pair formation [86]). This hydrogen bonding however constitutes only one type of the weak forces that co-operatively stabilise the structure of the DNA, still allowing for conformational flexibility. Amongst the others are hydrophobic effects: The purines and pyrimidines are hydrophobic molecules that are buried inside the helix and thus protected from the aqueous environment. Therefore, the helix is stabilised for entropic reasons [87]. Stacking forces additionally encourage the hybridisation reaction. The flat neighbouring bases of the same strand are stacked on top of each other and the planar faces interact with each other in a complex manner by van der Waals and dipole-dipole interactions. A potential instability is introduced by the negative charges of the phosphate in the backbone. However, the charge repulsion is minimised by interactions with cations and positively charged proteins in solution. The non-covalent cooperative forces holding the DNA strands together can easily be disrupted. This process is known as denaturation. Complete denaturation is never found in vivo (Only partly denaturation occurs for DNA replication, transcription, or DNA repair purposes.) but can be triggered in vitro by altering the environment of the double-helix: Extreme pH, low ionic strength, or chaotropic agents influence the hydrogen
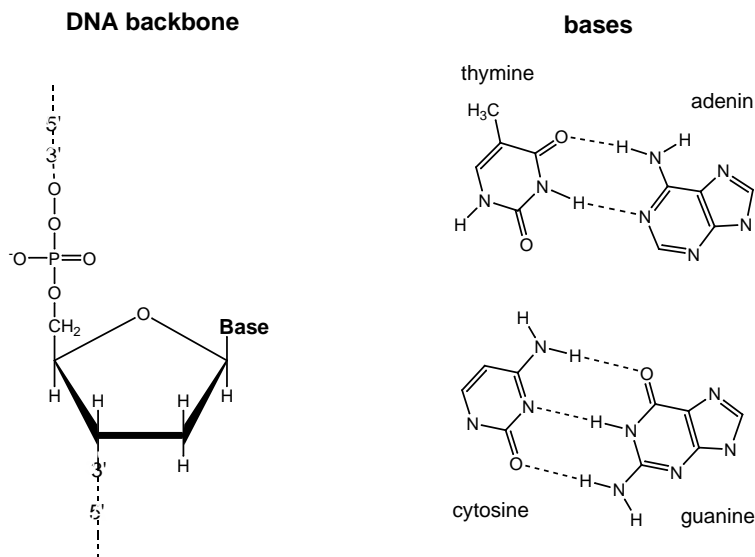
Figure 3.18: Nucleotide composed of a nitrogenous base, a pentose sugar, and a phosphate. The bases adenine, guanine, cytosine, thymine form pairs when two single stranded DNA sequences form a double helix.

bonds or the hydrophobic interactions and thus reduce the denaturation threshold. Tem-

perature is another factor that influences the stability and the process of denaturation is then called melting. At the melting temperature T_m 50% of all strands are separated into ssDNA. However, there is a difference between long and short DNA sequences: The long duplex separates to 50% whereas the oligonucleotide has far fewer weak forces to be disrupted, which causes, firstly, a decrease of T_m and, secondly, that half of all duplexes are separated into single strands at T_m. The melting further depends on the (G, C) content since there are three hydrogen bonds involved in the base pairing, the sequence of the nucleic acid as the stacking forces are not base-invariant, the presence of hydrogen bond disrupting agents like formamide or urea, and the number of base pair mismatches. The strictness of the (A, T)-, (G, C)-base pairing leads to a regular helix due to the similarity of the sizes. Mismatches with less stable hydrogen bonds and stacking forces reduce the double-strand stability. Their effects are more pronounced in short chain lengths and as a rule of thumb, 1% mismatch causes a decrease of T_m of about 1 °C for chains with less than 100 base pairs [58]. In vivo those mismatches are usually repaired.

type	bases	sequence
probe	30	5′-biotin-T_{15} TGT ACA TCA CAA CTA-3′
target (0MM)	15	5′-Cy5-TAG TTG TGA TGT ACA-3′
target (1MM)	15	5′-Cy5-TAG TTG TGA CGT ACA-3′

Table 3.2: Sequences of unlabelled probe and Cy5-labelled target oligonucleotides. Differences in the base sequences from perfect match are underlined.

This study is focused on the detection of the hybridisation reaction of oligonucleotides at a surface. Here, the target sequence can bind specifically to a region of the probe that is attached to a streptavidin layer through a biotin link. From a statistical point of view the minimum size of a probe that is unique is 20 [58]. The length of the probes also influences the hybridisation kinetic as short probes react faster. The hybridisation process itself can be split into two processes: The usually rate-limiting nucleation comprises the subsequent collision and dissociation of two single strands until the bases of complementary strands are in correct register. The formation of the dsDNA then follows quickly when both single strands are zippering up. Other properties that are rate determining are the formation

of secondary structures and self-complementary regions of the probe and target. Yet, structured probes have been found to show enhanced hybridisation specificity [58].

Table 3.2 summarises the oligonucleotide sequences used in this work. The 15 base thymine spacer next to the biotin linker of the probe serves to reduce steric hindrances during the hybridisation, being in the same time short enough to avoid crowding effects. The second 15 residues constitute the recognition sequence with the complementary sequence being found in the 0 mismatch (0MM) probe. A probe with 1 mismatch (1MM), the mismatch position of which is marked in the sequence, can be found in table 3.2 as well. Both probes are fluorescent labelled at the 5' end (Cy5-molecule). All sequences used feature hairpin formation and self-annealing of complementary regions [58].

3.3.3.3 Immobilisation Procedure

The preparation procedure of the multilayer architecture is done in the following steps: After the evaporation of gold the sample is transferred into a $5 \cdot 10^{-4}$ M solution of the 10%/90% binary mixture of thiols. There it is left for at least 30 min. The thiols (*Boeringer Mannheim*) were previously dissolved and mixed in phosphate buffer saline (PBS; 0.01 M phosphate buffer, 0.0027 M KCl, 0.15 M NaCl, pH 7.4; *Aldrich*). After rinsing with PBS the streptavidin layer is formed via specific binding from a $5 \cdot 10^{-6}$ M solution (in PBS) for at least 45 min. The 5'-biotinylated DNA probe (1 μM in PBS) is then bound to the straptavidin layer. These three preparation steps are well established and reliable [85; 58]. Usually they are performed outside the measurement cell and the sample is subsequently built into it. SPR is only used to register the final formation of the layers. After a first background scan a kinetic measurement is started and the target DNA (1ml, 0.5 μM) injected into the cell by means of a little T-connector in-between the tubing to the pump and the cell. The T-connector and the cell are then closed and the system is ready to be pressurised. To allow for the hybridisation, the cell is left unchanged and only after an equilibrium is reached the pump is switched on to increase the pressure to 10 MPa. The amount of injected target is calculated to be sufficient to guarantee no dilution due to the buffer in the pressurising equipment during pressure cycles.

3.3.4   Supercritical Carbon Dioxide

3.3.4.1   Introduction

A fluid is called supercritical when both, its temperature and pressure lie above its critical values (T_c, p_c). In this regime temperature and pressure control dielectric constant and solvability capacity. The supercritical fluid combines properties of fluids with those of gases in one and the same phase [88; 89]. Due to its compressibility densities comparable to fluids can be reached, which allows for solvation of many compounds while the viscosity and the diffusion properties remain those of gases resulting in important implications for reaction kinetics [90; 91].

Thanks to its characteristic chemical and physical properties (cf. table 3.3) CO_2 is a very convenient system. It has a critical temperature near room temperature, a modest critical pressure and a higher density than most supercritical fluids [92]. From a chemical viewpoint it is environmentally benign, non-inflammable being an end-product of a complete combustion, non-toxic and cheap. This makes it an excellent medium in the medical or food industry, e.g. to extract caffeine from coffee or tee [2]. The cheapness arises from the fact that it exists in many very pure natural resources and, additionally, that it is a by-product of ammonia, hydrogen, and ethanol production and electrical power stations.

$T_c[°C]$	$p_c[MPa]$	$\rho_c[(g/cm)^3]$	$\alpha[\ m^3]$	$\mu[D]$	$Q[(erg \cdot cm)^{1/2}]$
31.0	7.38	0.468	$2.76 \cdot 10^{20}$	0.0	$-4.3 \cdot 10^{26}$

Table 3.3: Physical properties of carbon dioxide.

The solubility plays a crucial role in many applications, one of them being polymerisation. While CO_2 is a good solvent for many unpolar and some polar molecules of low molecular weight [93; 94], polymers of high molar masses only solve poorly at mild conditions (< 100 °C, < 35 MPa) [92]. The only polymers that exhibit good solvability under mild conditions are amorphous fluoropolymers and silicones [88; 95; 96]. CO_2 has a low dielectric constant and no permanent dipole moment but its large quatrupole moment provides a substantial contribution to its solubility capability. Plenty of methods try to enhance the solubility properties of carbon dioxide, one of them is the addition of co-solvents, volatile substances like alcohols, ketons, or fluorocarbons. The solvability

characteristics of CO_2 also dictate the polymerisation type employed in polymer synthesis. Only few monomers can be polymerised homogeneously in supercritical CO_2; usually these are fluoropolymers [97; 91]. On the contrary, many polymerisation reactions are heterogeneous in nature, either as precipitation, dispersion, or emulsion processes due to the inherent insolubility of most polymers in CO_2. In consequence, the field of surfactant research is very vivid because they control the polymer properties and morphology [98; 99; 91]. When the pressure is lowered after the polymerisation process one gets fine powder and no drying of the product is needed - an important step towards reducing production costs.

Based on the properties described above many different applications arise: The fractionation of polymers is one important area affected by the polymer solubility in $scCO_2$. The controlled reduction of the density of a polymer solution, for instance, allows the precipitation of the highest molecular weight polymer fraction first [88; 96]. Another feature of $scCO_2$ is the promotion of plastification of polymers for example in polymerisation processes [8; 100], which results in a lowering of the glass transition temperature of the polymer as well [101; 9; 102].

3.3.4.2 Swelling of PMMA in MMA/scCO2

The sample preparation comprises (besides the gold evaporation) the following steps: Polymethylmethacrylate (PMMA) of a molar mass $M_W = 350.000$g/mol (*Polyscience*) is dissolved in toluene (99%, *Fisher*) at a concentration of 12.5 wt.%. The solution is subsequently degassed under vacuum and polymer films are prepared by spin-casting onto the gold layer at 8000 rpm for 60 s. In order to remove any residual solvent in the polymer and to minimize anisotropy effects induced by the spin-coating process the samples are then annealed at 120 °C in vacuum for 12 h. The extent of completion of the drying process is checked by measuring the refractive index of the PMMA film in air prior to all measurements. The inhibitor in the methylmethacrylate (MMA; *Röhm AG*) is removed by washing with 10 wt.% aqueous NaOH and, thereafter, with water. After careful drying, the monomer is distilled at reduced pressure. 0.2 wt.% hydroquinonemonomethylether added to the MMA prevents polymerisation during the measurements. Carbon dioxide (99.995 wt.%, *Linde AG*) is used without further purification.

As depicted in figure 3.7, a different approach to generate the pressure is used in the mea-

surements of the interaction of a polymethylmethacrylate (PMMA) film with a solution of its monomer (MMA) and supercritical carbon dioxide. A high-pressure mixing circuit comprises, besides the cell, an HPLC pump as pressure generator, a gear pump to mix the solvent homogeneously, and several valves to disconnect the pressure cell from the circuit. The tubes to and from the cell are heated in order to avoid temperature sinks while mixing. The cell itself is kept at a constant temperature of 60 °C using a thermostat (not shown).

The measurement execution comprises the following steps [103]: After the assembly of the pressure cell, the refractive index and the thickness of the PMMA film is measured as reference against air. Before the measurement protocol with the MMA/CO_2 mixture is started, the cell is tested for leaks in pure CO_2. In order to avoid damage of the polymer film in the cell due to the fact that MMA dissolves PMMA, a known amount of MMA is injected into the gear pump that is decoupled from the cell (valve V_2 closed, cf. fig. 3.7). Then, the mixing circuit is filled with CO_2, heated up to 60 °C, and the MMA/CO_2 solution is thoroughly stirred. Subsequent careful pumping of the solution through the whole circuit (V_2 opened) for several minutes results in a homogeneous mixture in the cell. After closing the valves V_2 and V_3 the mixture is left to equilibrate for 20 minutes in the cell before the actual measurement is started. Higher pressures than the starting one are obtained by adding CO_2 to the circuit and then resuming the complete mixing procedure.

3.3.5 Cyclic Voltammetry

All materials employed are of research grade and are used as received from commercial sources without any additional purification.

In the case of the experiments of the potassium hexacyanoferrate(III)-(II) system a solution of 0.1 M KCl, 2 mM $K_3Fe(CN)_6$, and 2 mM $K_4Fe(CN)_6$ in Milli-Q water are mixed. The second set of measurements concerning the polymerisation of thiophene are performed using a solution of 0.1 M thiophene monomer and 0.1 M $LiClO_4$ in acetonitrile.

As reference electrode the Ag/AgCl system is chosen for the measurement of the $K_3Fe(CN)_6/$ $K_4Fe(CN)_6$ system. To do so silverchloride is electrochemically deposited onto a blank silver wire in a 0.5 M HCl solution. However, since Ag/AgCl reference elec-

trodes have proven not to be reliable in an acetonitrile environment, a blank silver wire is used as reference electrode in the case of the thiophene/acetonitrile solution [104].

Prior to each measurement the solutions are purged with dry nitrogen to remove any residual oxygen. The high-pressure cell is cleaned with a 1% Hellmanex solution in an ultrasonic bath for at least 20 min followed by thorough rinsing with Milli-Q water and subsequent sonicating in pure Milli-Q water for another 10 min. The immersion of the platinum counter electrode in piranha solution after each measurement ensures removal of any organic contaminants. The silver wire reference electrode is cleaned with ethanol.

4. Sol-Gel Silica Films

The technique surface plasmon resonance spectroscopy is based upon the utilisation of a noble metal to generate the surface plasmon electromagnetic field. This field is then used to probe changes of the optical (film) properties, e.g. due to binding reactions, occurring within the vicinity of the surface. Thiol-based self-assembly techniques [105; 106] work well with noble metals and in most cases are sufficient to generate supramolecular architectures, which can be functionalised for e.g. potential biosensing applications [107; 108]. However, in certain cases, such an immobilisation strategy is not suitable and as a result requires the use of other complex coupling chemistries.

Supramolecular architectures of biomolecules based on silane coupling chemistries [109] on silicon dioxide substrates are commonly used in many applications like in genomic research where these substrates are employed to immobilise nucleic acids [110; 111]. Another example for the use of these substrates is in immobilising polymer brushes [112], which serve as a three-dimensional matrix for studying host-guest interactions, and also in fundamental studies of polyelectrolytes [113]. One way to combine the use of surface plasmon spectroscopy for monitoring surface reactions and silicon dioxide substrates for the coupling chemistry of one of the reactants is to thermally evaporate a thin layer of SiO_2 in a vacuum chamber onto the metal layer used for surface plasmon excitation. However, in most cases the interface SiO_2/aqueous medium is not stable and usually the thin layer of SiO_2 comes off the surface within a few minutes and, as a result, is not suitable for time-consuming applications.

Here, the use of sol-gel chemistry in generating stable silicon oxide films on noble metals that can then be easily functionalised for sensing purposes is reported. The consecutive steps of the assembly are scrutinised first. The stability of these films is tested by using a stringent aqueous solution containing PBS buffer, which is commonly used in many biological studies. To display the versatility of these films, they are applied in investigations

of N-isopropylacrylamide hydro-gels.

4.1 Characterization of Sol-Gel Silica Films

4.1.1 Assembly of Silica Films

The assembly of a sol-gel silica film on top of a noble metal comprises mainly three steps as indicated in figure 3.14: At first, a 3MPT monolayer is self-assembled onto the surface. Then, this layer is hydrolysed and condensed before a sol is spin-cast to form the top silica layer. After drying, the sample is ready for further modification with e.g. silane chemistry. In the following, the properties of the different assembly phases are characterised one after another.
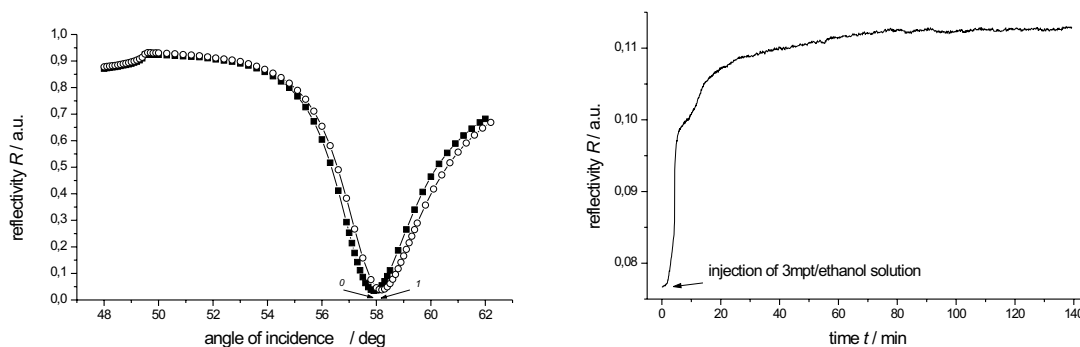
Figure 4.1: SPR scans (left) of the silver surface before (squares) and after (open circles) the self-assembly of 3MPT. The time dependent adsorption of the thiol onto the surface is shown on the right-hand side.

Onto a newly evaporated metal film (usually gold or silver) a layer of 3MPT is self-assembled. The right hand side of figure 4.1 illustrates this adsorption process by means of a SPS kinetic curve as introduced in section 3.1.1.1.2. After a steep rise in the first 20 min the curve levels off and an equilibrium value is reached after about 60 min. The corresponding scan curves are shown in the same figure on the left-hand side. The solid one of the two curves represents the surface plasmon resonance without the SAM, the other one with it. Clearly, a shift of the minimum due to the adsorption of 3MPT can be observed. Its evaluation by means of the Fresnel equations and with a refractive index of

the thiol layer of $n_{thiol} = 1.45$ reveals a thickness of 2.8 nm. This value is substantially larger than what is expected from reported bond lengths and angles [71]. There are two explanations for this increased thickness: Firstly, the 3MPT molecules are very reactive and tend to form dimers and higher orders at the presence of oxygen. This is the reason why the chemical is always vacuum distilled prior to use, solved in dry ethanol for self-assembly, and stored in a dessicator. The self-assembly itself is conducted in an oxygen-free argon environment. However, for the experiment of figure 4.1 the 3MPT solution has to be injected into the fluid cell at ambient conditions. Thus, dimers can easily form in the solution and adsorb to the surface as such. Secondly, the baseline in the kinetic (right side of fig. 4.1) is not absolutely stable. The pure ethanol that is used for the recording of the reference scan of plain gold seems to interact with the gold surface prior to the injection of the thiol solution. Consequently, the reference scan of the gold may not correspond to the actual reference as seen at the exact point of 3MPT injection.
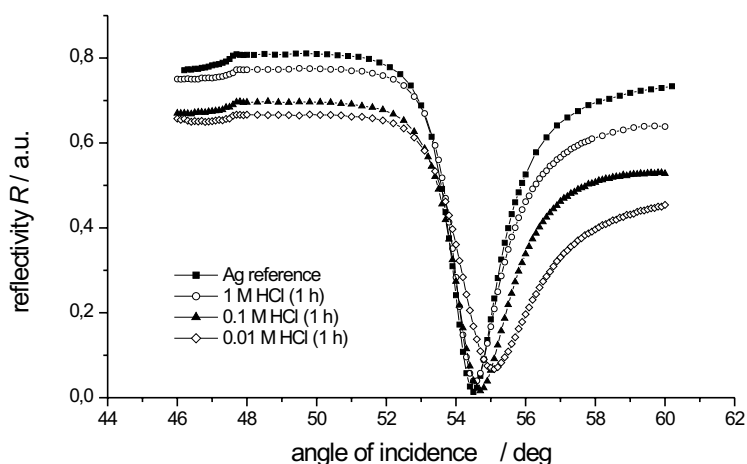
Figure 4.2: Reflectivity vs. angle of incidence for 3MPT layers on silver after immersion in HCl solutions of different molarity (0.01 M, 0.1 M, 1 M) for 1 h.

The second step in the silica film preparation procedure is the hydrolysis and condensation of the methoxy head-groups of the 3MPT molecules. Prior to hydrolysis 3MPT forms an organised monolayer and the head-groups are largely oriented parallel to the surface [114; 71]. After the hydrolysis and condensation reactions the molecules reorient on the

surface producing a Si-O-Si network containing some unreacted Si-OH defects. XPS studies [114; 71] showed that less than 5 % of the original Si-O sites remain as silanoles in the 3MPT monolayer. In terms of finding the optimal reaction parameters for SPR studies this method is again used to monitor the hydrolysis and condensation reactions at the surface. Since it is reported that these reactions highly depend on the pH of the solution [73] the molarity of the HCl solution that is used to stimulate hydrolysis is varied first. All samples are immersed in HCl for one hour. As can be seen in fig. 4.2 the kinetics of the reaction is such that for the 0.01 M solution the hydrolysis is not completed yet - the scan curve is very broad, the minimum at comparatively high angles and the reflectivity low. One can thus imagine a thiol surface that is still underway to fully convert to a dense, cross-linked monolayer. On the other hand, the angular scan of the sample treated with 1 M HCl has high reflectivity and is almost as sharp as the silver reference scan. Here it seems that the Si-O-Si network is completely established and the surface is rather smooth and homogeneous.
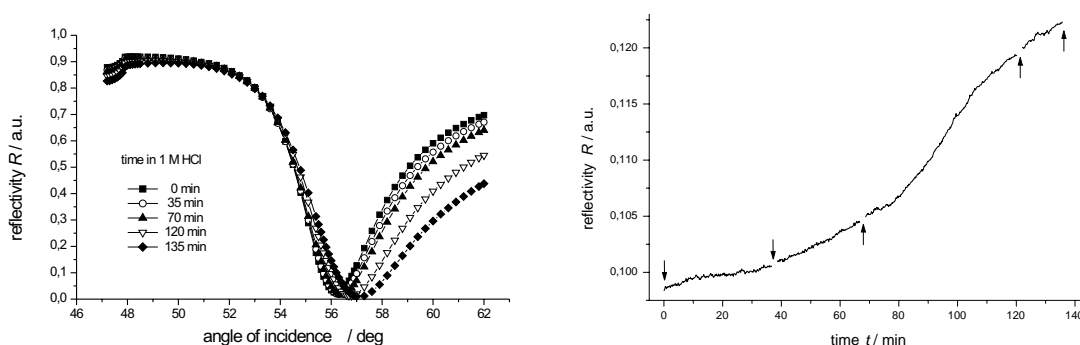
Figure 4.3: Immersed in a 1 M HCl solution the hydrolysis of the sample of
fig. 4.1 is studied as a function of time. The arrows indicate the points
when the scans, shown on the left hand side, are taken.

The second variation parameter is time. The same sample that is presented in fig. 4.1 is now exposed to 1 M HCl since the reaction in 1 M HCl seems to be the best concentration for a fast and complete sample preparation procedure (cf. 4.2). The left of figure 4.3 depicts the reflectivity scans taken at certain time intervals as indicated in the right panel of the same figure, which shows the corresponding behaviour of the reflectivity with time. In total, a reaction time of over 2 hours is covered. Corresponding to the results of the

variation of the concentration of HCl in the solution, here the reflectivity scan curves start from a broad shape and turn to be just as sharp as the reference scan. This behaviour can be followed in the kinetic SPR mode. As the plasmon resonance shifts to lower angles and its shape gets sharper, the reflectivity, recorded at a fixed angle ($\theta_{fixed} < \theta_0$), accordingly rises. After a time period of approximately 2 hours the curve starts to level off indicating that the surface reactions begin to slow down with only few sites left in the monolayer that are not yet cross-linked.
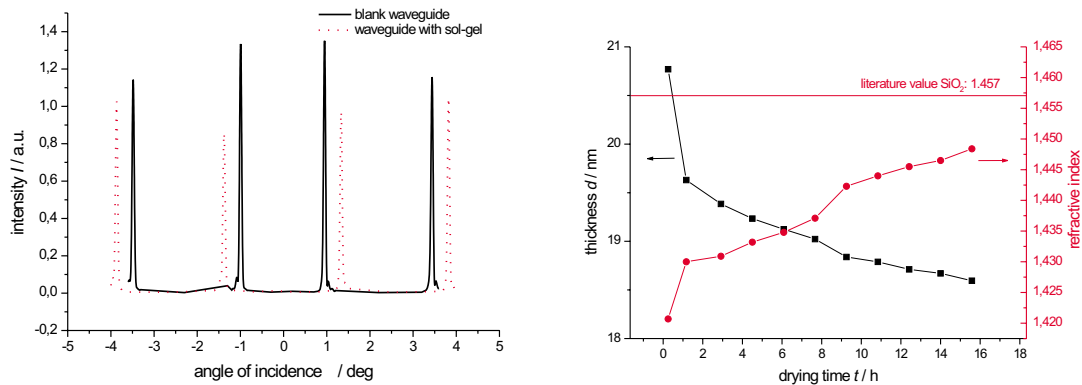
Figure 4.4: Waveguide scans of a ASI2000 chip with and without a spin-cast sol-gel layer (left). The evaluation of those scans taken in 1.5 hour intervals reveals the drying characteristic of the sol-gel under ambient conditions (right).

The final step of the silica film preparation is the spin-casting and subsequent drying of the sol-gel film. Different H_2O/TMOS ratios in the precursor sol account for the ability to vary the thickness of the applied silica film (cf. section 3.3.1). Since TMOS forms metastable, nanoscopic polymers between a pH of 1 and 5 the extend of solution polymerisation prior to deposition is controlled by dilution [69]. The very high dilutions used here result in extremely dense and perfect silica films once the gelation is completed and the remaining water has been removed [69]. The drying is achieved by just leaving the samples in the dry atmosphere of a dessicator for 24 hours. Figure 4.4 illustrates the drying procedure by means of waveguide mode spectroscopy. A 15 nm sol precursor is spin-cast onto a waveguide whose surface was chemically activated (1:1 methanol/HCl followed by a bath in concentrated H_2SO_4 [115]). The intensity of the waveguide modes

is recorded in approximately 1.5 hours intervals for a total of 16 hours (cf. fig. 4.4, left). The right part of figure 4.4 shows the evaluation of these scans giving the thickness of the sol-gel layer and simultaneously its refractive index. The thickness decreases over the whole time period by 11 % where half of it occurs within the first two hours indicating that most of the remaining solvent evaporates fast and the sol-gel condenses. The refractive index shows a similar dependence: With time it increases (the solvent evaporates and the film condenses) and seems to approach the literature value of $n(\mathrm{SiO_2}) = 1.457$ [73] in the long time limit.
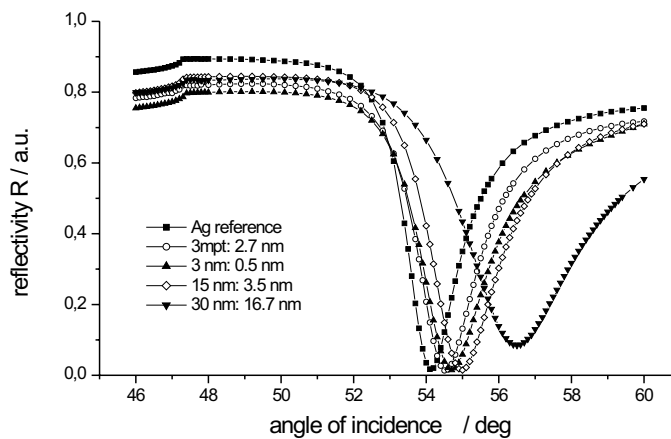
Figure 4.5: SPR reflectivity scans of sol-gel films with different $\mathrm{H_2O}$/TMOS ratios.

The final silica film can then be analysed for its thickness and suitability for SPR applications. Figure 4.5 compares different $\mathrm{H_2O}$/TMOS ratios of the precursor solution with respect to the final thickness on a substrate. The values are given in table 3.1. With increasing TMOS moiety the thickness of the layer increases as expected. However, very thick silica layers tend not to be as optically homogeneous as their counterparts at higher $\mathrm{H_2O}$/TMOS ratios. Their scan curve is broader than all the other curves, an observation, which can be explained by the formation of bigger polymer particles in the precursor sol prior to spin-casting.

X-ray reflectometry (XRR) is a measurement technique that reveals details about layer architecture and surface properties of thin films. Here it is applied to give some information about the surface roughness of the silica films. Apart from that, it produces data of

the layer thickness, which can then be compared to the method of surface plasmon reso-
nance spectroscopy. However, since gold scatters x-rays very well it has some glossing-over
effect. The response of the silica layer blurs and the data one is interested in cannot be
obtained anymore. For this reason the sol is spin-coated directly onto a chemically acti-
vated (see above) glass sample. Figure 4.6 shows the data that is evaluated to give the
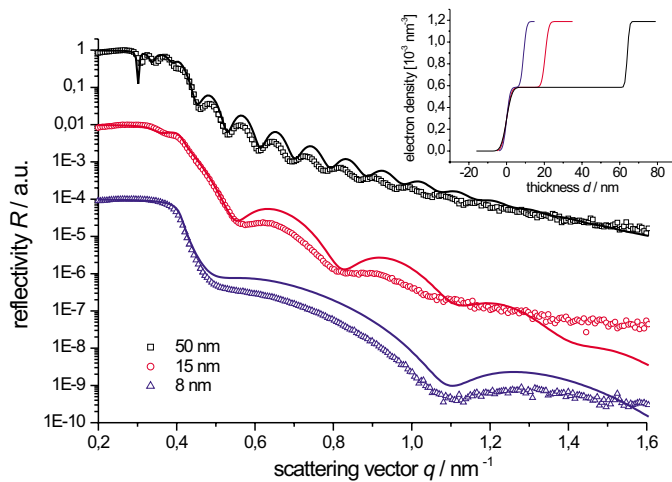
Figure 4.6: X-ray reflectometry scans of sol-gel films of different thickness.

results summarised in table 4.1. The theoretical fits upon which the surface property
values are retrieved from the data are by far not perfect. However, they are based on a
layer profile as simple as possible - a box profile (cf. inset of fig. 4.6).

sample d(ELL)	thickness nm	ρ(e$^-$, substrate) Å^{-3}	rms$_{substrate}$ Å	ρ(e$^-$, sol-gel) Å^{-3}	rms$_{sol-gel}$ Å
blank		1.22 ± 0.05	7 ± 1		
50 nm	640 ± 5	1.22 ± 0.05	9 ± 1	0.58 ± 0.02	23
15 nm	205 ± 3	1.22 ± 0.05	15 ± 1	0.58 ± 0.05	20
8 nm	90 ± 3	1.22 ± 0.05	13 ± 1	0.58 ± 0.1	15

Table 4.1: Comparison of the surface parameters obtained by x-ray reflectometry.

Nevertheless, since the parameters for the electron densities are valid for all samples

one can justify the comparison of the different samples on the basis of such a simple model. First of all, the roughness of all modified surfaces is greater than the one of the blank sample. Secondly, the roughness increases with decreasing H_2O/TMOS ratio. This finding is reasonable when considering that with increasing TMOS concentration the TMOS particles in the precursor sol get bigger and the resulting condensed silica film resembles these intrinsic structures. The thickness of the sol-gel layer is the second parameter that can be extracted from XRR measurements. The comparison to the values obtained by SPR show systematic deviations. In the case of surface plasmon spectroscopy the silica layers of the same TMOS concentration are thinner than the corresponding values measured by x-ray reflectometry. The reason is the preparation procedure. The SPR precursor sol is spin-cast onto a cross-linked 3MPT layer with approximately 5 % surface coverage of silanoles.
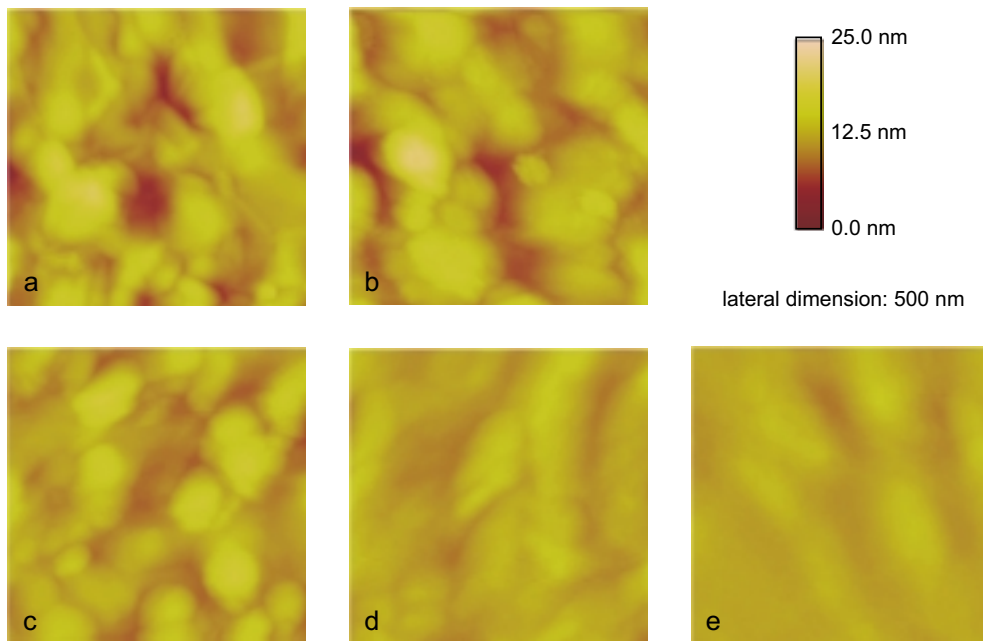
Figure 4.7: AFM pictures of (a) plain, annealed gold, (b) hydrolysed 3MPT on gold, (c) 3 nm (d) 15 nm and (e) 30 nm of silica on top of a cross-linked 3MPT layer. The lateral scale is 500 nm in every case.

On the contrary, the samples used for XRR are prepared on activated glass slides exposing a high number of silonole groups on the surface. Thus, the precursor finds a higher number of binding sites on glass slides than on a 3MPT covered surface resulting in a higher thickness of the overall silica film. This explanation is supported by the measurement

presented in figure 4.4. The samples prepared for the characterisation of the drying process by means of waveguide spectroscopy also simply consist of spin-coated precursor sol onto activated glass slides. The resulting silica layer thickness of 18.5 nm corresponds very well with the (20.5 ± 3) nm found by x-ray reflectometry.

Another surface characterisation method is atomic force microscopy. Figure 4.7 compares the different steps of the silica-layer assembly in terms of topology. The annealed gold surface prepared on a typical quartz glass substrate still reveals distinct gold particles. The self-assembly and hydrolysis of the 3MPT layer does not change this surface pattern much (cf. figures 4.7 a and b). The same observation is reported for scanning electron microscopy pictures of 3MPT on silver [72]. The results of the application of the silica film results a covering of the exposed surface as can be seen in figures 4.7 c, d, and e for 3 nm, 15 nm, and 30 nm thick silica films, respectively. The pictures indicate that the films conform to the roughness of the underlying gold surfaces and appear to be even and fairly dense. With increasing thickness the distinct marking of the underlying gold vanishes and a rather uniform surface is presented.

4.1.2 Stability in Buffer Solutions

Vapor deposited silicon oxide (SiO_x) films on noble metals are plagued by stability problems when tested in PBS buffer solution. PBS, however, is one of the most commonly used buffers in biomolecular interaction studies and serves as a useful test reference for the stability of the SiO_x films on noble metals. One of the inherent problems of this system is the interface between the noble metal and the SiO_x layer which is quite unstable and can be easily eroded by the presence of solvent molecules that are in contact with the SiO_x surface. The reactivity of the noble metal also has an important part to play in the overall stability of these layers. Thin films of gold are normally quite stable (cf fig. 4.8a) and resist oxidation in aqueous environments, unlike those made from silver which are easily oxidized under the influence of salt present in the buffer solution (fig. 4.8g). Although thin films made on gold are typically sufficiently stable for bio-molecular interaction studies, the robustness of deposited silicon dioxide films on Ag substrates is also tested. Since silver shows a very narrow surface plasmon resonance and also generates a high field enhancement, stable films of SiO_x obtained on that substrate will be very useful

for many fluorescence studies and sensoric applications.

SPR kinetic plots of silver and evaporated SiO_x films on silver and gold are shown in Figures 4.8g, f and d, respectively. The decrease in reflectivity with time indicates that the SiO_x film is eroding off the interface, which is a qualitative measure of the instability of the interface. This instability limits the usefulness of these substrates for various SiO_x coupling schemes.
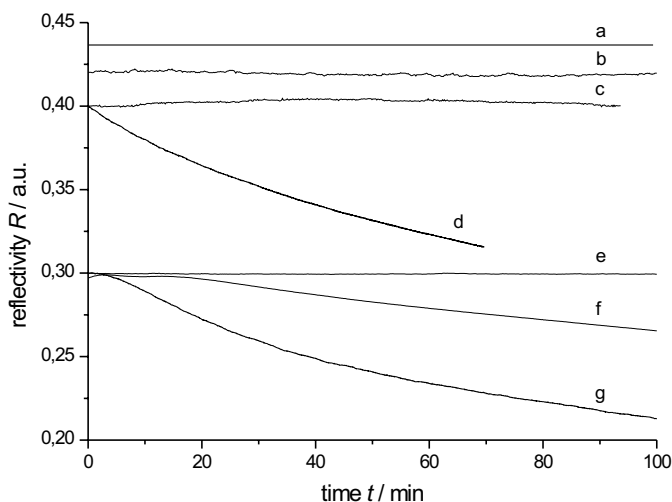
Figure 4.8: Stability analysis of sol gel films in PBS buffer. Shown are the reflectivities measured at a fixed angle of observation for (a) bare gold, (b) 15nm sol gel film on gold, (c) 30nm sol gel film on gold, (d) thermally evaporated 15nm SiO_x film on gold, (e) 30nm sol gel film on silver, (f) thermally evaporated 15nm SiO_x film on silver, and (g) bare silver.

The presented scheme to chemically synthesize silicon dioxide films circumvents this problem. Sol-gel processing allows for exquisite control of the micro and nano structure and thickness of these ultrathin coatings. The sol-gel preparations used here utilise extreme dilution of the Si-containing reactants to ensure complete hydrolysis of the starting alkoxide and to inhibit solution condensation reactions of hydrolysed monomers and oligomers. Thus, the sizes of the resulting sol particles are limited leading to a high packing density, the exclusion of most solvent (H_2O/ethanol) in the final film, and hence a very low porosity. The thickness of the SiO_2 can be varied by spin coating TMOS on to the hydrolyzed 3MPT monolayer at different speeds and concentrations. The stability of the 15 nm and

30 nm (ELL) silica films on gold (cf fig. 4.8b and c) and 30 nm film on silver (cf fig 4.8e) is quite remarkable. This behaviour is attributed mainly to two reasons: First, the SiO_2 film is effectively anchored onto the noble metal by forming covalent bonds between some of the Si atoms of the SiO_2 film and the Si atoms of the 3MPT molecule, which in turn is strongly coordinated via its S-terminal to the noble metal surface. Second, the sol-gel film, which forms a protective layer and thereby prevents the buffer from undermining the coating, is uniformly distributed. All the above stability experiments are performed at 20 °C and at atmospheric pressure. Next, the stability at high temperature and pressure conditions is illustrated.

4.1.3   Stability at Elevated Pressures

In addition to presenting a platform to which further functional layers can be assembled utilising different processing steps, the sol gel films also have to withstand severe thermal and chemical conditions [70] in some cases. Here, the focus is set on the variation of
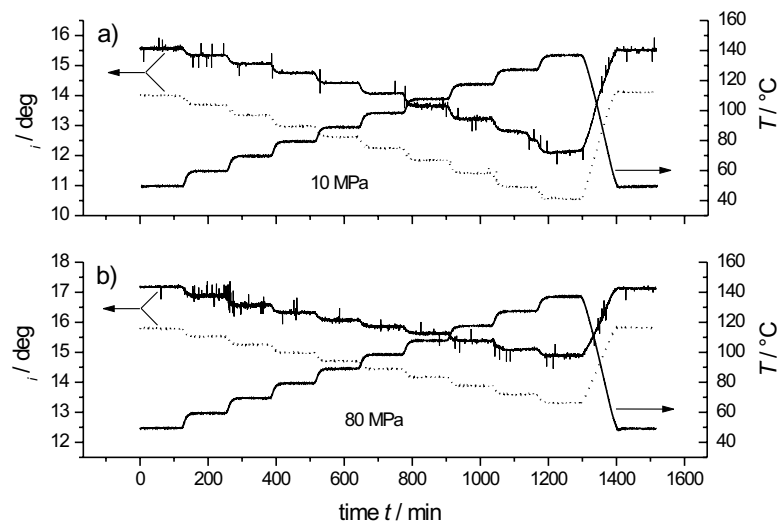
Figure 4.9: Comparison of the minimum resonance angle of gold (dashed) and gold containing a sol-gel film on top (solid) monitored as a function of time. While recording the minimum angle the temperature is increased in 10 °C-steps from 50 °C to 140 °C and decreased continuously back to 50 °C again. The data of part a) is measured at 10 MPa while part b) is recorded at 80 MPa.

the temperature and pressure to investigate the stability of the sol-gel films. The measurements are carried out using the grating high-pressure cell with the pressure medium being a mixture of acetone and ethanol (47.7%/52.3%). Figure 4.9 summarises the results obtained at 10MPa and 80MPa. The minimum resonance angle is monitored as a function of time while the temperature is simultaneously increased step-wise from 50 °C to 140 °C in 10 °C-steps and at each temperature is kept constant for 2 hours. At the end of the measurement cycle, the starting temperature is adjusted again in order to verify whether the high temperatures have damaged the film. As can be seen, the resonance minimum stays constant at the different temperatures over the two hour period which implies that also the optical thickness of the layer is constant and that the film is stable. Also, after the entire temperature cycle is completed by cooling down again to room temperature, the minimum angle matches the one measured at the beginning of the cycle, which is another evidence of the stability of the layer. The decreasing resonance angle with increasing temperature can be quantitatively attributed to the change of refractive index of the pressure medium with the optical thickness of the sol-gel layer staying virtually constant. This is also seen by comparing the curves of plain gold with those having a sol-gel film on top of them. When increasing the pressure, the shape of the curves remains the same whereas the respective resonance minima are shifted to somewhat larger angles. It appears that pressure has effectively no influence on the stability of sol gel films.

4.2 N-isopropylacrylamide Gels on Sol-Gel Films

Gels are materials that have both, liquid- and solid-like properties [116]. The liquid-like properties stem from the fact that its major constituent is usually a liquid, e.g. water. On the other hand, gels maintain their shape due to crosslinks of the polymers in the form of a network. This aspect highlights the solid-like nature of gels. Furthermore, gels can change their state drastically from a solvent swollen to a collapsed state and vice versa. The volume phase transition of hydrogels has been shown to respond to a variety of stimuli such as pH [5], temperature [6], magnetic fields [1], and electric fields [6] and has been proposed for use in a wide range of applications, particularly within the biological sciences. These include drug delivery systems [117], artificial muscles [1], membrane separations [118], and surfaces in biomaterials [119]. The phase transition is triggered by an infinitesimal change

of an environmental extensive variable, e.g. temperature, which results in an tremendous change of extensive properties of the gel, such as the volume. Thermoresponsive polymer gels like NIPAAm hydro-gels are known to have a volume phase transition, analogous to the lower critical solution temperature (LCST) of the corresponding linear polymer. The volume phase transition can be modelled using Flory-Tanaka theory as a balance between mixing free energy, rubber elasticity free energy, and osmotic pressure due to counter-ions of ionisable co-monomers [116]. However, this understanding of bulk gels does not necessarily extend to the many applications of thermoresponsive polymer gels. When used in actual devices the volume phase transition is inevitably constrained in some way and no longer corresponds to simple theoretical predictions.

The LCST transition results from a delicate balance of hydrophobic and hydrophilic groups within the polymer [120]. The collapse of NIPAAm gels can be attributed to hydrophobic interactions inside the gel, resembling the aggregation of NIPAAm in aqueous solutions as found by cloud point measurements [1]. Hydrogen bonding is central to the understanding of the volume phase transition in hydrogels and the addition of salts or urea can significantly alter the transition by acting as structure breakers. Through the addition of ionisable co-monomers, such as sodium acrylate (SA), the total volume change can be increased to as much as 100-fold along with an elevated transition temperature [116]. In addition to the effect on the volume change, the concentration of sodium acrylate also influences the continuity properties of the transition itself. Applying hydrostatic pressure to bulk gel has similar effects on the gel in that the hydrogen-bonding environment is disrupted. As a result, the transition temperature increases and the discontinuous transition becomes continuous with a broader transition as the pressure is increased [1; 121; 122].

In work by Suzuki and coworkers [123], the volume phase transition has been limited to two dimensions by fixing the ends of cylindrical NIPAAm gels. As a result of this constraint, neutral NIPAAm gel has a larger total volume change and higher volume phase transition temperature. This behaviour can also be modelled theoretically through a two-dimensional analogue of existing theory and modifications that allow for the resulting non-Gaussian chain conformations. Studies of linear polymers in thin films at interfaces have shown that the resulting confinement can alter characteristic transitions that exist in the bulk materials. Examples include the glass transition temperature [3], the LCST of linear substituted acrylamides [124], and nematic transitions in polymers with liquid

crystalline side chains [125]. Although the LCST transition of linear polymers has been observed at an interface, the more common crosslinked hydrogels have only been observed on a more macroscopic scale [126]. If a crosslinked gel is chemisorbed to the substrate, it will be unable to expand and contract laterally, effectively confining the transition to one dimension perpendicular to the substrate. The aim of this study will be to examine how this type of confinement affects the transition temperature of both neutral and ionized NIPAAm gels and how the additional influence of pressure, a complementary variable, influences the volume phase transition.
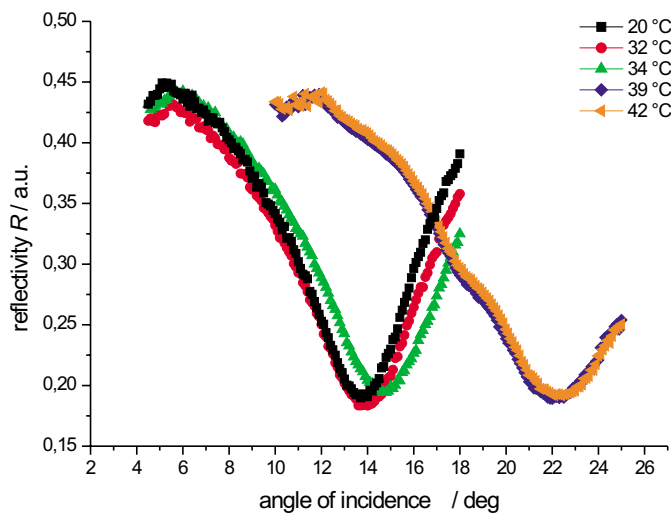
Figure 4.10: SPR reflectivity scans of a 0 mM SA, 700 mM NIPAAm, 8.6 mM BIS hydrogel film.

Kleideiter at al. [56] showed that the optical characteristics of gold surfaces remain unchanged under pressure, which constitutes the basis for all of the measurements presented in this work. Furthermore, in section 4.1.3 the pressure dependence of the sol-gel layer is presented. There, evidence of the stability of this mediator layer onto which the NIPAAm hydrogel is chemically fixed is given. In the case of the gels in this study, the angular scans of the gel layer, an example of which is given in figure 4.10 for a 0 mM SA, 8.6 mM BIS, 700 mM NIPAAm sample , are fit to Fresnel calculations to determine the refractive index n of the gel. In the graph, two scans are shown below (20 °C and 32 °C) and above (39 °C and 42 °C) the transition temperature. The last curve at

34 °C represents the gel at a point just below the transition temperature of 34.3 °C above which it collapses. At low temperatures the scan curve is comparatively sharp and the edge of total reflection indicates (along with the minimum position) the refractive index of the polymer/water mixture that varies with temperature. As the temperature is increased to near the transition temperature the entire curve shifts to higher angles due to a higher total refractive index of the gel in the process of the diffusion of solvent from the gel. The result of this completed process can quite clearly be seen in the curves at 39 °C and 42 °C. Here the whole scans are shifted to higher angles of
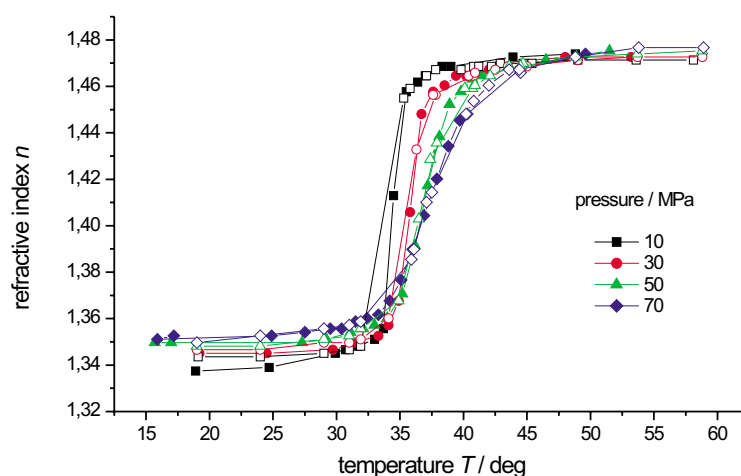
Figure 4.11: Comparison of the gel refractive index recorded at constant pressure (temperature varied, solid symbols) and constant temperature (pressure varied, open symbols). The composition of the gel is: 0 mM SA, 8.6 mM BIS, 700 mM NIPAAm.

incidence indicating that most of the water is driven out and the remaining gel has a refractive index larger than water. Note that due to the large thickness of the hydrogel layer only the refractive index of the NIPAAm gel is probed by surface plasmon spectroscopy. Another feature of the scans at high temperatures is the increased width of the resonance minimum and the extended irregularity of the form of the scan, both of which can be related to increased scattering in the collapsed state of the gel especially since the grating configuration with the light impinging from the solvent side is used. The phase behaviour of the gel at the NIPAAm/substrate interface is observed

as a function of temperature (approximately 15 °C to 65 °C) and pressure (0.1 MPa to 100 MPa).
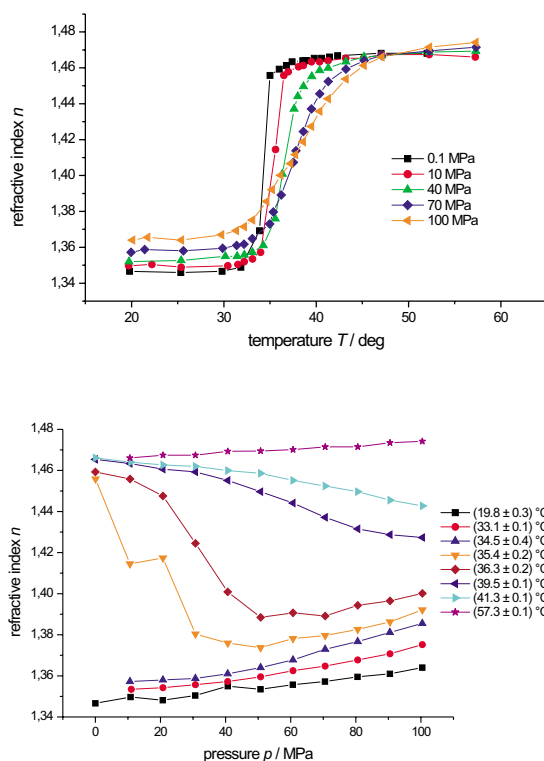
Figure 4.12: The hydrogel (8 mM SA, 692 mM NIPAAm, 8.6 mM BIS) refractive index as a function of temperature at different pressures (top) and as a function of pressure at different temperatures (bottom). For clarity, not all curves are shown and intermediate measurements follow the trends depicted above.

All transitions are fully reversible and no hysteresis is observed. Figure 4.11 depicts two sets of curves of refractive index as a function of temperature at different pressures recorded with two different measurement protocols. The solid symbols represent data where the whole $n(T)$ curve is measured at constant pressure; the temperature is varied before another curve is recorded at the next higher pressure. On the other hand, the open symbols refer to a gel transition where the pressure is varied at constant temperature. Both methods give the same results. The differences that can be seen close to the transition temperature of especially the 10 MPa curves result from a different and rather coarse temperature resolution. Therefore, all measurements are recorded by increasing

temperature and then varying pressure at constant temperature, which accelerates the measurements dramatically. The equilibration time for the gel after each temperature and pressure change was verified in the SPR kinetic mode and ranges from 10 min to 25 min.

The top of figure 4.12 shows the refractive index as a function of temperature and pressure for a sample containing 8 mM SA, 692 mM NIPAAm, 8.6 mM BIS. Following the curve at 0.1 MPa, the refractive index changes from $n(T = 19.8\ °C)$ of 1.347, which corresponds to a gel swollen with water, to $n(T = 52.0\ °C)$ of 1.468, which corresponds to a collapsed and hydrophobic gel phase containing little water. The resulting data are quantified through fitting with a sigmoidal curve, using the parameters n(low temperature), n(high temperature), transition temperature T, and transition width ΔT. For example, this evaluation gives a transition temperature of 34.3 °C and a width of 0.3 °C for the 0.1 MPa curve. This width is relatively small as compared to the width of the same sample at a pressure of 100 MPa, where it amounts to 2.9 °C. Similar to bulk NIPAAm gel, between these two extremes the width as well as the transition temperature increase as a function of pressure. This has been attributed to the disruption of the hydrogen-bonding environment within the gel, especially that surrounding the hydrophobic isopropyl group. The entropy of solution is decreased and causes the Flory interaction parameter χ to increase as a function of pressure. Both the transition temperature and the width of the transition increase as a result [1; 121; 127]. An unusual effect of this phase behaviour is that under certain conditions increasing pressure can actually cause the gel to expand. For example, at 0.1 MPa and 36 °C the gel is collapsed while at 100 MPa and 36 °C it is swollen. This unique characteristic is graphically illustrated in the bottom graph of figure 4.12 and found for all NIPAAm gel samples investigated as part of these experiments. At temperatures above and below the transition temperature of the hydrogel the refractive index increases as a function of pressure as expected due to the increased density of the gel and the solvent. However, at around 36 °C the gel expands with increased pressure. According to thermodynamics the derivative of pressure with respect to volume at constant temperature $(\partial p/\partial V)_T$ must be negative and as a result the compressibility is positive. This contradiction is resolved by referring to the requirement of a closed system [122; 1] in the thermodynamic derivation. In the process of swelling and shrinking water molecules enter and leave the gel network. Furthermore, the pressure is believed not to

be exerted directly on the gel but rather affects the polymer segment solvent interaction causing a shift in free energy that is in favour of the swollen state.
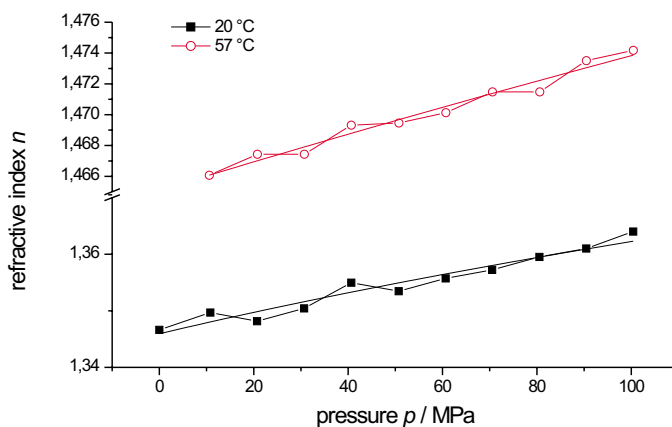
Figure 4.13: The refractive index of a 0 mM SA, 700 mM NIPAAm, 3.5 mM BIS gel as a function of pressure at 19.8 °C (circles) and 57.3 °C (squares). The data is evaluated using the Lorentz-Lorenz equation combined with the Tait equation to give the compressibility of the gel in the swollen (19.8 °C, solid line) and the collapsed (57.3 °C, dotted line) state.

At both, high and low temperatures, the refractive index changes as a function of pressure due to the increased density of water and polymer at increased pressure. To illustrate this effect, the refractive index data at 19.8 °C and 57.3 °C are fitted using a combination of the Lorentz-Lorenz and the Tait equations as described in sections 2.2.1 and 2.2.2 to give the Tait parameter $B(T)$ and the Lorentz-Lorenz constant R_{LL}. From the Tait parameter the isothermal compressibility $\kappa_0(T)$ can then easily be calculated [56; 41]. The resulting values $\kappa_0(19.8 \,°C) = 0.52$ GPa^{-1} ($v_0 = 1.0018$ cm^{3}g^{-1} [128]) and κ_0 (57.3 °C) = 0.17 GPa^{-1} ($v_0 = 1.386$ cm^{3}g^{-1} [129]), however, should only be treated as approximate values since both equations rely on approximations which have proved to hold well for certain liquids and polymers but also have their drawbacks, e.g. in the case of water [4]. A direct measurement of either density or volume change upon variation of temperature and pressure would therefore be preferred but the above values are in good agreement with the literature for the swollen (water) state and the collapsed (polymer) state In conclusion, the exceptional pressure sensitivity of the gel exists only in a small temperature range above

the volume phase transition temperature. The temperature sensitivity of the gel therefore constitutes a prerequisite for its pressure behaviour. Figure 4.14 provides a compilation of these findings in terms of an nTp three-dimensional phase diagram. The refractive index can be correlated to the water content of the gel through a Lorentz-Lorenz calculation and the known relationship between refractive index and pressure. Thus, n can be seen as representing the volume fraction of the polymer. The nT plane is equivalent to the left graph of figure 4.12. Depicted are only the curves for 0.1 MPa and 100 MPa. The np plane intersects with the s-shaped surface of the $n(T)$ curves. At both, low (points A, B) and high (points E, F) temperatures the refractive index increases due to pressure induced density changes as in the lower and upper curve of figure 4.12, right hand side. The plane indicated by the points C and D at a temperature slightly above the phase transition at atmospheric pressure is stair-shaped and corresponds to the curve in the middle in the fig. 4.12. Therefore, the pressure sensitivity relies on the temperature sensitivity of the gel and is simultaneously a result of the increase of the transition temperature and the transition width with pressure. Since the transition occurs in a comparatively small temperature range the pressure sensitivity is also restricted to a narrow range of temperature. [4; 130].
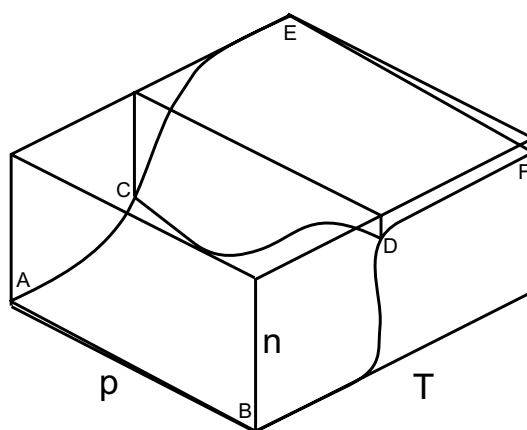
Figure 4.14: nTp phase diagram of a temperature sensitive hydrogel.

The data in figure 4.15 shows the transition temperature of NIPAAm as a function of pressure. The ionisable co-monomer (SA) concentration is varied as a parameter in the top graph and the crosslinking (BIS) density in the bottom graph. With the exception of the 16 mM SA sample all transition temperatures increase monotonously by 3 °C to 6 °C

over a range of 0.1 MPa to 100 MPa. Here, an unusual scatter is found for in the $n(T)$ plot at low pressures resulting in a just as irregular transition temperature. From these data of fig. 4.15, it is clear that the pressure sensitivity of the volume phase transition temperature at the NIPAAm-substrate interface is similar to that of bulk gels [1; 121; 127]. The increase
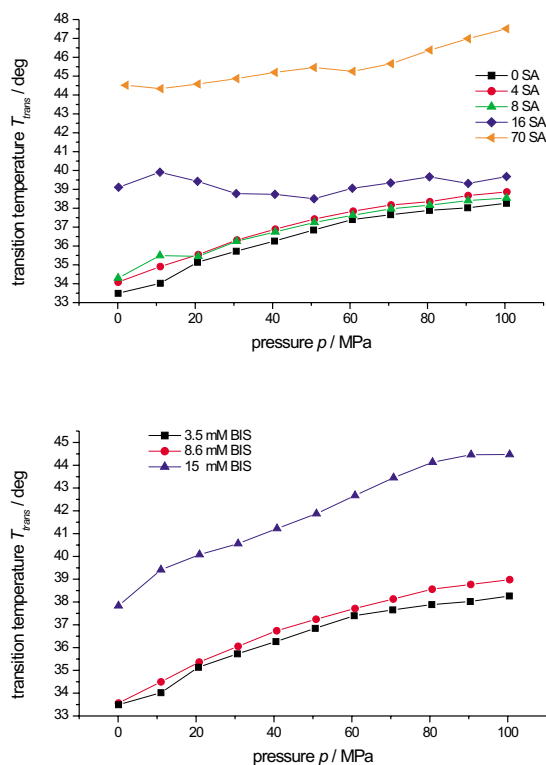
Figure 4.15: Pressure effects on the volume phase transition temperature. All samples labelled with the crosslinking density (x mM BIS) have a gel composition of 0 mM SA and 700 mM NIPAAm. All samples labelled with ionizable co-monomer concentration (x mM SA) have a corresponding NIPAAm concentration of (700 - x) mM and a crosslinking density of 8.6 mM BIS.

of the transition temperature is commonly explained by referring to the influence of the pressure on the hydrophobic interactions within the gel. The hydrophobic interaction is driven by the entropy increase due to water molecules being released from a more or less structured configuration around hydrophobic molecules when such hydrophobic solutes contact with each other. Pressure, on the other hand, promotes the formation of an ordered structure at the expense of thermal agitation. Thus, the interaction of

the water molecules with the polymer is changed as well as the characteristics of the hydrophobic interactions inside the gel. The quantitative description allows the Flory interaction parameter χ to be pressure dependent [1; 121]. NIPAAm gel films constrained by the presence of a fixed substrate and bulk hydrogel are qualitatively similar in terms of the dependence of the transition temperature on pressure. However, there are still some notable differences.

	transition temperature / deg		
SA / mM	bulk gel	0.3 μm film	4 μm film
0	34.3	33.8	33.7
4	34.7		34.1
8	35.9	38.9	34.3
16	36.8	38.9	39.1
32	37.7	42.1	
70	41.9	44.8	44.5
BIS / mM			
3.5	34.2		33.5
8.6	34.3		33.7
15	34.4		37.7

Table 4.2: Volume phase transition temperatures of bulk, very thin (0.3 μm [74]) and thick (4 μm) NIPAAm films of different ionisable co-monomer (SA) and crosslinker (BIS) concentrations at 0.1 MPa.

The transition temperatures at 0.1 MPa vary from those of bulk gels of the same composition as summarised in table 4.2. Shown are the volume phase transition temperatures at 1 bar as a function of ionisable co-monomer concentration and crosslinking density. As known from Flory-Tanaka theory, the transition temperature of bulk NIPAAm gel increases as a function of the SA concentration but is largely unaffected by the crosslinking density. However, as illustrated by both, the data in figure 4.15 and in table 4.2 the gel at the NIPAAm-substrate interface shows further increase in the volume phase transition at higher SA and BIS concentrations. Furthermore, at lower SA and BIS concentrations, the

transition temperature is slightly lower than the one in the corresponding bulk samples. This is analogous to other studies that show the effect of confinement at a fixed substrate altering characteristic transitions in polymeric materials [3; 125; 124]. It is tempting to try and model the constraint as an added stress or pressure within the gel [131] but this is inconsistent with the data in these experiments. In terms of the sigmoidal fit, the constraint has been reported to affect the transition temperature T but not the width of the transition ΔT [123; 132] while added hydrostatic pressure, as shown, affects both, T and ΔT.
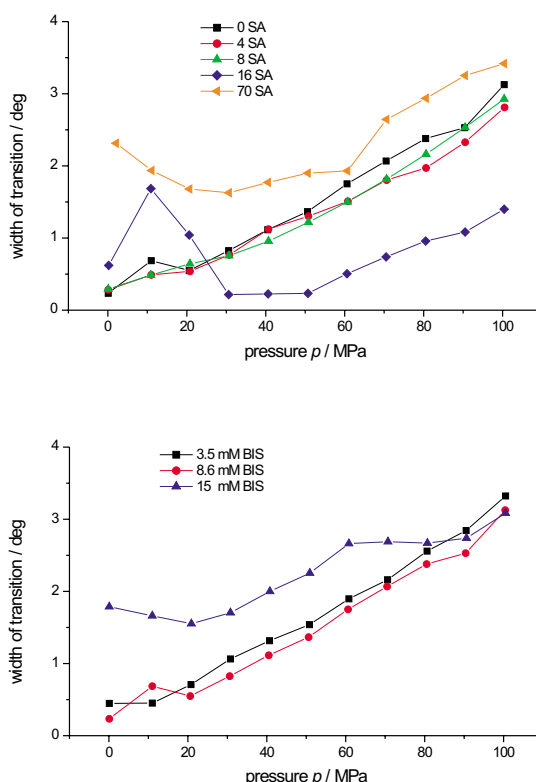
Figure 4.16: Pressure effects on the volume phase transition width for different ionisable co-monomer concentration (SA, top) and crosslinking density (BIS, bottom).

The second feature that differs considerably from bulk NIPAAm gels is the width of the volume phase transition, depicted in figure 4.16 as a function of the SA concentration (top) and the BIS density (bottom). It can be seen that all curves increase more or less monotonously with pressure. However, especially for high SA and BIS concentrations the

scatter of the curves increases resulting in irregular shapes. This finding is in contrast with the results obtained for bulk NIPAAm gels [127; 1]. Although the bulk gel with 0 mM sodium acrylate shows a gradual increase of transition temperature and transition width for the gel of 14 mM SA concentration the transition is reported to be discontinuous up to 20 MPa from where it starts to be continuous. This behaviour is thereafter compared to the critical behaviour of fluids as the Flory-Tanaka theory shows similarities to the description of van der Waals fluids [116]. The hydrogel films studied here all show a continuous transition and an increasing width due to the application of hydrostatic pressure to the system. The constraint of the gel being chemically bound to a surface therefore changes its response to external stimuli such as temperature. From macroscopic observations [126] it is known that NIPAAm gel films on the order of 50 μm show significant distortion as they expand and contract in response to temperature and these transitions can not be viewed as one-dimensional. Most likely there is a characteristic length scale over which the effects of the substrate are felt by the gel film. To explore this further, the results of a separate set of experiments [74] that used a surface-bound photoinitiator [133; 134] are also listed in table 4.2.

This technique allows the thickness of the gel layer to be controlled by the UV exposure time and produces films thinner than those reported in this study. The entire thickness of films of 0.3 μm and thinner, which is of the order of the decay length of an SPR measurement, are thus probed by this set of measurements. The transition temperatures of the thin gel films correspond well with those at the NIPAAm-substrate interface (cf. table 4.2) and the constraint of the fixed substrate then appears to affect the entire film. This does not resolve the issue of the exact length scale needed to describe the system but it can be concluded that the film feels the constraint of the substrate over distances larger than the decay length of the surface plasmon. Further investigations on this topic [135] reveal that for gel thicknesses below 1 μm the transition temperature is increased. For gels thicker than 1 μm the closest layer to the surface still has an increased transition temperature whereas the second domain further away from the substrate shows a decreasing volume phase transition temperature. Additionally, the refractive index of the collapsed state decreases as the film thickness decreases, indicating that the gel is not completely collapsed at temperatures above the volume phase transition temperature. Interestingly, this effect of a partially collapsed gel

is also observed for bulk gels as a function of pressure [1].

The confinement of the gel through its bonding to the surface yields yet another effect, shown in figure 4.17. The polymer volume fraction of the gel films can be calculated from the refractive index of the film. In bulk gel, the addition of ionisable counterions swells the gel significantly and the polymer volume fraction decreases. However, it is
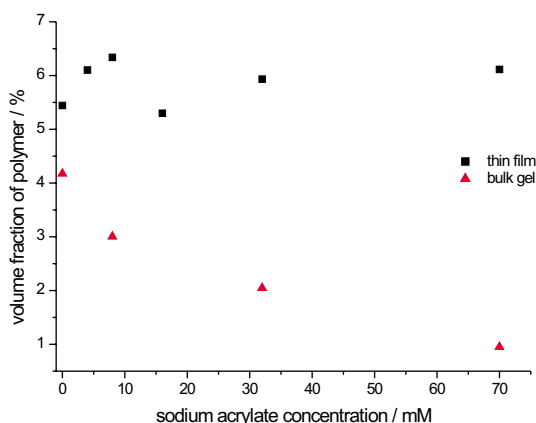
Figure 4.17: Equilibrium swelling below the volume phase transition temperature. The volume fraction of polymer in the gel samples is calculated from the refractive index in the case of the thin film and from the equilibrium-swelling ratio in the case of the bulk gel.

apparent from the data in fig. 4.17 that the swelling ability of counterions in the thin film is substantially less than in the bulk. Thus, the effect of confinement on ionized NIPAAm gels is that, although the transition temperature increases as in the bulk, the associated swelling of the gel is not present. As a thought experiment, a one-dimensional analogue to Flory-Tanaka theory should have a more rapid increase in elasticity free energy as the gel expands and polymer volume fraction decreases. This could explain the reduced swelling for the gel at the NIPAAm-substrate interface but it is unclear how this will affect the volume phase transition temperature and the width of the transition.

4.3 Conclusion

It is demonstrated that stable silica films on noble metals can be generated by applying sol-gel chemistry. The different steps in the preparation procedure are discussed in detail.

Special emphasis is set on the characterisation of the roughness of the surface. These films are resistant to buffer solutions containing various salts and can be readily used in a liquid cell format for investigating the build-up of supramolecular architectures in real-time. The stability of these films under high pressure and temperature conditions is found to be quite remarkable, which enhances their suitability for experiments even at harsh conditions. The films can be chemically treated to introduce various reactive groups, which can then be used for various surface studies. The flexibility of introducing various silane coupling agents on these stable silica sol-gel films on noble metals might greatly enhance their applicability in studying problems related to fluorescence quenching, biomolecular interactions, or polymers at interfaces.

NIPAAm gels layers are presented as an application of sol-gel films. The experiments are a first step towards understanding the volume phase transition in NIPAAm gels under lateral constraint. This is particularly relevant for a number of applications such as thermally selective membrane separations [118] and thermally activated surfaces in biomaterials [119]. These applications use thermoresponsive hydrogels at surfaces and interfaces, and the understanding of bulk hydrogels cannot necessarily be extended to these types of geometries.

As demonstrated, NIPAAm gel at a fixed interface is a complex system and the mobility of the gel at the interface most likely has a characteristic length scale associated with it. The data also suggest that the constraint can not simply be modelled as an added stress or pressure within the material. However, the effect of confinement on NIPAAm at a fixed interface is shown to alter the transition temperature, especially for ionised or highly crosslinked gels, and to significantly decrease the swelling ability of ionic species in the gel. Furthermore, the effect of increased hydrostatic pressure is to increase the transition temperature and the width of the transition, which is to some extend similar to bulk gels. However, the width of the transition for ionised gels does increase monotonously for thin films and does not display any discontinuity features comparable to a van der Waals fluid as reported for bulk NIPAAm gels. Due to the pressure dependence of the transition an interesting phase behaviour slightly above the phase transition at ambient pressures is produced: under certain conditions the gel can expand in response to increased pressure.

5. DNA Hybridisation at Elevated Pressures

The goal of the measurements presented in this section is the study of hybridisation reactions at elevated pressures. For this purpose a universal binding matrix consisting of a biotinylated thiol and subsequent adsorption of streptavidin is immobilised onto the gold surface. Onto this platform a biotinylated DNA probe is adsorbed, to which an appropriate fluorescent labelled DNA target sequence hybridises (compare fig. 5.1). In the following the models and findings of duplex formation reactions in bulk at elevated pressures are summarised first. Then a brief outline of the adsorption behaviour of the different sections of the layer system is given. Thereafter, the attention is drawn to the pressure and temperature stability of the binding matrix layers and the DNA target first before turning to the actual hybridisation measurements. Here, two different target sequences are investigated; one is a 0 mismatch and the other a 1 mismatch sequence as compared to the probe oligonucleotide.
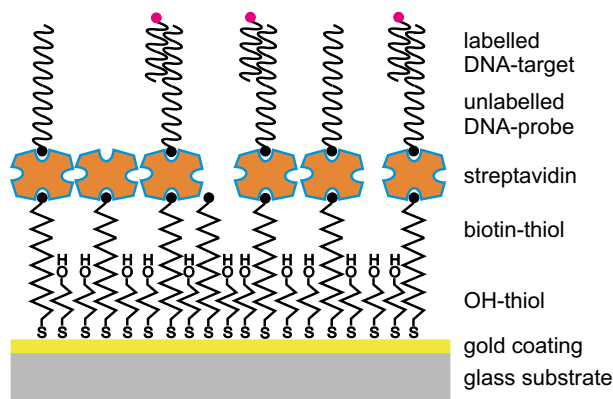
Figure 5.1: Layer scheme of the supramolecular architecture used to study DNA hybridisation. The order starting from the gold surface is: biotinylated/OH-terminated thiol mixture, strepatvidin, DNA probe, DNA targed (fluorecent labelled).

5.1 Hybridisation Reactions at Elevated Pressures

The thermodynamic stability of nucleic acid duplexes is generally described by a pseudo-first-order transition between the double helical form and the separated complementary single stranded coil form [136]. This type of transition can be induced by either temperature or pressure. Although the majority of biological processes occur at conditions of constant temperature and pressure, temperature and pressure dependent studies represent the only way to thermodynamically characterise the molecular interactions contributing to the stability of a given sequence-specific DNA conformation. Thus, studies of biochemical systems at high pressure usually have the aim to gain a better understanding of the system's behaviour at ambient conditions. Since the first report of the effect of pressure on the secondary structure of nucleic acids by Hedén et al. in 1964 [137] - The melting temperature of natural calf thymus DNA was reported to increase by 6 °C after being pressurised to about 260 MPa. - the interest in pressure effects on nucleic acids has increased. Especially the role of hydration in biochemical and biophysical processes is found to be an issue of interest. The majority of publications deal with the thermodynamics and kinetics of the formation and denaturation of DNA double helices whereas only a small number have focused on RNA or the effect of pressure on the structure of the double helix or higher order DNA hybrids.

In addition to the less common circular dichroism spectroscopy [138], dynamic light scattering [139], and fourier transform IR spectroscopy [140], UV absorption spectroscopy represents the most widespread measurement technique to characterise the stability of DNA duplexes. Nucleic acids absorb less (hypochromism) when two complementary strands form a double helix and the absorption increases (hyperchromism) when, e.g. at high temperatures, the duplex splits into two separate strands. Thus, the melting temperature T_m of the transition can be easily followed by the intensity change in UV spectroscopy. Thermodynamic parameters can be obtained from the temperature dependence of the optical signal measured at different pressures by treating the separation process as a phase transition. Then, the Clausius-Clapeyron equation

$$\frac{\mathrm{d}T_m}{\mathrm{d}p} = \frac{T_m \Delta V}{\Delta H} \tag{5.1}$$

can be employed to calculate the volume change ΔV of the transition if the enthalpy difference ΔH is at hand.

The early investigations were carried out on natural sequences like calf thymus DNA. Nordmeier et al. [139], for example, used dynamic light scattering in their studies to find that the volume change of the transition increases with ionic strength and decreases with pressure. Although general principles and connections can be demonstrated by using natural DNA only by studying synthesised oligomers and polymers with defined sequences the precise effect of pressure on the thermodynamics of helix formation can be established. One of the most examined synthetic systems is the one containing only AT base pairs - poly(dA)poly(dT) and poly(d(A-T)). Double and triple stranded DNA polymers showed increased stability, i.e. T_m increases linearly with pressure for solutions containing sodium or potassium ions [141]. Also for poly(d(G-C)) with a transition temperature above 100 °C T_m increased linearly as a function of pressure. In the field of synthetic oligomers, studies have mainly focused on the influence of the chain length on the volume change of the transition. The effect that terminal bases of a double helix are less stable than base pairs distant from an end is termed 'fraying'. According to MacGregor et al. [142] the consequence of the frayed base pairs on the transition of poly(dA)$_x$poly(dT)$_x$ with $x = 11, 15, 19$ is a negative volume change, which is clearly in contrast to the normally positive volume change linked with the denaturation process. Contrary to the findings that $\mathrm{d}T_m/\mathrm{d}p$ is positive and therefore the associated volume change is also positive (eqn. (5.1)) calorimetric measurements on polymeric AT- and AU-containing DNA duplexes revealed that ΔV is negative for $T_m < 50$ °C and positive for transition temperatures above 50 °C [143]. Dubins et al. [136] formed a model, which anticipates a destabilising effect of pressures below about 200 MPa for sequences with a melting point below 50 °C and stabilisation for systems with $T_m > 50$ °C. For pressures above 200 MPa these findings reverse.One picture that unites three important parameters, namely the type of salt employed in the studies, the salt concentration, and the pressure is based on the concept of the internal pressure of a solvent. Electrostriction, i.e. the decrease of net volume of e.g. water in the presence of ions, results in a compression of adjacent water dipoles equivalent to a few hundred MPa. This pressure, referred to as the internal pressure, can be used to explain why the transition temperature of certain duplexes increases with an increasing concentration of e.g. NaCl however decreases with other types of salts, as for example NaClO$_4$ [144]. Different salts result in different internal pressures that can also turn negative when very large anions reduce the charge density to below the value of wa-

ter, effectively decreasing the interactions as compared to those among water molecules. Within this terminology also the hydrostatic pressure can be thought of as an additional contribution to the internal pressure of the system.

5.2 Immobilisation Matrix

In this section, experimental results on the immobilisation matrix consisting of the biotinylated/OH-terminated thiol mixture, the streptavidin layer and biotin-terminated DNA probe strand are presented. The procedure of the consecutive immobilisation of the respective layers is well established in our group [108; 58; 85]. Nevertheless, as it represents a fundamental matrix system upon which the detection scheme is based a short summary of the results is given.

5.2.1 Binding Matrix at Ambient Conditions

All data presented are recorded in the grating configuration inside the high-pressure cell utilising a flow cell that has been especially designed for this purpose. Figure 5.2 shows the flow cell, which has a volume of less than 100 μl and is mounted in-between the front sapphire window and the gold-coated sample. It should be noted, however, that in order to use it as a flow cell in high-pressure fluid-exchange experiments a suitable pump and
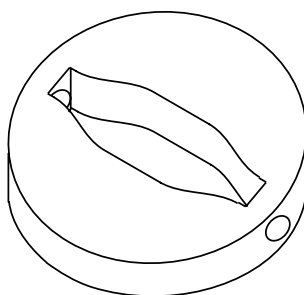
Figure 5.2: Sketch of the flow cell constructed for the grating high-pressure SPR cell.

leak valve has to be utilised such that a constant flow through the cell is established. Also, to be able to conduct experiments with different solvents an intelligent pump system has to be used. Since this is not the major aim of the experiments presented here all data are collected at atmospheric pressure and 25 °C.

Figure 5.3 (top) illustrates the adsorption processes of the two layers and the subsequent DNA probe as a time-dependent reflectivity measurement whereas the bottom graph of fig. 5.3 depicts the angular scans taken before and after the kinetic measurements, respectively. With the aid of the scan curves the thickness of the three layers
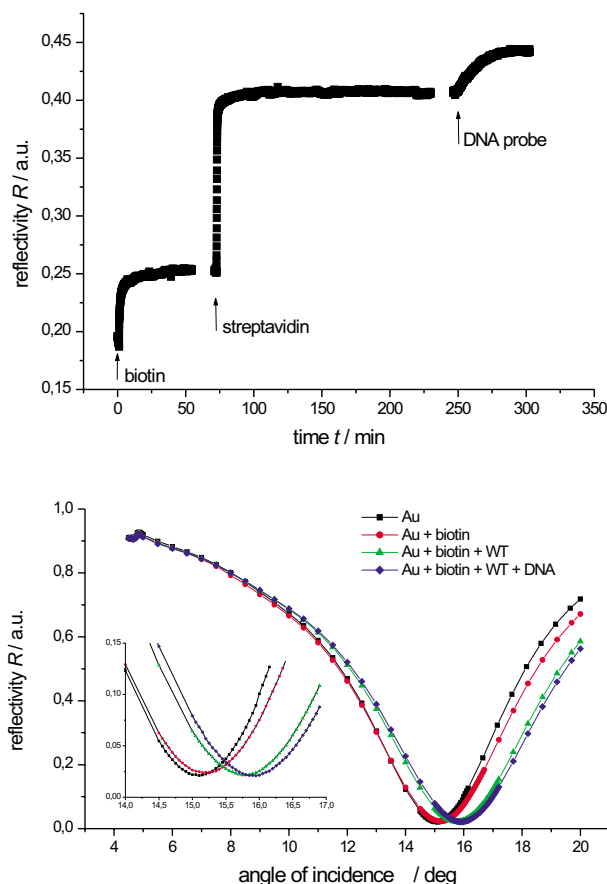
Figure 5.3: Top: Adsorption kinetics of the biotinylated thiol mixture on gold, the consecutive immobilisation of streptavidin, and the adsorption of the DNA probe. Bottom: The corresponding scan curves to the adsorption kinetic data.

can be evaluated assuming refractive indices for the different layers. As can be seen in the kinetics the adsorption of the thiol mixture and the streptavidin is completed after 15 min to 25 min and the resulting streptavidin matrix is very stable throughout a time period of more than 120 min. The consecutive injection of a 0.5 μM biotinylated DNA probe leads to an adsorption of the biotin end of the DNA to the proteins. This process takes somewhat longer, which is reasonable considering the molarity of the DNA solution.

The optical constants used for fitting the scan curves are listed in table 5.1.

layer	d / nm	ϵ
thiol	0.7	$2.25 + i \cdot 0$
streptavidin	4.3	$2.1025 + i \cdot 0$
DNA probe	1.9	$1.891 + i \cdot 0$

Table 5.1: Optical parameters used for fitting the scan curves of figure 5.3.

The value of 0.7 nm thickness of the thiol layer seems a little small compared to the ones reported. However, the thickness of the thiol varied from sample to sample and usually lies in the range between 0.7 nm on the very low end and about 1.4 nm at the upper end, which is comparable to the values reported [58; 85]. One also has to consider that in the case of the grating the surface is not smooth but corrugated, which has some influence on the self-assembly behaviour of the thiols resulting in a comparatively small thickness. The thickness of 4.3 nm for the streptavidin layer corresponds well to literature. From this value the adsorbed amount of protein can be calculated if the refractive index of it is known as well as the refractive index increment of the dissolved molecule with concentration [58; 85]. As result, the area per protein is calculated to be approximately 44 nm^2. Yet, the determination of the streptavidin structure by x-ray spectrometry shows that its surface area is only 23.4 nm^2. From these findings it is evident that the layer is not as highly ordered as a crystal - the surface coverage being 53 % - and that defects in the structure exist. However, the streptavidin layer in this work is used as a binding matrix for DNA probe oligonucleotides for the study of DNA hybridisation reactions. One therefore has to provide firstly a surface that permits easy access for the target DNA sequences to permit the duplex formation and secondly a matrix where no apparent interactions like crowding effects between the probe molecules can take place. Thus, the loosely packed streptavidin surface with approximately 44 nm^2 per molecule as compared to only 3.1 nm^2 for a double helix serves as convenient platform for studying DNA hybridisation. The thickness of the probe is calculated to be 1.9 nm for an assumed refractive index of n = 1.375. Compared to literature, which gives values of 3.4 nm per 10 bases of a B-DNA helix that add up to approximately 10 nm for 30 bases, this seems to be an extremely small value. However, the measured value represents the optical thickness of the layer

and, moreover, no information about the surface coverage is given. Another argument for a lower thickness than 10 nm comes from the fact that the probe as injected is single-stranded. In the case of a random-coiled probe an end-to-end distance (excluding the biotin) average value of 5 nm can be assumed [58]. It has also been shown [58] that the DNA sequence used in these experiments is likely to form hairpins, which results in a drop in thickness as well.

5.2.2 Stability of Biotinylated Thiol

For the stability of the binding matrix it is essential that the various layers constituting it are stable. The first layer is formed by a mixture of a biotinylated and an OH-terminated thiol, which self-assemble on the surface. As it is the bottom layer the data presented go more into detail whereas the stability of the streptavidin layer will be described in a briefer fashion later on.
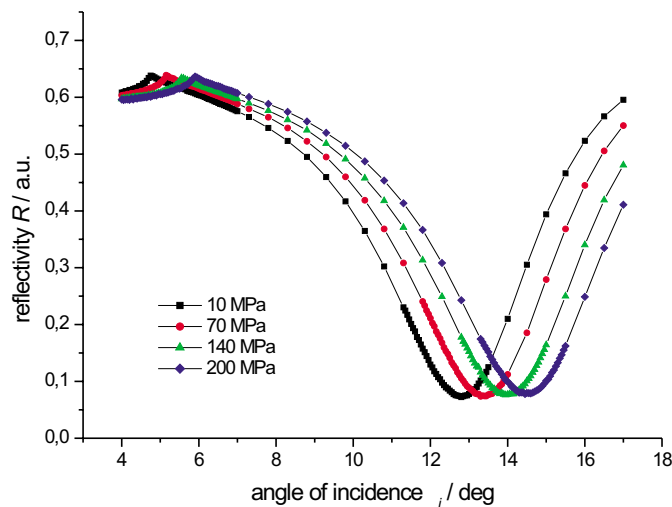
Figure 5.4: Scan curves of the system gold / thiol mixture / PBS buffer at 19.2 °C and different pressures.

Kleideiter at. al. [56] showed that evaporated gold layers are stable in water and some organic solutions at elevated pressures. Due to its small compressibility the angular scans at elevated pressures can be fitted with constant parameters for gold and the only variable is the refractive index of the pressure medium. Hence, such behaviour can be assumed

for the system gold/biotinylated/OH thiol mixture/PBS as well. Typical scan curves at different pressures as depicted in figure 5.4 are evaluated by keeping the gold parameters constant and by varying the refractive index of the pressure medium and the thickness of the thiol layer. As a surface plasmon resonance curve only provides one minimum only one parameter of the adsorbed layer can be extracted from the scan curves. Thus, the refractive index of the thiol is assumed to be constant at $n = 1.5$. The shift of the edge of total reflection to higher angles indicates that the pressure compresses the buffer. Consequently, its density and refractive index increase. The minimum of the curve is fitted by adjusting the thickness of the biotinylated thiol layer.
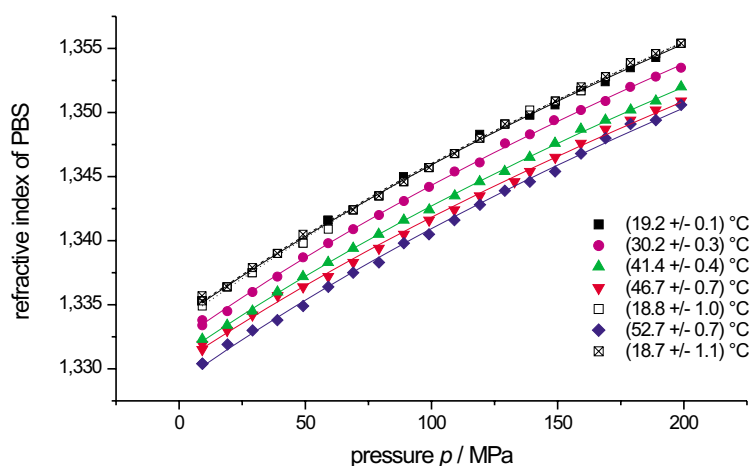
Figure 5.5: The refractive index of PBS buffer at various temperatures and pressures as evaluated from the edge of total reflection. Also shown are the Lorentz-Lorenz/Tait fits to the corresponding curves (solid lines).

Figure 5.5 depicts the refractive index of the PBS buffer as a function of pressure at different temperatures. The protocol for increasing the temperature starts from an initial 20 °C to 30 °C, 40 °C and 45 °C, decreases to 20 °C, then increases again to 50 °C and finally leaves the cell at 20 °C. This procedure reflects the idea that temperature has some effect on the stability of the thiol layer yet the pressure variation disguises or inhibits desorption. Therefore, the second and third pressure cycle at 20 °C is meant to confirm the stability of the layer also at high temperatures. If all of the resulting values for the thickness of the thiol and the refractive index of the pressure medium are

unchanged as compared to the first pressure run the system is assumed to be stable. The data in fig. 5.5 clearly shows that at least the refractive index of the buffer remains unchanged at 20 °C. The little scatter occurring in-between the three runs at 20 °C can be attributed to slightly different temperatures. Consequently, even if there are thiol molecules rearranging at the surface or desorbing as consequence to the pressure and temperature variation it does not effect the refractive index of the buffer. Regarding the curves at higher temperatures, they are shifted to lower refractive indices due to the decrease of density resulting from the temperature increase. Pressure has the opposite effect on the refractive index. The compression leads to an increased density and thus increased refractive index. This behaviour can be evaluated with the Lorentz-Lorenz and Tait equations. The results of this evaluation are shown in table 5.2.

T / °C	v_0 / cm^3/g	R_{LL} / cm^3/g	B / MPa	κ_0 / GPa
19.2 ± 0.1	1.0017	2369.71 ± 22.18	0.2065 ± 0.0001	0.377
30.2 ± 0.3	1.0044	2330.19 ± 17.74	0.2062 ± 0.0001	0.384
41.4 ± 0.4	1.0084	2391.07 ± 15.97	0.2062 ± 0.0001	0.374
46.7 ± 0.7	1.0106	2472.07 ± 32.37	0.2060 ± 0.0001	0.362
18.8 ± 1.0	1.0016	2302.46 ± 20.18	0.2064 ± 0.0001	0.388
52.7 ± 0.7	1.0134	2321.63 ± 31.15	0.2061 ± 0.0001	0.385
18.7 ± 1.1	1.0016	2368.24 ± 20.84	0.2066 ± 0.0001	0.378

Table 5.2: Parameters resulting from fitting the Lorentz-Lorenz/Tait equations to the data of the refractive index of PBS. The values for v_0 are extrapolated from [128].

As mentioned in section 2.2.1 the Lorentz-Lorenz refractivity R_{LL} does not necessarily have to be a constant with respect to temperature and pressure (although assumed in the derivation of the equation). However, the deviation of R_{LL} from constant behaviour for water is of the order of $\Delta n = 10^{-4}$ and therefore not detectable with SPR [4]. The derived values for the Lorentz-Lorentz refractivity reflect this reasoning in that no dependence on the temperature can be seen. Quite different is the behaviour of the Tait parameter B. Equation (2.66) gives the commonly assumed relation between the Tait parameter and temperature. As assumed, a decay of B with temperature is also found in the data. In the

presented temperature range also no significant dependence of the compressibility on T can be found. The absolute values are comparable to those found for pure water [4] although the salt concentration in the buffer should decrease the compressibility somewhat [130]. However, since the buffer contains only small amounts of salt no pronounced deviation from the values for water are expected.
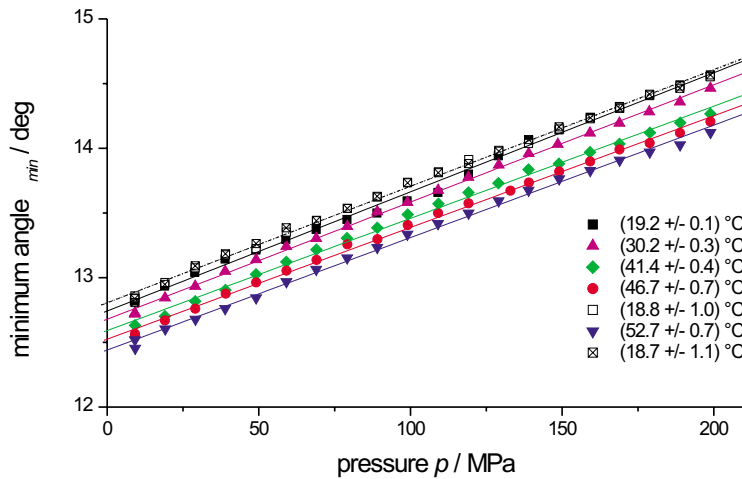
Figure 5.6: The minimum angle of the scans vs. pressure at different temperatures. The solid lines represent a first approximation linear fit of the respective curves.

The pressure stability of the thiol layer itself is best reflected by the position of the minimum angle of the surface plasmon resonance. The evaluated thickness of the layer would also suit this purpose but the values are not quite as precise because a value for the refractive index has to be assumed in order to fit the thickness. Despite the fact that the refractive index can also be extracted from the same curves there is still a certain error connected to it. This has an enormous impact on the determination of an accurate thickness. In figure 5.6 the minimum angle is plotted versus pressure at the same temperatures as described above. The same general behaviour as in fig. 5.5 is found. Temperature and pressure influence the refractive index of the pressure medium and consequently the whole surface plasmon angular scan curve is shifted following the density changes. In addition, the information about the layer behaviour is included in the minimum position. Again, there is virtually no shift between the values of the three runs

at 20 °C. If there was some desorption occurring during the pressure and temperature cycles the minimum would shift to smaller values indicating a decrease of the average layer thickness. In order to compare the various datasets of the same system the curves are fitted linearly, indicated in the graph by the lines.
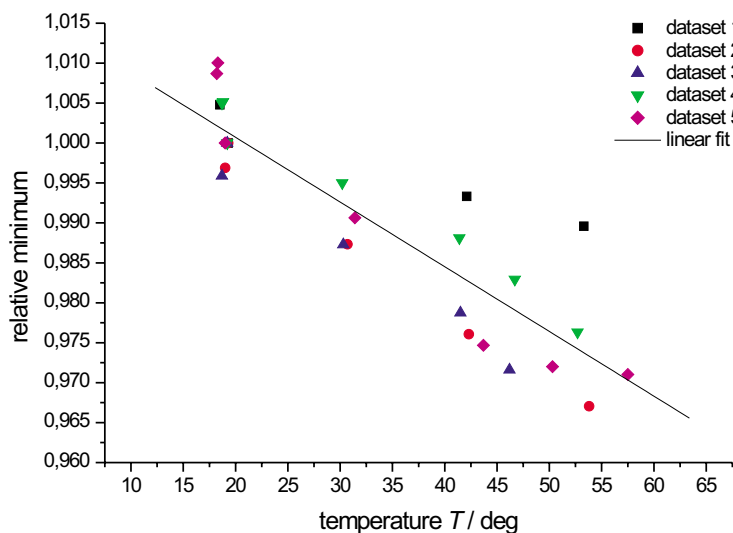
Figure 5.7: The relative minimum position of the plasmon resonance at 0 MPa as a function of temperature as determined by linear fits to the data shown in fig. 5.6.

From this fit two parameters can be extracted, the zero pressure minimum angle and the slope with pressure. These two film characteristics can be compared in a statistical way to measurements of the same system on different samples. However, since the exact position of the resonance minimum depends on the properties of the grating only the relative minimum angles can be compared in a meaningful way. Figure 5.7 shows the position of the relative resonance minimum at 0 MPa as evaluated from $\theta_{min}(p)$ curves as a function of temperature. First, a decrease of the minimum position with temperature is observed as already described above. Second, all angles seem to lie on a straight line when fitted with a linear function. There is no drop of the minimum angle observed at high temperatures indicating that the thiol remains nicely bound to the surface even at temperatures as high as 57 °C. However, the data at the lowest temperature (approx. 20 °C) give a hint that there might be a stability problem as the points for the second

and third pressure cycle all tend to be at lower values than the ones for the first pressure run. Compared to the scatter of the whole dataset though one might also argue that this drop lies within the error of the measurement. The overall behaviour of the layer with temperature can be expressed through a linear fit to the data (solid line in fig. 5.7), the slope of which might be interpreted as some sort of thermal expansion coefficient that is however not related to any volume change.
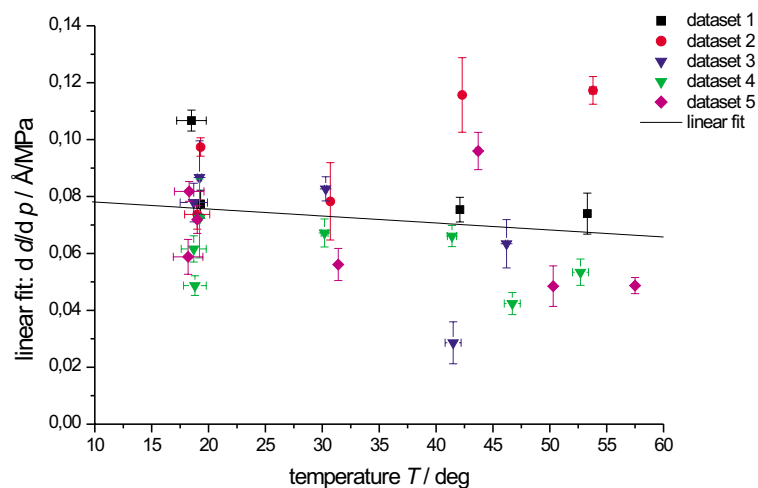
Figure 5.8: The slope $\partial d/\partial p$ of the thiol layer (refractive index assumed to be constant and equal to $n = 1.5$) as a function of the temperature. The solid line represents a fit to the average of all presented datasets.

The second quantity that can be extracted from fig. 5.6 is the slope of the minimum position with pressure. More expressive though seems to be the slope of the thickness of the layer (determined at constant refractive index) with pressure. Here, the scatter in the data due to the evaluation procedure, as explained above, is averaged and the slopes of different datasets are plotted as a function of temperature in figure 5.8. Although the data are quite noisy (as may be again partly attributed to the evaluation method) there are a few things noteworthy: Firstly, the slopes are all positive. The thickness of the layer therefore increases with increasing pressure. This finding of a negative compressibility is somewhat surprising, however can be reasoned by referring to the constant refractive index of the layer that is assumed in the evaluation. Rather, the refractive index of the layer should increase with pressure due to an increased density. (If the increased pressure

does not lead to a higher solvability of the molecules in the pressure medium.) Thus, the positive slope is presumably an artefact produced by the evaluation method and does not reflect the actual behaviour of the layer. Nevertheless, if desorption took place the $d(p)$ correlation should change leading to a change in the slope $\partial d/\partial p$ with temperature. Yet, as already pointed out in the previously discussed graphs, no abrupt change in the slope at e.g. high temperatures is visible. Hence, the thiol layer can be assumed to be stable at pressures up to 200 MPa and tempertures between 20 °C and 57 °C.

5.2.3 Stability of Wildtype Streptavidin

The binding of streptavidin to the biotinylated thiol completes the preparation of the binding matrix. The pressure and temperature stability has strong impact on any subsequently adsorbed layer and is therefore a prerequisite for the hybridisation reactions that are presented in the following section. The streptavidin layer can only be as stable as its
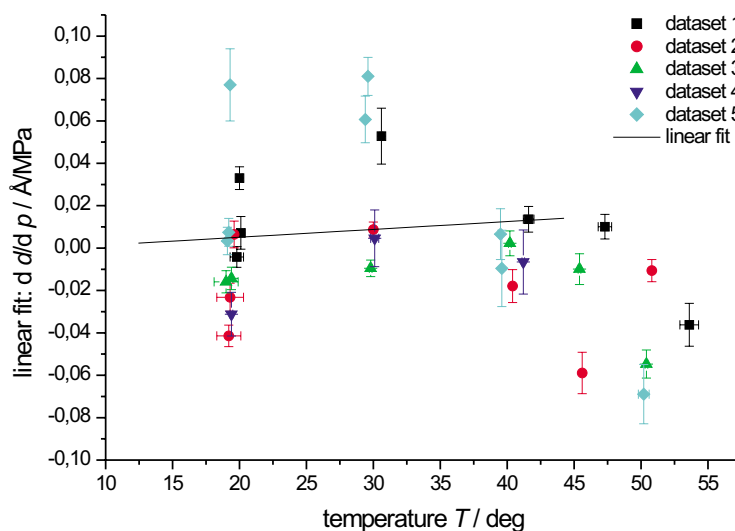
Figure 5.9: The slope $\partial d/\partial p$ of the streptavidin layer (refractive index assumed to be constant and equal to $n = 1.45$) as a function of temperature. The solid line represents a fit to the average of all presented datasets up to 40 °C.

preceding layer, which has proven to be stable at the examined temperature and pressure interval, though. The measurement and evaluation strategy in this section follows closely

the one presented in the previous section. For comparison only the plots of $\partial d/\partial p$ vs. T and $\theta_{min}(T)$ will be presented.

The slope of the thickness of the streptavidin layer with pressure as a function of temperature is depicted in figure 5.9. In contrast to the results of the previous section the average thickness (solid line) does not increase with pressure but remains more or less constant ($\partial d/\partial p \approx 0$). Again, it has to be noted that for the thickness evaluation a constant refractive index ($n = 1.45$) is used even though temperature and pressure are varied. The net outcome is therefore a mixture of refractive index increase and thickness decrease. Nevertheless, the major result of graph 5.9 is that the slope drops abruptly at a temperature of around 35 °C to 45 °C depending on the dataset. This can be interpreted as a first sign that the layer is not stable at elevated temperatures yet remains unaltered upon pressure increase to 200 MPa at low temperatures.
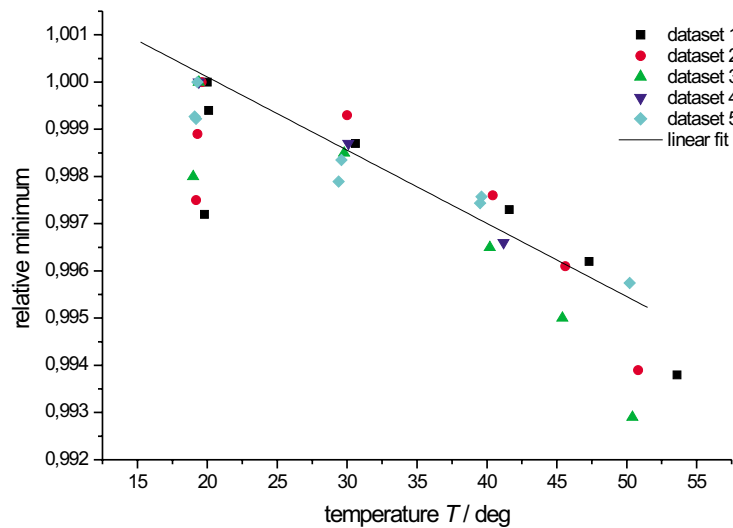
Figure 5.10: The relative minimum position at 0 MPa of the plasmon resonance of the system gold/biotinylated thiol/streptavidin/PBS.

A clearer picture of these findings is shown in figure 5.10, in which the relative minimum position of the surface plasmon resonance is plotted versus temperature. Clearly, the points at 50 °C and above are off the straight line, which is a linear fit to the first part of the data. This means that the layer thickness is decreased at high temperatures - an additional indication that the streptavidin desorps from the surface. Another feature that

reflects this process is the fact that the minimum position after returning from elevated temperatures to the initial temperature is extensively shifted towards lower angles. This means that the desorption is not reversible and that no re-adsorption takes place when the temperature is lowered again. Therefore, it can be concluded that from 45 °C to 50 °C the streptavidin layer gets unstable whereas pressure does not have any noticeable effect on the stability of the system. However, if the maximum stability value is compared to literature ($T_{max} \approx 40$ °C - 45 °C, [145]) a slight increase in the stability can be deduced. This statement, though, has to be confirmed and in particular has to be based on a larger amount and more accurate (temperature-wise) measurements.

5.3 Fluorescence Measurements on Oligonucleotides

The principals of nucleic acid hybridisation and the stability of the formed double helix has already been presented in section 3.3.3. The melting temperatures of such systems are usually deduced from UV-VIS spectrometric or calorimetric measurements and are performed in solution. However, these values do not correlate to the ones of immobilised DNA on sensor chips since here the geometry and the surface potential plays an important part. Factors like the the spatial restriction, and the orientation of the molecules extremely influence the interactions with the target sequence and as a consequence different affinity constants will be derived.

This section is concerned with the basic question of how pressure influences the hybridisation reaction of two single stranded DNA sequences, one of which is bound to a flat surface. Since the melting of a duplex is closely related to temperature this parameter is also varied in order to get a clearer picture of the reaction. The observations are discussed within the framework of the Langmuir adsorption that has been shown to describe the temperature effects on the same oligonucleotide sequences [145] well. At first, a DNA probe that is biotinylated at the 5' end and carries a fluorescent label at the 3' end will be characterised. Then, the hybridisation of a labelled one-mismatch target sequence with respect to the same but unlabelled DNA probe is shown. It represents a less stable hybrid than its zero-mismatch relative, which is described thereafter, and therefore gives a clearer demonstration of the consequences of pressure on the system. A comparison of the results concludes this section.

5.3.1 Characterisation of DNA Probe Layer

The temperature and pressure behaviour of the DNA probe sequence that is linked through a coupled biotin at the 5' end to the strepatvidin and that is fluorescent labelled with a Cy5 molecule at the 3' end is shown in figure 5.11. Since the pressure cell and the pump system used here do not provide the option to follow the adsorption of any species at elevated pressures online - Due to the construction the cell shows poor mixing properties and the pump system is not designed for exchanging fluids at high pressures. - the binding process is followed at atmospheric pressures. The adsorption of the same (unlabelled) sequence onto the streptavidin layer has already been presented in section 5.2.1 and it is therefore omitted here. The lower part of the figure shows the temperature and pressure variation protocol that is kept virtually constant throughout the whole section on DNA hybridisation. The adsorption of the layer is carried out at a temperature of 25 °C and atmospheric pressure. Then the pressure is increased to 10 MPa where figure
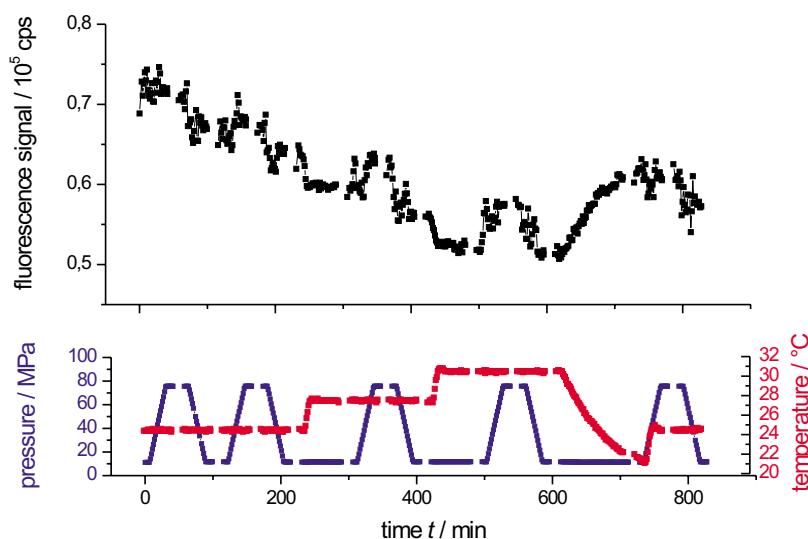
Figure 5.11: Top: Fluorescence signal of the Cy5 labelled DNA probe sequence as a function of temperature and pressure. The single strand (500 nM) is immobilised on a streptavidin layer. Bottom: The temperature and pressure profile during the measurement. Note the answer of the fluorescence signal on the stimulus of an increased temperature or pressure.

5.11 starts. In order to keep the concentration unaltered by mixing with the pressure medium a largely exceeding volume of DNA target (500 nM in PBS buffer) is injected into the cell from the pump side through a T-connection. Two first pressure cycles from 10 MPa to 80 MPa and back to the initial value are executed in order to see their influence on the fluorescence signal. Then, the temperature is increased twice by 3 °C together with another pressure cycle, respectively. The system is cooled down again to 25 °C followed by a final pressure cycle. The upper part of fig. 5.11 shows the fluorescence signal as a function of time. Clearly visible are the two distinct drops of fluorescence intensity upon increasing the temperature and its recovery when the temperature is set to the initial value again. Note also the influence of pressure on the signal. Increased pressure leads to an increased intensity and vice versa. Another feature of the curve is its downward trend indicating that some fluorescence signal is lost with time. The discussion of this phenomenon is given below; however, it should be noted that bleaching of the fluorescence label can be ruled out. In all measurements a shutter system blocked the laser beam for 90 s and it only opened briefly for the data point to be taken. It is therefore assumed
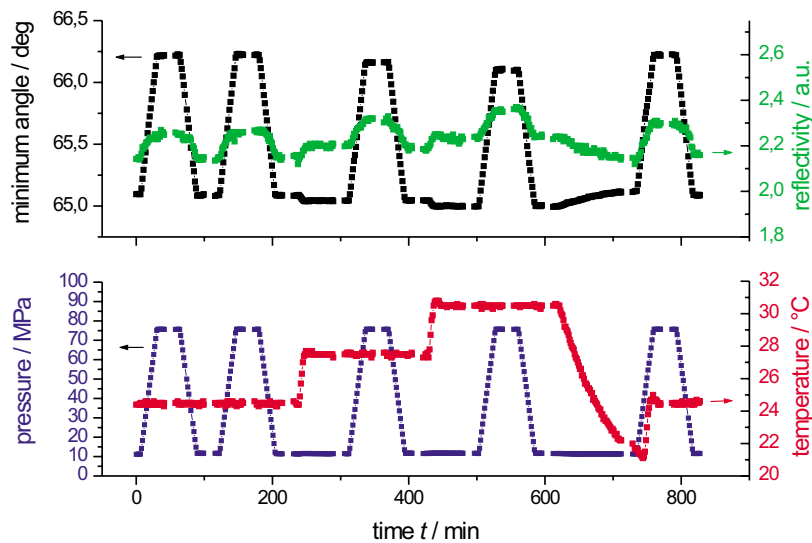
Figure 5.12: The resonance minimum angle and the surface plasmon reflectivity (top) recorded during the measurement. The change of the thermodynamic variables T and p (bottom) can clearly be followed in the minimum position and the reflectivity.

that the labelled molecules do not deteriorate due to any bleaching effect.

When varying the pressure one more technical aspect has to be considered. The increasing pressure changes the density of the medium considerably. On the contrary, the small temperature changes do not extensively alter the refractive index of the solution. Consequently, the normal method to record the reflectivity or fluorescence as a function of time at a constant angle of incidence cannot be applied here as the fluorescence curve (cf. fig. 5.15) shifts with the surface plasmon resonance that is giving rise to it. Due to the angle shift the fluorescence would drop with increasing pressure and no effect of the system itself could be extracted. As a result the kinetic mode that is following the minimum of the resonance curve is used in all measurements. It is assumed that with shifting the angle of incidence the observation position within the fluorescence peak stays constant since the minimum of the resonance shifts to the same extent as the fluorescence curve. Figure 5.12 illustrates the effects of temperature and pressure (lower part) on the SP resonance position and the reflectivity (upper part) when the set-up automatically follows the minimum. The minimum angle increases, as expected, considerably with pressure and decreases only slightly with temperature. The reflectivity increases with both parameters; the temperature seems to have a more pronounced influence, though. Yet, the net effect on the reflectivity is almost negligible as can be read of the corresponding scale.

5.3.2   Characterisation of Mismatch One Hybridisation

Figure 5.13 illustrates the hybridisation reaction of a fluorescent-labelled one mismatch target to an unlabelled probe that is bound to the surface. Shown in the top panel are the reflectivity and the background fluorescence signal before the injection of the 500 nM target sequence (squares) and the fluorescence signal after the reaction has reached equilibrium (circles). Since the surface plasmon curve does not shift upon hybridisation due to the fact that the surface coverage and the molecular weight of the adsorbate are too low [85; 58] the respective curve has been omitted. When the absolute value and shape of the background fluorescence signal are compared to literature values it can be seen on the one hand that the value is rather large (approx. 30000 cps) and on the other hand that the shape shows an angular dependence, which is not reported in other surface plasmon

enhanced fluorescence measurements. Both observations are correlated in that it seems that some of the target molecules of preceding measurements remain in the high-pressure cell. Even extensive cleaning in an ultrasonic bath with temperatures up to 45 °C could only reduce this effect but not completely remove all residues. The hybridisation of the
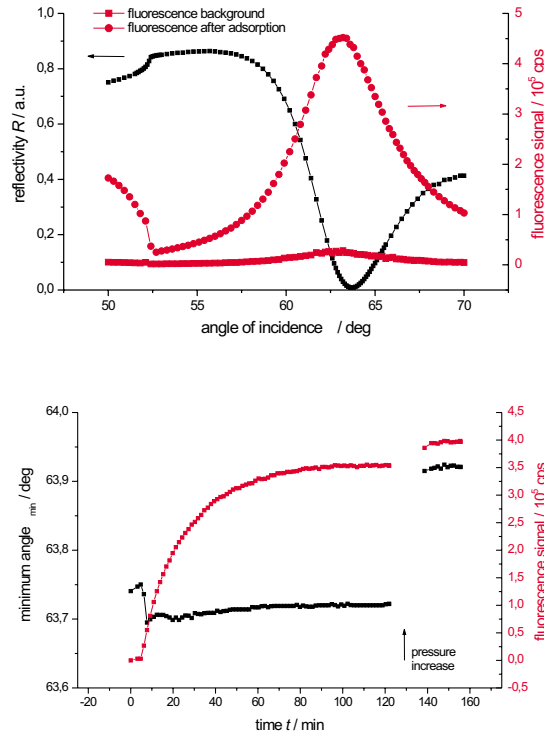
Figure 5.13: Top: Fluorescence scans of the probe layer (1 μM) prior to the injection of the 1MM target (500 nM) (squares) and after reaching of the adsorption equilibrium (circles). Also shown is the respective reference scan of the DNA probe layer. Upon adsorption no shift of the SP curve is found. Bottom: The adsorption as a function of time. Depicted are the fluorescence signal and the reflectivity.

two DNA single strands, the time dependence of which can be followed in the lower part of fig. 5.13, however leads to an more then 10-fold increase of the fluorescence signal. From the time dependent graph it can be seen that in deed the reflectivity or in this case the resonance minimum does not shift upon adsorption of the target. The fluorescence labelling enormously increases the sensitivity. After the adsorption has finished and a scan curve has been recorded the working pressure is increased to 10 MPa, which ensures

a save performance of the pressure gear. This increase of pressure can be followed in the kinetic by the shift of the surface plasmon minimum to higher angles. Along with it the fluorescence signal is increased. This effect is caused by two factors: On the one hand, with an increased density of the fluid the density of the target is increased in the medium. Consequently, the net fluorescence signal as seen by the measurement method is increased due to integration over all fluorescence markers that happen to be in the surface plasmon excitation field. This reasoning, though, has to be put into perspective as result of the measurement at even more elevated pressures (see below) . On the other hand, it might be due to a shift of the equilibrium surface coverage to higher values when the pressure is increased.
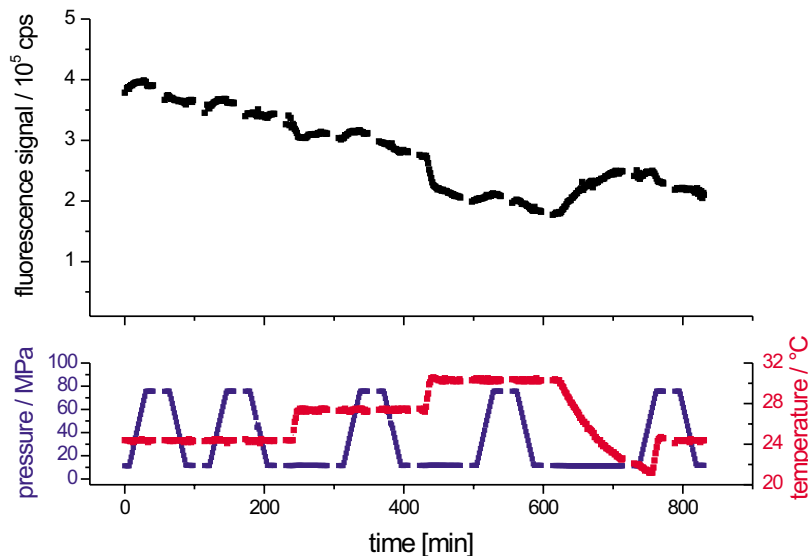
Figure 5.14: Fluorescence signal of the 1MM target as a function of temperature and pressure. The lower part of the graph shows the temperature and pressure protocol of the measurement.

Figure 5.14 shows the fluorescence of the sample as a function of time. The parameters that are varied are again temperature and pressure (cf. section 5.3.1). As in the case of the measurement of the labelled DNA probe the fluorescence intensity drops steadily with time. It is therefore assumed that some general principle has to be responsible for this behaviour. However, compared to the labelled ssDNA the total signal intensity is

roughly four times larger. This increase is contributed to the different conformations of the DNA probe in both experiments. In the former experiment the probe is a single-stranded molecule tending to form hairpins. The label is therefore closer to the surface than in the case of an erected double helix with the fluorescence marker sitting the furthest away from the surface as possible. Within the picture of the Förster transfer (cf. section 2.3) the answer to this behaviour lies within the distance of the fluorophore from the surface. The larger the distance the less emitted intensity is quenched by the metal surface. Hence, the signal of the 1MM-hybridised DNA probe has to be larger that that of the single strand. When temperature and pressure are varied the fluorescence signal again changes, showing the same general response as in the case of the labelled DNA sequence. Yet, a clear difference in the amount of signal change can be anticipated. Temperature increases lead to a larger drop of fluorescence intensity whereas the pressure effect is more suppressed.
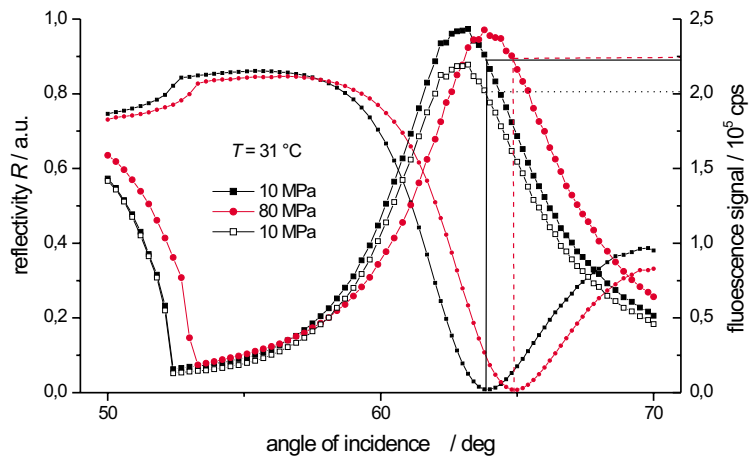
Figure 5.15: At 31 °C three different fluorescence scan curves are shown. One prior to the pressure increase from 10 MPa to 80 MPa (solid sqares), one at 80 MPa (circles), and one after decreasing the pressure again to its original value (open squares). Along with the fluorescence signal, the reflectivity is shown. The whole curve shifts to higher angles at increased pressure as the density of the system increases.

In figure 5.15 three scans at 10 MPa and 80 MPa are shown at 31 °C. This temperature is chosen as the pressure effect on the system is the largest. First of all, the surface plasmon scans reveal the requirement for the type of kinetic measurement as discussed in section

5.3.1. Here, the respective scans before, at, and after the pressure increase of 80 MPa are shown, the time position of which are represented in fig. 5.14 by gaps in the measurement curve. The kinetic measurement shows a slight increase of the fluorescence signal due to an increased hydrostatic pressure. The same change can be found in the scan curves as indicated by the lines in figure 5.15. The fact that the third fluorescence scan has a lower signal as compared to the first one at the same conditions is related to the general decrease of the fluorescence signal with time.

5.3.3 Characterisation of Mismatch Zero Hybridisation

The last experiment in this sequence comprises the hybridisation reaction of 500 nM target with its fully complementary probe sequence. Figure 5.16 presents the results of the time dependent fluorescence signal. Temperature and pressure are varied according to the experiments introduced above. Common to all measurements is the drop of signal with time. Both, 1MM and 0MM targets show an approximately 4-fold intensity as compared to the labelled DNA probe. A feature that varies from system to system is the response
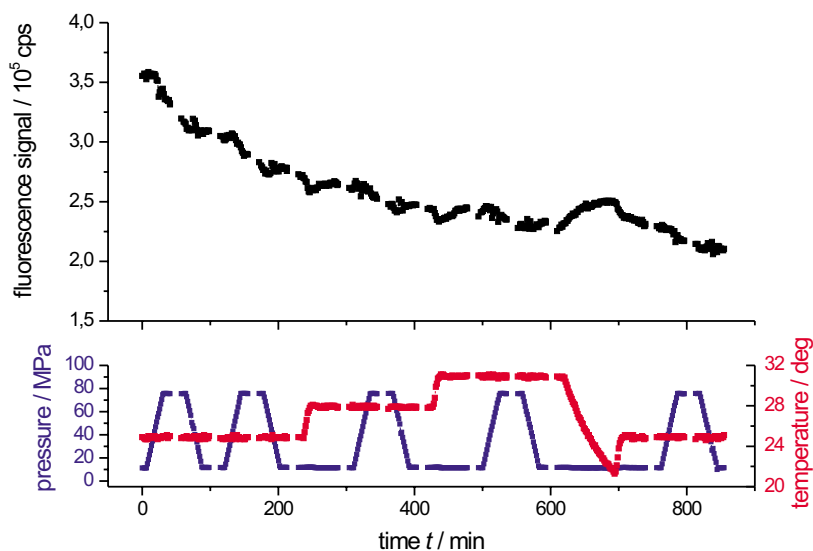
Figure 5.16: Fluorescence signal of the zero mismatch target as a function of time. The lower part of the graph depicts the temperature and pressure profile of the measurement.

to shifts in temperature and pressure, though. Compared to the 1MM situation, both thermodynamic variables show virtually no effect on the zero mismatch sample. The reason for no temperature effect is probably due to the higher melting temperature of the 0MM duplex. Since the temperature is only increased up to 31 °C no net desorption of the target occurs even though there is again an increase of the fluorescence when the temperature returns to its initial 25 °C. The same argument can be applied for the pressure sensitivity of the system. As all duplexes are closely bound and presumably all probes on the surface are saturated with target sequences the pressure variation has no net effect on the surface coverage of the target molecules.

5.3.4 Comparison of Fluorescence Measurements

The analysis and qualitative explanation of the above experiments can be carried out by using the Langmuir isotherm as described in section 2.4. At a fixed temperature T_1 the hybridisation of surface bound species results in the complete saturation of the surface following the isotherm depicted in figure 5.17 if a sufficient amount of target molecules is present. As the temperature is increased to T_2 or T_3 the dynamic equilibrium between probe and target shifts, which is expressed through changed affinity constants. The
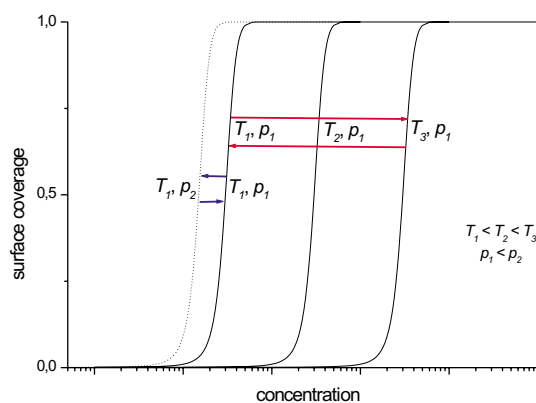
Figure 5.17: The Langmuir isotherm at different temperatures. The whole curve shifts when the temperature is changed due to changes in the affinity constant. Also indicated is an anticipated shift of the isotherm with increasing pressure.

whole isotherm shifts to higher concentrations, i.e. full surface coverage is only achieved at higher target concentrations. Since the target concentration remains fixed during an experiment increasing the temperature means that the surface coverage drops from a high value to almost zero, depending on the working concentration and temperature shift. For a fully reversible system the curve returns to its original position when the temperature is lowered again to its initial value. In the absence of any binding matrix effects the above process can be repeated over several temperature cycles and results in identical binding/dissociation during the cooling and heating steps, respectively. The
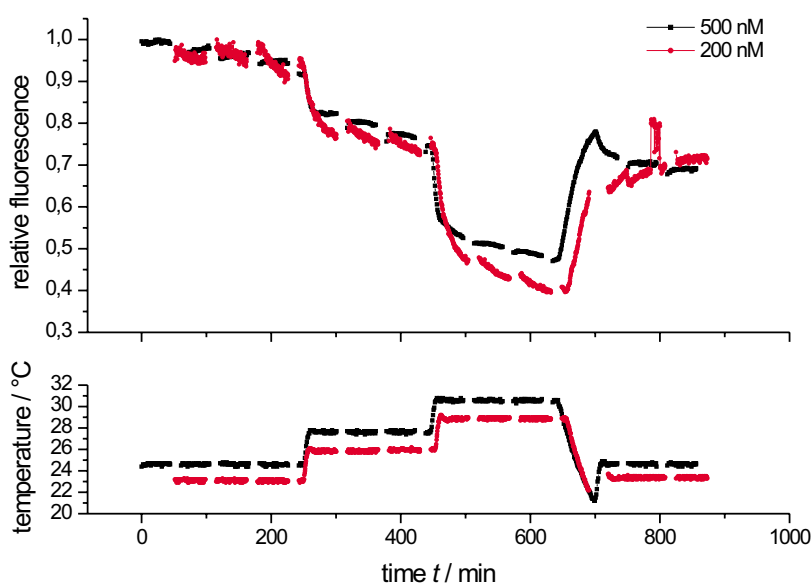
Figure 5.18: Comparison of the relative fluorescence of the one mismatch target of the concentrations 200 nM and 500 nM (on 0.5 μM and 1 μM probe layers, respectively). The temperature profile (at atmospheric pressure) is shown in the lower part of the graph.

effect of pressure can be seen from a similar viewpoint. If the pressure is increased from p_1 to p_2 and the hybridisation reaction is stabilised by pressure, an increased affinity constant moves the isotherm towards lower concentrations. At a fixed concentration the surface coverage as expressed through the fluorescence intensity is expected to rise. Also, this process should be ideally fully reversible. However, these considerations are based purely on the kinetic model. Under normal experimental conditions temperature as well

as pressure variations may have some effect on the underlying binding matrix and the stability of the immobilised probe and no full recovery of the signal might be observed.

This intrinsic instability of the system can be readily seen in figure 5.18 as well as in fig. 5.19. Figure 5.18 compares two measurements of type one mismatch at two different probe and target concentrations (200 nM target, 500 nM probe and 500 nM target, 1 μM probe, respectively). Figure 5.19 relates the kinetic curves of the labelled DNA strand and the 1MM and 0MM systems that have been presented above. As already mentioned all systems combine a loss of fluorescence intensity with time. Since the experiments cover a whole range of different material combinations including a simple fluorescent labelled DNA probe sequence immobilised at the binding matrix it is unlikely that the hybridisation itself is responsible for this behaviour. Also the probe or target concentration cannot be the reason for the decreasing signal since it is invariant to concentration changes as illustrated by fig. 5.18. Temperature or pressure could explain these findings though. Experiments carried out on the same set of materials at almost the same concentrations [145] showed that there is a steady decrease of the fluorescence signal when the temperature is steadily ramped from about 25 °C to 45 °C (close to the stability breakdown of the binding matrix) and back. It was reckoned that this temperature cycling over a period of around 2 h to 6 h decreases the stability of the binding matrix. A close look on these data reveals that the slope of fluorescence drop is about the same as found in the data presented here. Since the measurements presented here all start with a period of constant, low temperature for at least 3 h to 4 h (however at elevated pressures) it can be concluded that the decrease of the fluorescence signal does not depend on either temperature or pressure but is an intrinsic feature of the binding matrix that might desorb with time. The contradiction to the data of section 5.2.3 on the stability of the streptavidin layer at elevated temperatures and pressures can be resolved by referring to the largely increased sensitivity that is gained by the incorporation of fluorophores.

In addition to these more fundamental findings on the stability of the biotinylated thiol/streptavidin binding matrix figure 5.18 reveals some more information. First of all, an increase of temperature results in a decrease of fluorescence signal. The initial 3 °C are followed by a 15 % decrease the second 3 °C by a 20 % drop. The melting temperature for this system on the sensor surface has been reported to be approximately 35 °C [145]. Hence, it is not surprising that closer to T_m the response of the system to temperature

changes is increased. Another feature that is noteworthy is the similarity of the two curves. Despite the differences in the concentrations both measurements react similarly, yet at distinct rates. The curve with the lower concentrations responds to a higher degree to temperature jumps than the measurement with 500 nM target concentration. Moreover, this increased sensitivity takes place at an about 2 °C lower temperature. The Langmuir isotherm again helps to understand this behaviour. Both target concentrations correspond to different points within the Langmuir isotherm. The 200 nM target solution can be considered to be the concentration that results in a 50 % coverage of the probe molecules. Consequently, slight shifts of the isotherm due to temperature cause large changes of the surface coverage and, thus, of the fluorescence signal. The larger concentration in the 500 nM experiment leads to a higher surface coverage (the fluorescence signal is about 7 times larger than in the 200 nM experiment). This also means that the concentration does not necessarily sit in the middle of the isotherm anymore. The slope of the isotherm at that point is lower and the dependency of the fluorescence signal on temperature changes is therefore less pronounced. So far, the concentration of the probe molecule has not been considered in detail. Measurements carried out at constant target concentration, with 500 nM or 1 μM probe concentration reveal that the resulting fluorescence signal does not change. Hence, even a probe concentration of 500 nM seems to be already sufficient to provide full coverage of the surface, so that the influence of this concentration change can be neglected.

The responses of the systems labelled-DNA probe, one mismatch, and two mismatches (all measurements are carried out at a 1 μM probe concentration) to temperature and pressure changes are summarised in figure 5.19. In order to understand the behaviour of the three systems the molecular structure of the DNA single strand (labelled DNA) and double strands (1MM and 0MM) has to be considered. Due to this fundamental difference in the compared systems the discussion is split into a part concerned with the labelled DNA probe and another part that compares the differences of the 1MM and 0MM targets. Temperature plays in the case of ssDNA a different role that in the case of dsDNA. Since no double helix formation exists and the probe molecules are attached to the surface sufficiently far from each other to avoid crowding effects only conformational effects within the single strands can explain the experiment. Background effects like enhanced dynamic quenching of the fluorescence signal have to be excluded from this discussion as it would

be visible to the same extend in all three sets of measurements. The 1MM data shows much less temperature or pressure effect than the other two curves. Also, changes in the fluorescence label Cy5 due to temperature and pressure are not likely to influence the observed behaviour. On the one hand, measurements on other types of fluorescence labels have shown that the change in the absorption band is small [146; 147], on the other hand, again all three curves would be influenced in the same way. The conformation of the probe can be considered as being randomly bent. However, since one end of the molecule
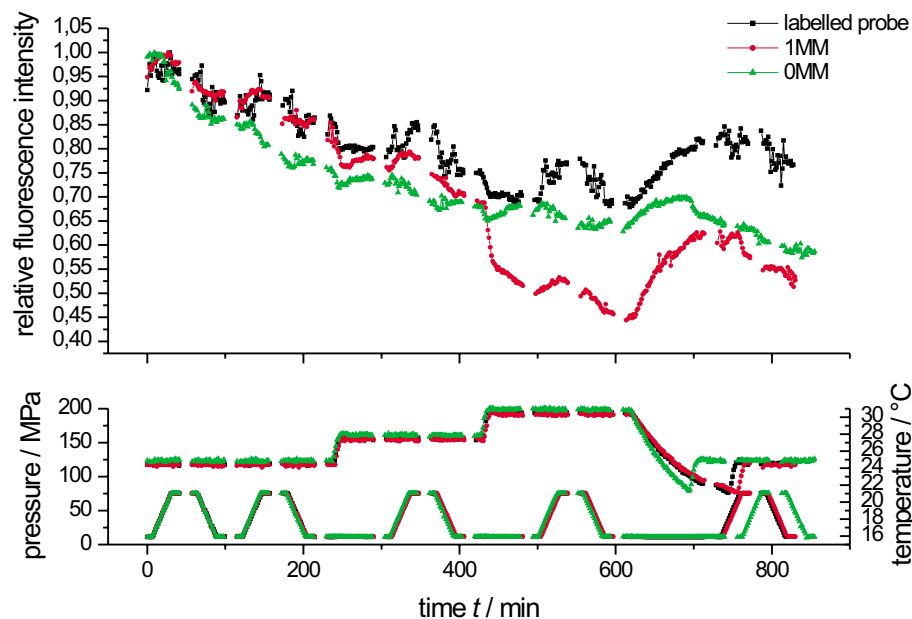
Figure 5.19: The relative fluorescence signal of the probe (squares), the 1MM (circles), and the 0MM (triangles) sequences as a function of time. The lower part of the graph depicts the temperature and pressure profile of the different measurements. As can be seen, in the last part of the kinetic the T, p protocol of the 0MM target is slightly changed with respect to the other two measurements.

is fixed to the surface and the chain length is rather small no random coil structure can be assumed. Moreover, the formation of hairpins due to self-annealing of complementary regions in the strand (cf. section 3.3.3) is suppressed at the given temperatures. (An estimation of the melting temperature of the 4 bases TTGT in the self-annealing region is 18 °C.) Consequently, the changes of temperature and pressure effect the conformation of the single strand through a changed DNA-water interaction. Moreover, as the temperature increases, the entropy of the system is increased. Hence, the mean distance of the label

from the surface is decreased and the fluorescence intensity drops due to increased Förster quenching. Temperature thus affects the conformation of the single strand. Pressure has the opposite net effect of temperature on the fluorescence intensity. It also seems that the pressure effect is virtually not dependent on the temperature. However, the increased signal at elevated pressures can additionally be induced by an increased bulk concentration. As the density increases with pressure so does the concentration of the solved DNA molecules. Thus, in the picture of the Langmuir isotherm the surface coverage is increased.

The situation is different in the case of a target sequence that is hybridised to its corresponding probe. The one mismatch target shows a pronounced temperature dependence, as has been already discussed above. An increase of pressure results in an increased fluorescence intensity. In the framework of the Langmuir isotherm the consequence of increased pressure is a shift of the curve to lower concentrations as the binding affinity is increased. Therefore, the surface coverage and along with it the fluorescence signal shifts to higher values since the bulk concentration stays constant. In fact, the bulk concentration increases with pressure as well, which additionally promotes an increased surface coverage of hybridised species. The interaction of temperature and pressure gives rise to another effect. The system reacts to pressure more pronounced at higher temperatures. As already assumed above, at the concentration of 500 nM target the surface is already highly covered by duplexes. Temperature reduces the surface coverage and shifts the isotherm such that the working point is closer to the concentration with 50 % surface coverage. Consequently, the slope of the isotherm is steeper and small shifts of the isotherm induced by pressure variation results in a more pronounced change of fluorescence signal. In principle, this discussion is also valid for the zero mismatch system. However, the affinity of both ssDNA to each other is higher as compared to the 1MM case. Therefore, a 500 nM target concentration completely covers the surface. As a consequence, temperature or pressure do not influence the saturated surface coverage. This behaviour can be seen in fig. 5.19 where little response to temperature but no pressure effects can be observed.

5.4 Conclusion

In this section it is shown that high-pressure surface plasmon enhanced fluorescence spectroscopy is an appropriate tool to study DNA hybridisation reactions where the target is immobilised at a surface. The supramolecular binding matrix used to fix the target consists of a thiol and a streptavidin layer that are both tested for their stability.

The self-assembled biotinylated/OH-terminated thiol layer is neither destabilised by pressure nor by temperature. The surface plasmon angular scans solely reflect the change of the density of the pressure medium when both parameters are varied. When the minimum position of the resonance curve at 0 MPa (extracted from minimum versus pressure plots) is graphed as a function of temperature a steady decrease is observed indicating that the layer is stable in the applied temperature (20 °C to 55°C) and pressure (10 MPa to 200 MPa) ranges.

The same measurement protocol applied to the subsequent streptavidin layer resulted in different results. Pressure has no apparent effect on the layer stability whereas temperatures above 45 °C to 50°C effectively destabilise the biotin/streptavidin binding. These temperature values, though, are about 5 °C larger than reported in literature, which is an indication that pressure inhibits the desorption process of the protein at high temperatures.

In another set of experiments, fluorescent labelled DNA probe molecules are injected into the high-pressure cell to bind to the streptavidin layer. In the kinetic measurement mode a complex temperature and pressure protocol triggers the response of the target layer. The signal slightly decreases with temperature and increases with pressure. As the target is a single strand oligonucleotide a random coil-like conformation is assumed to explain the results. In the case of temperature, entropic effects can result in a more compact conformation of the single strand. Moreover, the solute-solvent interactions that change when temperature and pressure are varied also seem to influence the conformation. Furthermore, the increased density of fluorophores near the surface at elevated pressures may influence the signal change as the absolute value of the recorded fluorescence intensity is comparatively low. The general decrease of the fluorescence signal with time can be attributed to the intrinsic instability of the binding matrix. This behaviour, which is not found in the normal surface plasmon spectroscopy studies discussed above due to the

lower sensitivity, is common to all fluorescence measurements to a similar extend and also found in literature.

Kinetic studies of the hybridisation of a labelled one mismatch target and a corresponding unlabelled probe sequence show in principle the same behaviour as the probe molecule alone. However, here the conformation of the DNA is a double helix. The much more pronounced temperature dependence of this system is explained with the melting temperature of the double helix. In terms of the Langmuir picture the isotherm shifts to higher concentrations and the surface coverage decreases. Pressure stabilises the helix formation, which is coupled to a negative volume change, and the fluorescence intensity therefore increases. The larger effect at increased temperature is also explained in the Langmuir framework.

A zero mismatch target shows little response to the same pressure and temperature variation protocol. Since its melting temperature is much higher than in the one mismatch case the affinity between both single strands is extremely enhanced. Therefore the small temperature changes do not affect the stability of the duplex very much. Similarly pressure has no significant influence and no response of the system is detectable.

6. PMMA/MMA in Supercritical Carbon Dioxide

The interest in exploiting supercritical fluids as an ecological alternative to conventional solvents has increased in recent years. Due to its unique properties as solvent and transport medium some special applications have become feasible [148; 88; 149]. Supercritical fluid extraction [88; 150] and polymerisation reactions [91] have even been realised technically [151].

Along these lines, the thermodynamic behaviour of glassy polymer-gas systems is of general interest. The excellent solving characteristics of compressed gasses can lead to extensive swelling [8; 152; 153] and significant lowering of the glass transition temperatures [101; 9; 102]. References about the sorption and swelling behaviour of polymers in CO_2 can readily be found in the literature [8; 152; 154; 155; 156; 157; 158]. Most studies, however, have been carried out at low or moderate pressures [154; 155; 156; 157; 158].

The industrial application of e.g. polymerisation reactions requires the knowledge of material parameters at elevated temperatures and pressures. Recently, dispersion polymerisations have been studied by utilising light scattering methods [159; 160; 161]. The refractive indices of the polymer swollen by the respective monomer have in these cases been extrapolated. Precise measurements of the refractive indices of polymer/monomer systems however are the necessary prerequisite for the evaluation of turbidimetric data that have been used to elucidate the kinetics of polymerisation of MMA in sc-CO_2 [161].

The techniques used in the past to determine the swelling behaviour of polymers are either based on visual inspection [162] or electrical resistance measurements [163]. Here, an optical method fits in extremely well to simultaneously quantify the swelling of, in this case, a thin polymer film and the refractive indices of the solvent and the polymer.

The characterisation of thin PMMA films in contact with (fluid) CO_2 or CO_2/MMA

mixtures in this section is accomplished by means of waveguide spectroscopy. At first, the refractive index of carbon dioxide as a function of pressure is compared to literature data in order to validate the SPR/waveguide mode technique in this context. The refractive indices of the solvent and the swollen polymer are presented thereafter and compared to calculations based on an ideal mixture. A third part concerns the influence of pressure and MMA monomer concentration on the swelling behaviour of the polymer.

6.1   Refractive Index of Carbon Dioxide

At first the performance of the apparatus is examined by measuring the refractive index of supercritical carbon dioxide at pressures up to 200 MPa. For this system there exists a good set of experimental data [35; 36] to which the presented results can be compared. Fig. 6.1 shows the data of the refractive index of CO_2 as a function of pressure at 41 °C, 51 °C, and 62 °C. Initially, the refractive index increases rapidly with increasing pressure and then, from about 20 MPa - 30 MPa, somewhat slower.   This behaviour can be
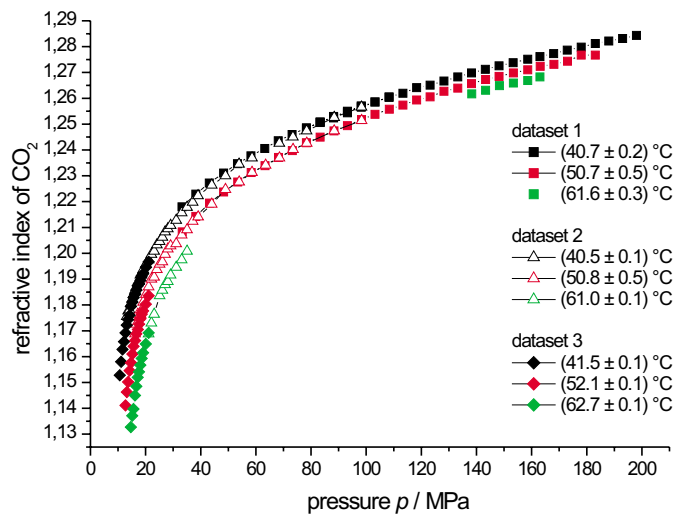
Figure 6.1: Refractive index of CO_2 versus pressure. The refractive index is measured on a few different samples that are especially prepared for the refractive index region of carbon dioxide. For the measurements at high pressures the grating constant is optimised for $n = 1.2$, the lower pressure data are recorded with gratings suitable from approx. $n = 1.15$ onward.

explained by the increase of density with increasing pressure. The refractive indices of the solvent decreases with increasing temperature. This is again contributed to a density change, this time caused by the change of temperature.
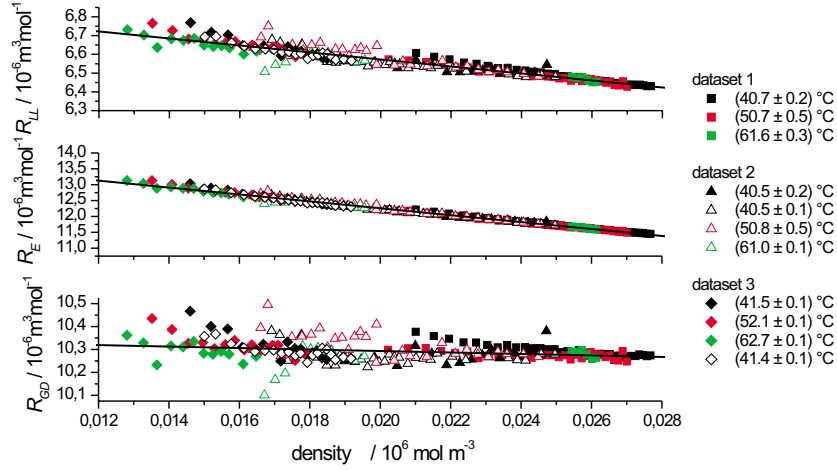
Figure 6.2: Comparison of the refractive index of CO_2 evaluated in terms of the refractivities according to Lorentz-Lorenz R_{LL}, Eykman R_E, and Gladstone-Dale R_{GD} as a function of density. The solid lines are linear fits to the respective data.

As explained in section 2.2.1 the theoretical description of this data is usually carried out by using either the Lorentz-Lorenz equation (2.51) or one of the other equations that link the refractive index with the density of the system. Sometimes the commonly used Lorenz-Lorentz relation (2.51) does not fit the experimentally determined refractivities well. Instead of being a constant when plotted versus the density the refractivity R_{LL} shows a distinct slope of $(-0.424 \pm 0.010)10^{-6}\text{m}^3\text{mol}^{-1}$. The densities to the respective temperature and pressure data are extracted from the Span-Wagner equation of state and the IUPAC tables [164]. Figure 6.2 compares the three different semi-empirical refractivity equations given in section 2.2.1, namely the Lorentz-Lorenz (2.51), the Gladstone-Dale (2.52), and the Eykman (2.53) equations. Out of these three equations clearly the Gladstone-Dale equation gives the best results. The slope of R_{GD} is $(-0.073 \pm 0.016)10^{-6}\text{m}^3\text{mol}^{-1}$ and its assumed constant refractivity at a laser wavelength of $\lambda = 632.8$ nm is $R_{GD}(632.8\,\text{nm}) = (0.234 \pm 0.001)10^{-6}\text{m}^3\text{mol}^{-1}$.

Nevertheless, there is another way to describe the data; a virial expansion of the Lorentz-Lorenz equation (2.51) [35; 36] as given by equation (2.54) accounts for the deviations of the refractive index of CO_2 from the Lorentz-Lorenz equation. Figure 6.3 depicts the refractive index of CO_2 as a function of density. Clearly, the differences in refractive index due to different temperatures that are still apparent in fig. 6.1 have vanished since pressure and temperature have been merged to density values. This curve is readily fitted using eqn. (2.54). The values of the fit are summarised together with some literature values in table 6.1.
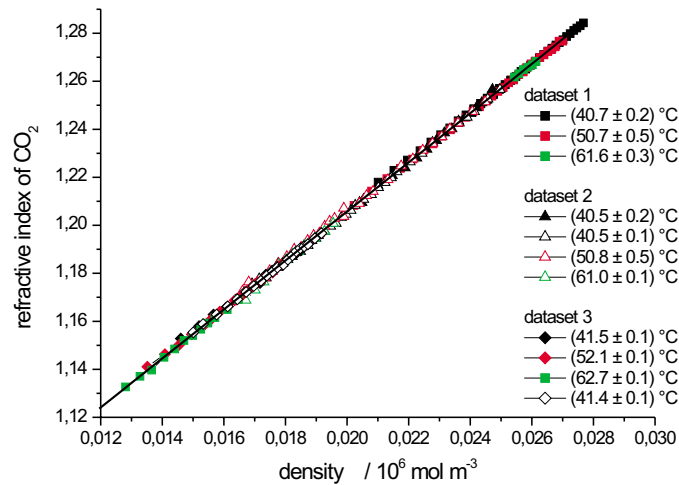
Figure 6.3: The refractive index of carbon dioxide at different densities. The solid line represents a fit using the virial expansion (2.54) of the Lorentz-Lorenz equation.

If all three virial coefficients are fitted to the measured data drastic deviations from the literature values have to be acknowledged. The second and third virial coefficient even have changed signs. To explain these deviations the assumptions that the presented data is based on and possible errors in the data treatment have to be emphasised: Firstly, the grating might not be exactly sinusoidal as anticipated. Secondly, the simple treatment of the grating in the evaluation method leaves some space for improvement. The full theory of gratings should be applied instead. Thirdly, the grating spacing, which is measured in the Littrow configuration and which has a great impact on the converted data, which is evaluated with the transfer-matrix method, has a certain error. Finally,

A_R $10^{-6}\mathrm{m^3mol^{-1}}$	B_R $10^{-12}\mathrm{m^6mol^{-2}}$	C_R $10^{-18}\mathrm{m^9mol^{-3}}$	reference
7.005 ± 0.052	-24.7 ± 4.9	147.4 ± 113.8	
6.634 ± 0.002	1.9 ± 0	-287 ± 0	B_R, C_R from literature
6.600	1.25	-264	Michels [165]
6.644	1.9 ± 0.2	-287	Achtermann [35]
6.649 ± 0.015	1.9 ± 0.2	-287	Obriot [36]
6.687	1.21	-	Kholodov [166]
6.658	3.3 ± 3.6	-287 ± 8	St.-Arnaud [167]

Table 6.1: Virial coefficients of carbon dioxide.

the recorded pressure and temperature are flawed with error (c.f. section 3.1.1.2) resulting in an incorrect conversion into density data. these factors influence the exact evaluation of the data presented in figure 6.3, thus, leading to deviations of the virial coefficients from literature. However, if the second and third virial coefficient are kept constant at literature values (as, for instance, has been done in the data treatment of Obriot et. al [36] as well) a value of $(6.634 \pm 0.002)10^{-6}\mathrm{m^3mol^{-1}}$ is found for A_R. This value is in good agreement with the values reported in literature. Some more care might have to be taken though in order to get reasonable values for the second and third virial coefficients. It is however a difficult task to retrieve the second and third coefficient from the data as their influence on the refractive index is extremely small. In general, scatter of the data and fundamental assumptions in the evaluation methods might easily account for large errors in B_R and C_R.

6.2 Polymer/Monomer Interaction in Supercritical Carbon Dioxide

The calculations presented in this section assume an ideal mixture, i.e. the volumes of the individual components add up to the total volume neglecting any volume change upon mixing. Therefore the Lorenz-Lorentz mixing rule as expressed through eqn. (2.57) can be applied. The refractive index of carbon dioxide is calculated by extrapolation of the refractivities of CO_2 as given by Obriot et al. [36]. The densities needed for this

calculation are obtained from the Span-Wagner equation of state and the IUPAC tables [164] at the specific pressures and temperatures. The refractive index of distilled MMA is measured with an Abbé refractometer at $\lambda = 587$ nm, $T = 20$ °C, and atmospheric pressure and is subsequently converted to a wavelength of 632 nm according to Li et al. [168]: n(MMA, 633 nm, 20 °C) = 1.414. The density of methylmethacrylate is taken from the literature to be ρ(MMA) = 0.944 gcm^{-3} [128]. With these parameters and eqn. (2.51) the Lorenz-Lorentz constant for MMA can be determined to be R_{LL}(MMA) = 0.265 cm^{3}g^{-1}. The thermal expansion coefficient and the isothermal compressibility of methylmethacrylate at the appropriate conditions are taken from Galland et al. [169] and Sasuga and Takehisa [170]. Also, for poly(methylmethacrylate) the refractive index, density, isobaric thermal expansion coefficient and isothermal compression are adopted from literature [128; 171; 172; 56]. Any contribution of the small amount of added inhibitor hydroquinonemonomethylether is neglected. Concerning the ternary mixture CO_2/MMA/PMMA, a pressure independent distribution ratio of 1 with regard to volume is assumed for MMA in CO_2 and PMMA. Within the context of an ideal mixture and without the knowledge of the MMA content in PMMA this assumption ensured the feasibility of the calculations. In order to obtain the volume fraction of carbon dioxide in the polymer the specific density of CO_2 solved in polymethylmethacrylate is estimated to be 44 cm^{3}mol^{-1} [100; 153]. Finally, the measured swelling of PMMA due to CO_2, as shown below, is taken into consideration in the calculations. Although the MMA concentration in solution is decreased by its absorption into the PMMA film, this effect is ignored because of the negligible PMMA/solution volume ratio.

In the following, measurements of the refractive indices of CO_2, CO_2/MMA and CO_2/MMA/PMMA mixtures and the swelling of a PMMA film in pure carbon dioxide and MMA/CO_2 mixtures are presented. All measurements are conducted at a constant temperature of 60 °C.

6.2.1 Refractive Index of Pressure Medium

After the verification of the measurement system the MMA content of the solution is varied in order to gain some information about the swelling behaviour of the PMMA film in its monomer. 0.5, 1.0 and 1.5 molar solutions of MMA in CO_2 are tested. As shown

in fig. 6.4 the higher the MMA concentration the higher is the pressure at the first data point. At 1.5 mol/l the data around 20 MPa are extremely noisy. These observations are explained by the solubility of methylmethacrylate in CO_2, which depends on the
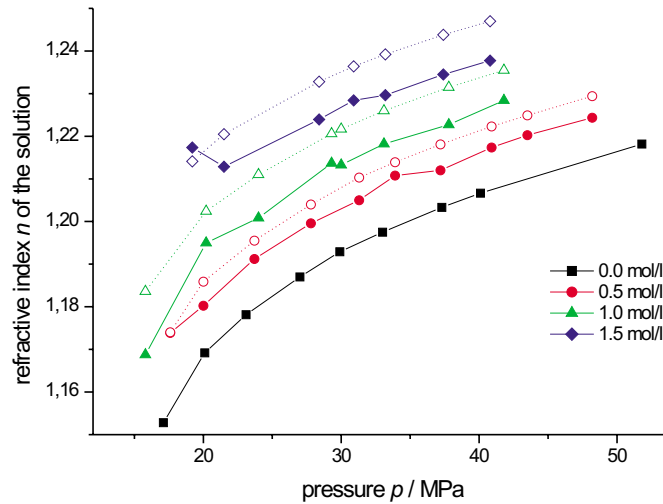
Figure 6.4: The refractive index of 0, 0.5, 1.0, 1.5 molar MMA solved in CO_2 versus pressure indicated by squares, circles, triangles, and diamonds, respectively. The calculated refractive indices corresponding to the particular measurement conditions are represented by the corresponding open symbols and connected with dotted lines for clarity.

MMA concentration, temperature and pressure [161; 92]. At pressures below 16 MPa all MMA/CO_2 mixtures are of heterogeneous nature. The increasing density of the fluids again induces the increasing refractive index with pressure. Moreover, with increasing MMA content the refractive index of the mixture rises. This phenomenon is explained by the higher fraction of MMA in solution, which has a larger refractive index compared to carbon dioxide. The calculated refractive indices are depicted in fig. 6.4 as open symbols, respectively. Clearly, all calculated data are larger than their corresponding experimental data points. However, the qualitative trend of the measurements is reproduced correctly, in that the displacement between both curves remains the same throughout the whole pressure range. The origin of the displacement itself stays unexplained but can presumably be found in the crude assumptions made at the derivation of the calculations.

6.2.2 Refractive Index of PMMA-MMA Mixtures

The following two sections focus on the characterisation of the PMMA film. Firstly, the pressure and MMA molarity dependent change in refractive index is examined. Secondly, attention is drawn to the swelling characteristics of the film as a function of the above mentioned parameters. In fig. 6.5 the refractive index of the MMA/CO_2-swollen PMMA film is plotted against pressure. Two features are noteworthy. First, with increasing pressure the refractive index of the layer decreases due to the pressure-induced increase of the MMA/CO_2 content in the film; both, MMA and CO_2 have a lower refractive index than the polymer. Second, with increasing MMA concentration the refractive index of the film decreases. This behavior is induced by the swelling ability of MMA with respect to PMMA (see section 6.2.3). The higher the MMA content, the more swollen the PMMA film, the higher the MMA/CO_2 fraction in the film and, thus, the lower the apparent refractive index of the polymer.
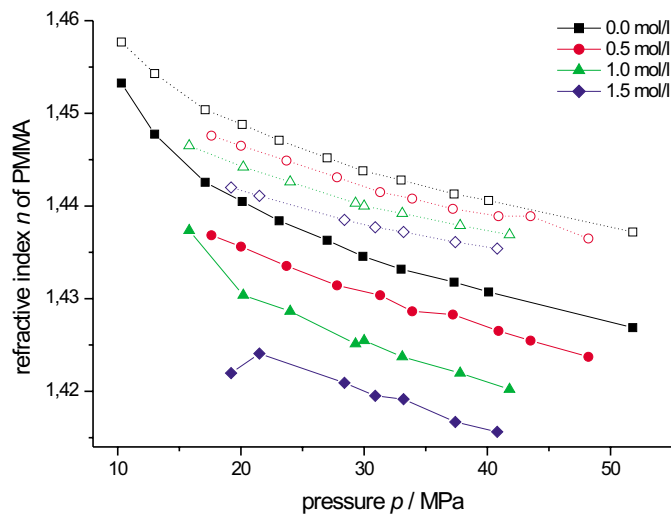
Figure 6.5: The refractive index of the swollen PMMA film plotted against pressure for different MMA concentrations (diamond, 1.5 M; triangle, 1.0 M; circle, 0.5 M; square, 0 M MMA content in CO_2). The calculated refractive indices corresponding to the particular measurement conditions are represented by the respective open symbols and connected with dotted lines.

Focusing on the calculated values marked by the respective open symbols, one can see the

qualitative conformity with the measured data in that the refractive indices decrease with pressure and MMA concentration. However, in this case the slopes of the curves deviate from the measured ones. A smaller dependence on the pressure is predicted. Also, with increasing MMA molarity the calculated values diverge to a much larger extent. It is clear that especially for high methylmethacrylate concentrations the assumption of an ideal mixture is no longer valid. The smaller slope of the calculated curves can be explained by an extended MMA content in the polymer film with increasing pressure (as compared to the constant volume fraction that is assumed in the calculations).

6.2.3 Swelling of Polymer Film

Waveguide spectroscopy yields, besides the refractive indices of the superstrate and the dielectric film, the thickness d of this layer, provided that at least two resonances are excited. Fig. 6.6 shows the measured thickness dependence of the polymer film on pressure. Clearly, the thickness increases, at first, rapidly and then, from about 17 MPa
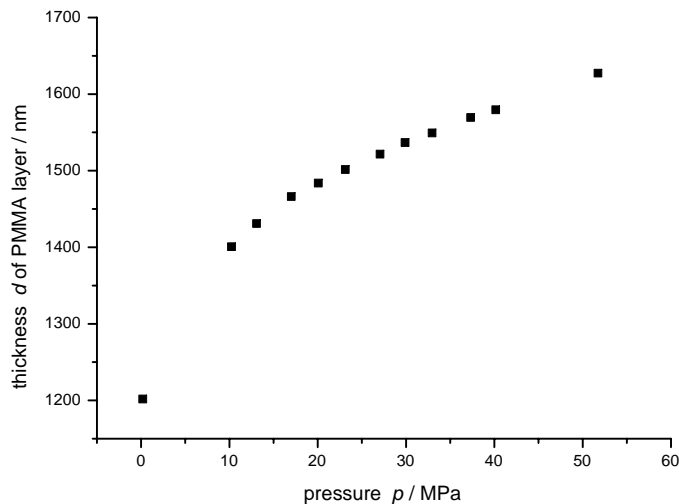
Figure 6.6: The absolute thickness of a PMMA layer versus pressure.

on, slower. The comparison to data measured against water as pressure medium reveals the hydrophobic property of PMMA[56]. Kleideiter et al. found a decreasing thickness (and an increasing refractive index in contrast to the data presented above) with increasing pressure. Since, in a first approximation, no water is solved in the polymer it is simply

compressed by the water. Using CO_2 as pressure medium the presented measurements demonstrate the sorption of CO_2 and therefore the swelling of the PMMA film.
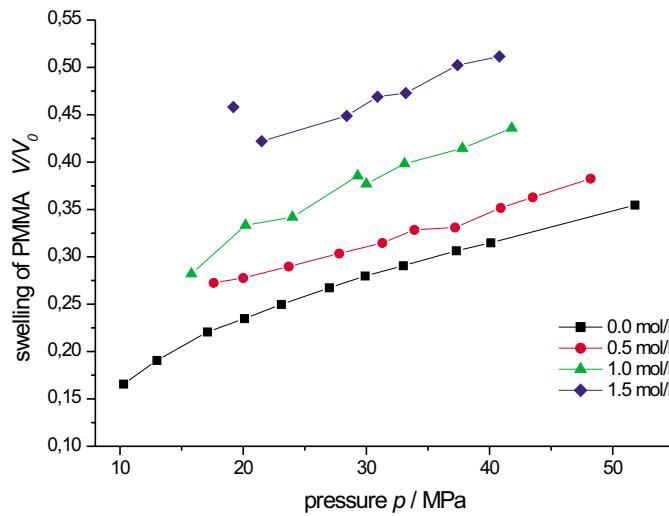
Figure 6.7: The swelling of the PMMA layer versus pressure for varying MMA concentrations (diamond, 1.5 M; triangle, 1.0 M; circle, 0.5 M; square, 0 M MMA content in CO_2). The swelling is determined from the thickness variation by assuming that a thickness change corresponds to a change of volume (see explanations in the text).

In this work, the PMMA film cannot expand in the plane of the surface but only in thickness. The assumption on which the following discussion is based is that the volume change of the film is proportional to the thickness change since the polymethylmethacrylate used is neither cross-linked nor unisotropic. The strain built up inside the sample is assumed to relax. Thus, the swelling describes the volume change ΔV of the polymer related to the initial volume V_0 and is based on the thickness change d - d_0, with d_0 being determined prior to every measurement incorporating a new sample.

As can be seen in fig. 6.7, the swelling of the PMMA film in the different MMA/CO_2 solvents increases with pressure. It also increases with increasing MMA content, resulting in an overall reverse behaviour compared to the one of the refractive index of fig. 6.5. The way the refractive index behaviour is explained in the subsection above is based on fig. 6.7, which illustrates an increased swelling of the polymer due to a higher concentration of MMA.

In the literature there already exist some studies on the sorption and swelling behaviour of PMMA in CO_2. Liau and McHugh, for example, found by visual inspection that PMMA increasingly absorbs CO_2 as a function of pressure, which, in turn, results in an increased volume of the polymer [152]. The comparison of the swelling results of Liau and McHugh with the data presented here (fig. 6.8) shows extremely large deviations. However, Paulatis and Wissinger have already noted that the visual determination of the swelling behaviour may be accompanied by large errors [8]. In addition, different sample
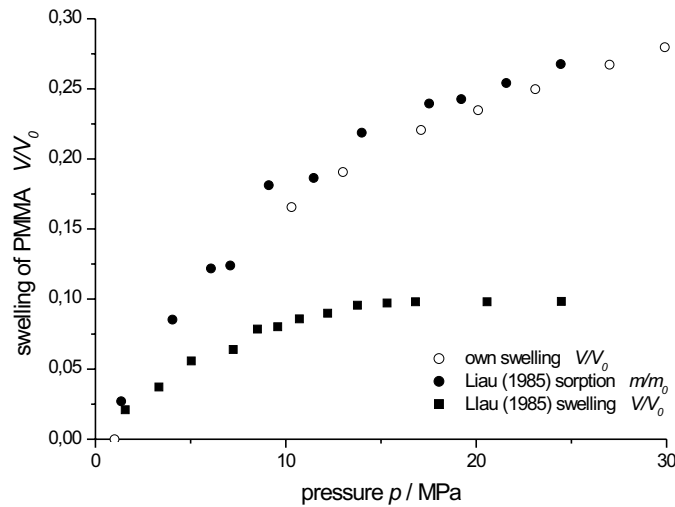
Figure 6.8: Comparison of the experimental swelling data (CO_2 swollen PMMA at $T = 59.8$ °C) with literature values (Liau and McHugh, 1985 [152]) determined at 58.1 °C. A correspondence between the swelling data and the sorption data of Liau et al. can be observed.

formats have been used. Nevertheless, the sorption data of Liau and McHugh correspond very well with the swelling behaviour of the measurements presented. While surprising at first, this correlation becomes more reasonable when taking into account that the partial specific volume of CO_2 in PMMA stays virtually constant at pressures above 7 MPa [100]. Thus, in the pressure range under investigation the volume change is proportional to the mass and therefore to the sorption change.

6.3   Conclusion

The refractive index of pure CO_2 corresponds well to prior measurements [36] and can be modelled with a virial expansion of the Lorenz-Lorentz equation. If only the first virial coefficient is fitted with the 2nd and 3rd coefficient kept constant assuming literature values good agreement with literature can be found. However, when the first three coefficients are varied deviations from literature values arise presumably due to accumulated errors.

Furthermore, it is shown that thin polymer films with supercritical carbon dioxide as solvent can be characterised using waveguide spectroscopy. The results suggest the possibility that even thinner films with no waveguide modes present might readily be characterised and that sorption experiments in a supercritical fluid environment can be realised by means of surface plasmon spectroscopy.

The study of a spin-cast PMMA film at the interface with CO_2 and CO_2/MMA mixtures has given the following results:

Firstly, quantitative deviations of up to 1.5 % arise when the experimental refractive indices of the three component system CO_2/MMA/PMMA are compared to those calculated by means of the Lorentz-Lorenz mixing rule for ideal mixtures. Yet, the qualitative behaviour of the experimentally determined refractive indices is reproduced correctly.

Secondly, the thickness of the polymer film rises with increasing pressure and MMA concentration in the fluid. A higher percentage of solvent is absorbed and the refractive index of the film decreases hereupon.

Thirdly, the swelling behaviour of PMMA due to sorption of CO_2 clearly deviates from other studies [152]. The waveguide spectroscopy, though, as an optical method, seems to be a more accurate method than visual inspection alone.

In conclusion, the refractive indices of the presented solvent mixtures cannot be simply described by an ideal mixture at the given conditions. Rather, it is necessary to complement experimental measurements of refractive indices with suitable theoretical models.

7. Cyclic Voltammetry

In the previous chapters surface plasmon spectroscopy at elevated pressures is used to characterise the optical properties of thin films. This chapter goes one step further in that high-pressure surface-plasmon spectroscopy is combined with electrochemistry. The results of two systems that are measured in a newly constructed cell that provides the facilities for both measurement techniques are presented. After an introduction to cyclic voltammetry (CV) at elevated pressures the well-studied system potassium hexacyanoferrate(III)-(II) is introduced to establish the electrochemical reliability of the cell. As an example of the combination SPR-CV the electro-polymerisation of thiophene at elevated pressures is presented thereafter.

7.1 Electrochemistry at Elevated Pressures

Experiments at high pressure provide information about the activation and reaction volumes that accompany physicochemical processes. Thus, reaction mechanisms governed by a solute and/or solute-solvent interaction can be better understood. As a consequence, many common techniques such as nuclear magnetic resonance [173], spectrophotometry [174], or surface plasmon spectroscopy [56] have been adapted to high-pressure measurements. There are also some studies that have exploited electrochemical techniques to study reactions at high pressures [175; 176; 177; 178; 179]. When using electrochemical methods the thermodynamic and kinetic aspects of a wide range of redox reactions can be investigated. Amongst these are formal redox potentials, electron transfer rates, ion-solvent interactions, and diffusion properties.

As already mentioned in section 5.1 the formation of charged species in solution is accompanied by electrostriction. These changes in the solvation energy will affect the standard potential E^0, which is in the case of a reversible redox relation (2.78) related to the peak

potential E_p of a cyclic voltammogram by [178]

$$E^0 = E_p + \frac{RT}{nF} \ln \left[\frac{a_{Red}D_{Ox}}{a_{Ox}D_{Red}} \right] + \frac{0.029}{n}, \tag{7.1}$$

where D_{Ox}, D_{Red} are the diffusion coefficients and a_{Ox}, a_{Red} are the activity coefficients of the oxidised and reduced species, respectively. T is the temperature, R the gas constant, F the Faraday constant, and n the number of electrons transferred in the reaction. From thermodynamics the change of free energy ΔG^0 of a reaction is related to the standard reaction volume ΔV^0 by

$$\left(\frac{\partial \Delta G^0}{\partial p} \right)_T = \Delta V^0. \tag{7.2}$$

With the equation

$$\Delta G^0 = -nF \cdot \Delta E^0 \tag{7.3}$$

the standard reaction volume can be expressed through the standard potential. If the ratios of the diffusion and activity coefficients are assumed to remain constant in the investigated pressure region this equation simplifies to [178]

$$\Delta E_p = -\frac{\Delta V^0}{nF} \Delta p, \tag{7.4}$$

where the peak potentials are easily extracted from the measured cyclic voltammograms. From a practical point of view, it is extremely important for the interpretation of experimental results in terms of reaction volumes to know about the pressure dependence of the potential of the reference electrode. For an Ag/AgCl reference electrode Cruañes et al. [177] reasoned that at least in the pressure range below 300 MPa the potential may be considered constant.

The diffusion coefficient of a reactant as a function of pressure can be determined from the slopes of the peak current versus the square root of the sweep rate. The Randles-Ševčik equation (2.82) links these two quantities, however the area of the working electrode and the bulk concentration of the reactant that are both depending on the pressure are also variables in this equation. For a solid disk electrode the pressure dependence is negligible; as for the concentration, extra measurements are required or appropriate assumptions have to be made.

7.2 Potassium Hexacyanoferrate(III)-(II)

The potassium hexacyanoferrate(III)-(II) redox couple has been extensively studied at all kinds of electrodes [180; 181; 182] including solid electrodes at elevated pressures [176; 179]. For this reason it has been chosen to test the high-pressure cyclic voltammetry cell.
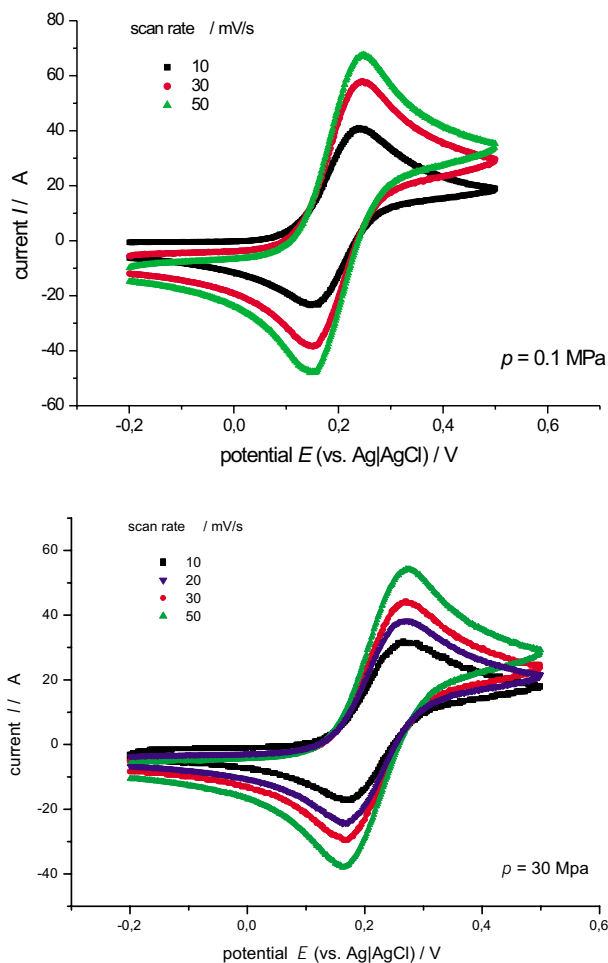
Figure 7.1: Cyclic voltammograms of the potassium hexacyanoferrate(III)-(II) system at 0.1 MPa and 30 MPa. The scan rate ν is varied from 10 mV/s to 50 mV/s.

Figure 7.1 shows the cyclic voltammograms of a 0.1 M KCl, 2 mM $K_3Fe(CN)_6$, and 2 mM $K_4Fe(CN)_6$ aqueous solution recorded at various sweep rates ν from 10 mV/s to 50 mV/s at 0.1 MPa and 30 MPa. As expected for the reaction

$$Fe(CN)_6^{3-} + e^- \rightleftharpoons Fe(CN)_6^{4-} \tag{7.5}$$
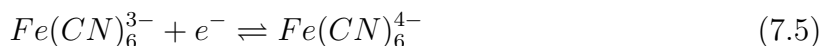
reversible voltammograms can be recorded in the potential range from -0.2 V to 0.6 V. The voltammograms show a half-way potential of 198 mV vs. Ag/AgCl and a quasi-reversible behaviour, the peak separation being about 100 mV. In comparison to 59 mV in the reversible case this value is quite high. However, one has to consider that 59 mV is an ideal value, difficult to achieve depending on the electrode preparation [183]. In the case of the presented data a poly-crystalline gold film is thermally evaporated onto a surface grating. Both of these conditions are not in favour of an ideal electrode surface. In order to further test the reversibility of the system the sweep rate is varied at constant pressure. According to the theory of reversible reactions (the charge transfer is fast compared to the mass transport, cf. section 2.5) the peak current has to be a linear function of the square root of the sweep. The increase in the peak current with ν can be explained by referring to the time elapsed while sweeping through the oxidation or reduction peak. The general trend that the peak current is increasing with sweep rate can easily be seen in fig. 7.1.
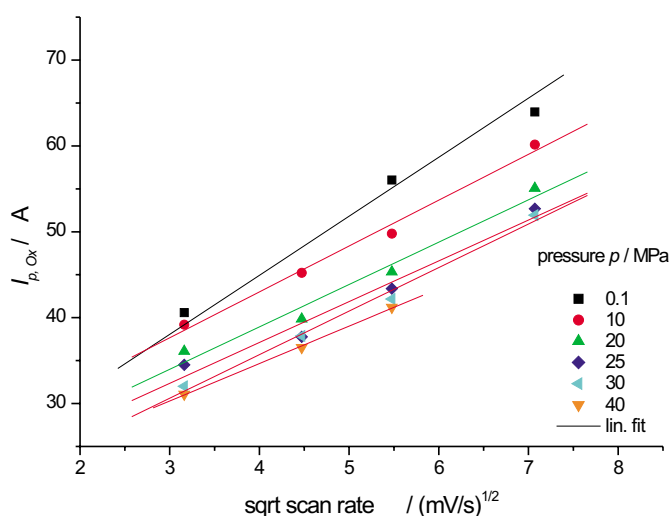
Figure 7.2: Oxidation peak current versus square root of the scan rate at different pressures. The solid lines are linear fits to the data at the respective pressures.

Figure 7.2 demonstrates that the peak current indeed follows the Randles- Ševčik equation. The current $I_{p,Ox}$ (as well as $I_{p,Red}$, not shown), which is plotted as a function of the square root of ν, can be fitted by a linear function. Figure 7.1 shows data found with

and without pressure applied. Interestingly, the peak current decreases with increasing pressure. Since the surface area of the electrode remains constant (the compressibility of gold is rather low) and the number of transferred charges stays the same the only parameters that change with pressure are the diffusion coefficient and the bulk concentration of the reactant. Therefore, in the simple picture that complex-formation is not enhanced at elevated pressures the change of the slope of $I_p(\nu)$ has to result from the interaction of the diffusion coefficient and the bulk concentration. The former decreases, the latter increases with pressure.

The decrease of the peak current with pressure can also be seen in figure 7.3, which compares the cyclic voltammograms taken at a set of different pressures and a sweep rate of 10 mV/s. In addition to the effect of the diffusion coefficient and concentration the whole curves shift to higher potentials as the pressure is increased.
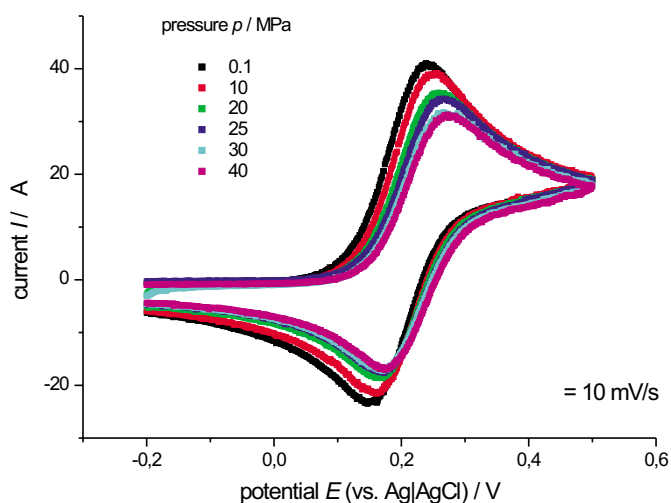
Figure 7.3: Comparison of the cyclic voltammograms at different pressures. The scan rate is 10 mV/s.

This shift of about 30 mV/s in the half-way potential is depicted in the top panel of figure 7.4. The molar volume change ΔV^0 calculated from the slope of this plot is (-63.4 $\pm$ 5.9) cm^{3}mol^{-1}. The comparison with literature ((-41.9 $\pm$ 0.6) cm^{3}mol^{-1} [179]) shows that the presented molar volume change is approximately 50 % larger than the reported one. Moreover, ΔV^0 can also be calculated from solution thermodynamic measurements if the

appropriate values are available. The partial molar volumes for potassium ferrocyanide (95.6 cm^{3}mol^{-1}), potassium ferricyanide (137.0 cm^{3}mol^{-1}), and an electron (3 cm^{3}mol^{-1}) [176] give together with the molar volume of silver a value of -44.4 cm^{3}mol^{-1} for reaction (7.5). However, the comparison to the calculated values has to be unreliable due to the fact that the thermodynamic method uses partial molal volumes at infinite dilution whereas the cyclic voltammetry experiment involves highly charged ions at a high concentration of supporting electrolyte. It can be assumed that there will be extensive ion association between the highly charged iron complex ions and cations present. The discrepancy between the two experimental values might arise from the different preparation procedures of the working electrodes. Sachinidis et al. used a flat 1 mm disk electrode, which is cleaned with emery paper and polished with high purity alumina particles, whereas here a 5 mm^2 electrode is thermally evaporated onto a surface grating and used without further cleaning. Possible side effects due to this procedure cannot be ruled out.
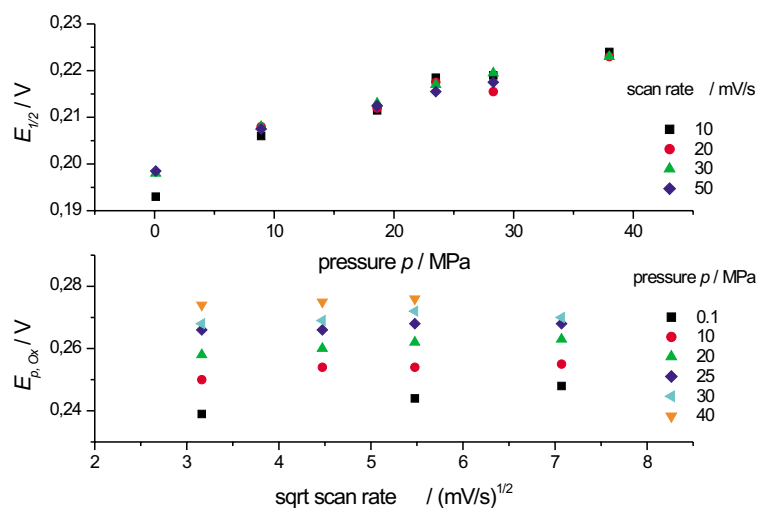
Figure 7.4: The half-way potential as a function of pressure (top) and the oxidation peak potentials as a function of the scan rate (bottom). From linear fits to $E_{1/2}(p)$ the reaction volume of the reaction (7.5) can be determined.

The bottom graph of figure 7.4 shows the oxidation peak potential as a function of the sweep rate. In a reversible system this curve should be constant since E_p does not depend on ν. In the case of the presented measurements the peak potential stays virtually constant

for all pressures.

Yet another prediction that a Nernstian reversible system has to fulfil is that the ratio of the peak currents of oxidation and reduction is one. This means that the forward reaction is just as strong as the backward reaction and no oxidation product is lost, which cannot be re-converted into the reduced species. Figure 7.5 plots the ratio $I_{p,Ox}/I_{p,Red}$ as a function of the square root of the sweep rate for various pressures. The figure shows, on the one hand, that pressure has no impact on the ratio of the peak currents regardless of their decrease with pressure. On the other hand, the ratio is not constant and equal to one. Since no variation with pressure is observed one can assume that this behaviour results from the gold working electrode. It is known that gold has some surface functionalities that influence for example the value of the peak separation. The thermally evaporated sample cannot be extensively cleaned prior to use. Furthermore, it is exposed to the environment for a long time while the pressure cell is assembled. As a consequence, the working electrode is far from being ideal. Deviations from the strictly reversible behaviour have to occur.
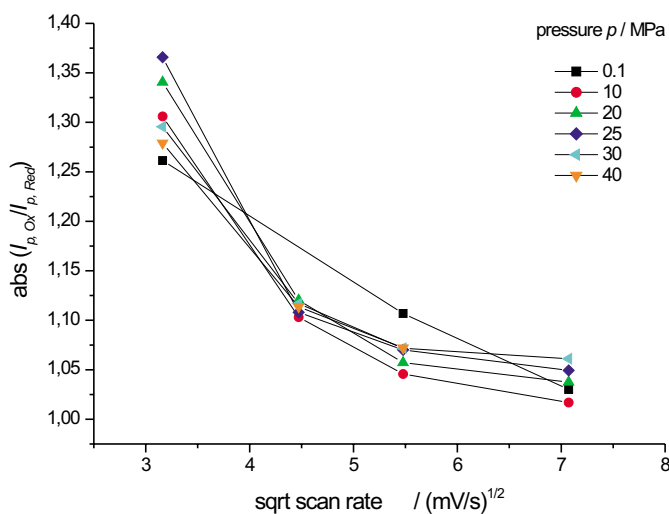
Figure 7.5: The ratio of the peak currents of oxidation and reduction versus the scan rate at different pressures.

In conclusion, the system is found to be quasi-reversible supported by the facts that the peak separation is somewhat higher than expected and that the ratio of the peak

currents is not equal to 1. On the other hand, the peak current is a linear function of the square root of the scan rate and the peak potentials are virtually constant. With this in mind the $I_p(\nu)$ curves can be evaluated using the Randles-Ševčik equation (2.82), which is valid only for reversible systems, to give the diffusion coefficient of the reactant at different pressures as shown in fig. 7.6. The value of calculated diffusion coefficient D lies within a reasonable range for solutes in fluids and decreases with increasing pressure due to a higher density of the reaction medium. It has to be mentioned, though, that the influence of the compression of the bulk medium has been neglected. Rather than D the above evaluation yields $D(c_p/c_0)^2$ with c_p and c_0 being the bulk concentration at elevated pressures and at atmospheric pressure, respectively. Krasiński et al. [184] could show that the compressibility of a medium with NaCl as electrolyte influences the diffusion coefficient. The concentration changes in a NaCl electrolyte solution with pressure affect the diffusion coefficient and consequently its value is reduced by up to 20 % at 1000 MPa.
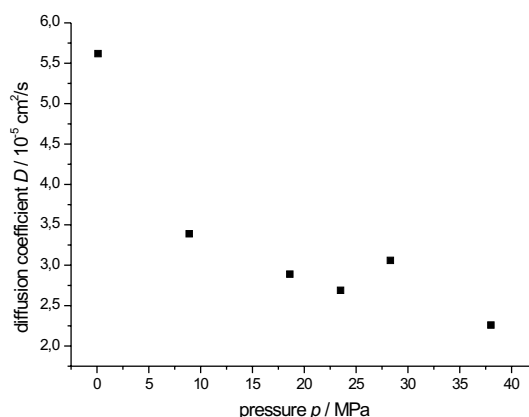
Figure 7.6: The diffusion coefficient as a function of pressure as determined from eqn. (2.82) under the assumption of a constant bulk concentration.

7.3 Electro-Polymerisation of Thiophene

The combination of SPR and CV is bound to give new results on the optical properties of electro-polymerised films. In this study the monomer thiophene is used mostly due to its

solvent properties. Where acidic solutions, which are needed for e.g. the polymerisation of aniline, tend to interact with the steel of the cell, acetonitrile solutions do not produce any visible deterioration of the steel. It should be noted, however, that due to the limited time for this project only first results can be presented. It is necessary to perform more thorough investigations on this material system.

Polythiophenes and especially polythiophene derivatives are widely used in the field of organic molecular electronics [185]. Applications in devices including polymer light emmiting diodes [186], field-effect transistors [187], and photovoltaic cells [188] require good quality ultrathin films since sandwich devices are frequently used. Organic polymers such as polythiophene have very complicated morphological structures depending on the method of synthesis. Consequently, the synthesis has strong impact on the physical properties of the produced polymer. The electrochemical properties of thin polythiophene films largely depend on the supporting electrolyte [189], the working electrode preparation method [190], or the solubilities of the monomer and the polymer [191]. Pressure as well as temperature are bound to influence the film formation qualities and the properties of the deposited layer since both affect for example the solubilities of materials or the transport properties.
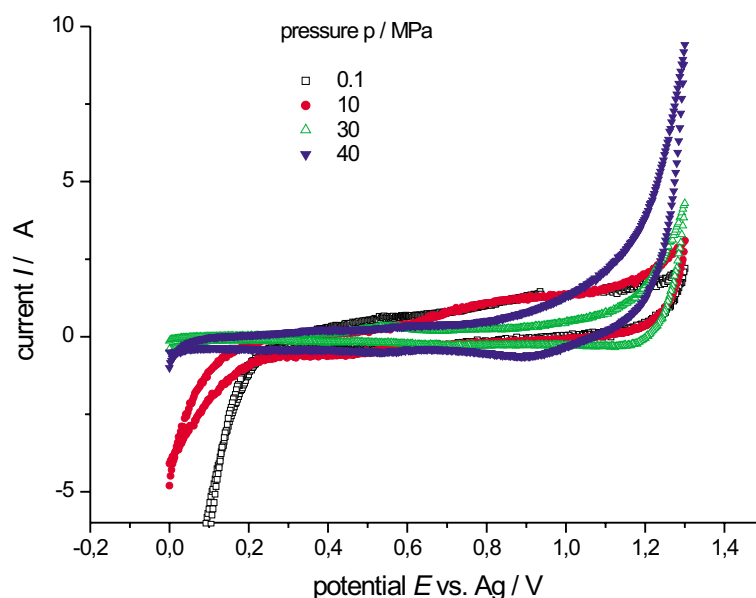
Figure 7.7: Cyclic voltammograms of 0.1 M thiophene, 0.1 M LiClO$_4$ in acetronitrile. Depicted are the first sweeps of different samples measured at 0.1, 10, 30, and 40 MPa, respectively.

Figure 7.7 shows the first potential sweeps of different samples at 0.1 MPa, 10 MPa, 30 MPa, and 40 MPa, respectively. The distinct feature of the electrochemical behaviour of thiophene can be seen from about 1.2 V (vs. Ag) on. Here, the monomer is oxidised. The return potential is not high enough to resolve the anodic peak but high enough to promote film growth. At 0.1 MPa and 10 MPa there occurs oxidation at low potentials, which is contributed to contaminations in the solvent. From this graph it can also be seen that the current at the return point of the potential increases with pressure. In the absence of any pressure effects on the reference electrode this means that either the oxidation peak potential has shifted to lower values or that the peak current drastically increases with pressure. The nature of this behaviour remains unclear.
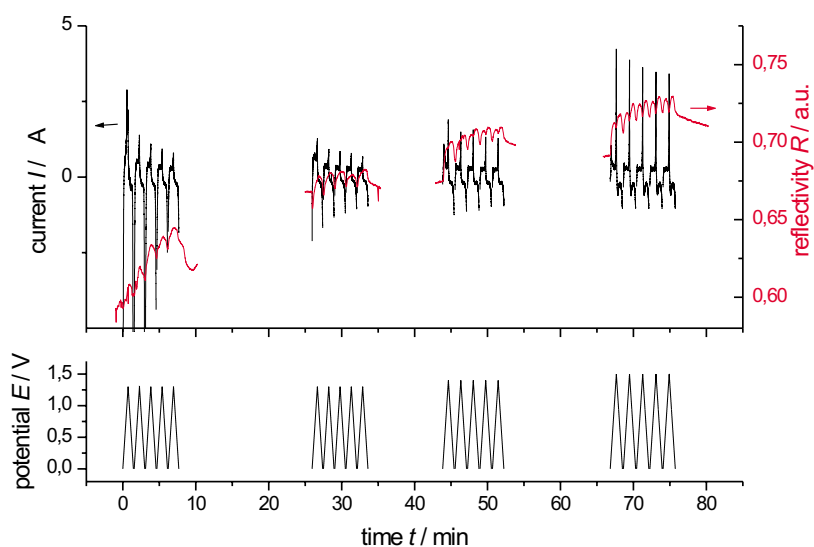
Figure 7.8: The reflectivity, the current, and the potential are shown as a function of time at 0.1 MPa. The increase of the reflectivity indicates the formation of polythiophene at the gold working electrode.

The relation between the surface plasmon reflectivity and the cyclo-voltammetric current is shown in figure 7.8 as a function of time. The data are recorded at atmospheric pressure and the return potential of the sweep is increased from 1.3 V (vs. Ag) to 1.4 V and 1.5 V after the 10th and the 15th cycle, respectively. In the potential range where oxidation takes place the reflectivity increases, when the scan direction is reverted R decreases again. The reflectivity therefore monitors the optical thickness increase each time when

thiophene is oxidised. The drop of reflectivity when decreasing the potential might have various reasons. One of them could be changed optical properties or thickness when the polymer is either in the oxidised/conducting or in the de-doped state. Also, the doping/de-doping process itself going along with the sweep might influence the optical response. In experiments with an electrochemical quartz-crystal-microbalance thiophene co-polymers have shown a mass increase and decrease with cycling in positive and negative direction [192]. The general positive trend of the reflectivity indicates that a polymer film of increasing thickness is formed on the surface as the number of cycles increases. Regarding the cyclic voltammetry curves, the peak current decreases with the cycle number. For that reason the return potential is increased from the 10th cycle on. Gonçalves et al. [190] suggest that only an increasing current with successive cycling is related to a continuous increase in film thickness. In their experiments the current increases up to the second cycle and then decreases monotonously.
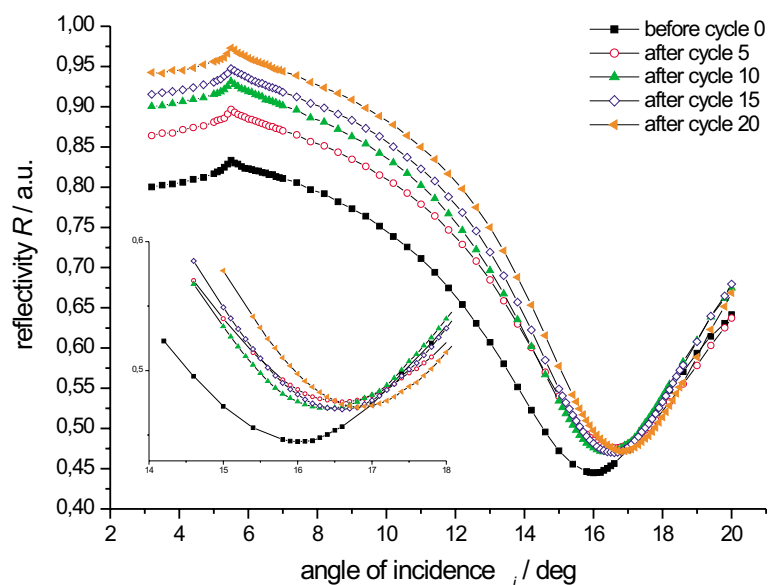
Figure 7.9: Surface plasmon angular scans after the completion of 5, 10, 15, and 20 cycles, respectively.

The answer to this discrepancy between the SPR and the CV signal is found in figure 7.9. The reflectivity increase with the number of cycles is due to a change of shape of the surface plasmon resonance. This effect is also observed in the experiments at elevated pressure, however to a much less extend. Up to now the origin of this change is still unclear

but it might be attributed to the condition of the gold working electrode. Nevertheless, the thickness of the polythiophene layer can still be determined from the minimum of the surface plasmon resonance. After a large initial (after 5 cycles) increase the thickness of the layer stays constant or decreases slightly (cf. figs. 7.9 and 7.11). Moreover, no further increase in the thickness triggered by an increased turning point potential is observed. The results of Gonçalves et al. [190] fall along these lines. After the second cycle their current at the return potential decreases. Also after increasing the return potential they found no increase in current. They reasoned that even small traces of water in acetonitrile containing $LiClO_4$ initiates the passivation of the electrode, which effectively prevents the polymerisation procedure.
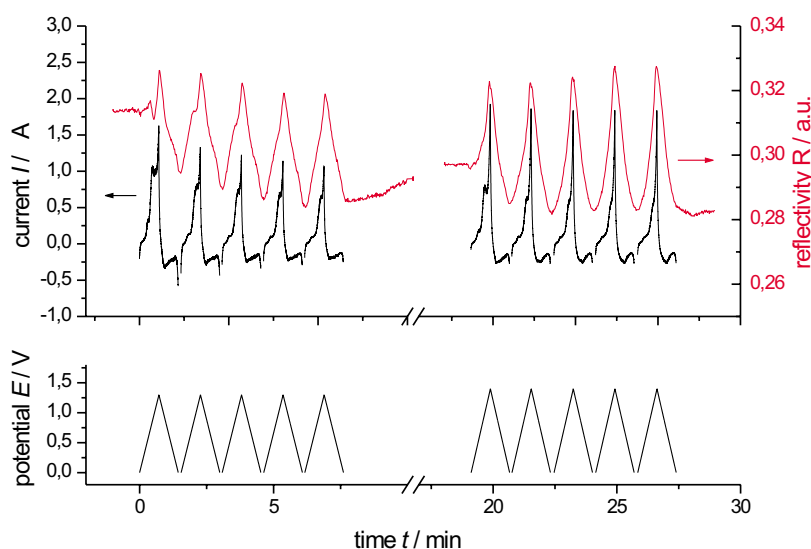
Figure 7.10: A zoom in on the reflectivity/current correlation as a function of time. The pressure is 30 MPa. The net reflectivity decreases with time.

Figure 7.10 presents the first 10 cycles of the thiophene polymerisation at 30 MPa. The reflectivity/cyclic voltammetry correlation is the same as in the case of the measurements at 0.1 MPa. Upon oxidisation R increases, while de-doping it decreases. However, the general trend of R in this case is negative. Also the angular scan curves reveal that the resonance minimum shifts to lower values. Since negative thickness values cannot be explained physically it is again assumed that changes at the working electrode alter its

optical response.
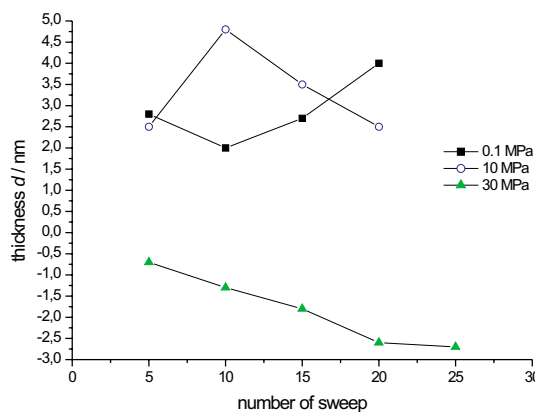
Figure 7.11: Thiophene thickness as a function of the number of cycles for different pressures. At 30 MPa the negative thicknesses are determined from SPR measurements as the resonance shifts to lower angles.

With respect to the above discussion the surface plasmon resonance curves have to be evaluated carefully. At 0.1 MPa and 10 MPa the thickness of the film on the surface is more or less constant, independent of the number of cycles (cf. fig. 7.11). This could either be due to actual polymerisation or to passivation of the surface. In the case of the data at 30 MPa clearly the properties of the working electrode are changed. Even though the electrolyte $LiClO_4$ is known to inhibit the corrosion of gold [190; 191] these processes at elevated pressures are still to be excluded.

7.4 Conclusion

In this section a new high-pressure cell is presented that combines the two measurement methods SPR and cyclic voltammetry with each other. In order to proof that accurate electrochemical measurements are feasible the equipment is tested on the well-characterised potassium hexacyanoferrate(III)-(II) system. First measurements with the combination of the optical and the electrochemical techniques on the electro-polymerisation are presented thereafter.

Potassium hexacyanoferrate(III)-(II) is a reversible redox system that can be used to test electrochemical equipment. The criteria for reversibility are the linearity of $I_p(\sqrt{\nu})$,

a constant peak potential separation of 59 mV with $\sqrt{\nu}$ at ambient conditions and a constant ratio of $I_{p,Ox}/I_{p,Red} = 1$. Indeed, a linear behaviour of the peak current with the square root of the sweep rate is observed. From the pressure dependence of the slopes the diffusion coefficient is determined as a function of pressure. The Randles-Ševčik equation yields values that are reasonable for solutes in fluids and the diffusion coefficient decreases with pressure, as expected. The peak potential separation is also found to be virtually independent of $\sqrt{\nu}$. The value of the peak separation, though, is larger than 59 mV. However, this value is a function of the condition of the electrode. Especially gold working electrodes are known to show larger values than the ideal 59 mV. Not only the peak current but also the peak potential varies with pressure. From this dependence the molar volume change of the redox reaction can be calculated. In the case of the presented data the value is higher than the volumes found in literature. This discrepancy is also related to the gold electrode as the preparation method that is used does not provide the possibility for extensive cleaning of the gold surface. The evaluation of the peak currents corresponds with these findings as well. The ratio of the peak currents is in favour of the oxidation at low sweep rates, however approaches the value of 1 for higher scan rates. In conclusion, electrochemical experiments work well in the high-pressure cell. However, the preparation of the working electrode should be done carefully. A change of the cleaning procedure prior to the measurements might proof useful.

The cyclic voltammetry curves of thiophene in acetonitrile with $LiClO_4$ as electrolyte show the distinct oxidation peak when thiophene is oxidised and the polymerisation initiated. The simultaneous recording of the surface plasmon reflectivity at 0.1 MPa reveals an apparent thickness increase with the number of sweep cycles. The evaluation of the corresponding scan curves however yields that the thickness stagnates after an initial rise after the first few cycles. The data for 30 MPa show a steady decrease of the polymer thickness, even resulting in negative values. The assumption that unwanted processes at the gold surface influence the polymerisation behaviour is confirmed by literature [190]. There, it is found that even small amounts of water present in the solution lead to a passivation of the gold surface, which prevents polymerisation. In the future, these polymerisation experiments should be conducted in a different reaction medium. Gonçalves et al. [190] report that e.g. with tetrabutylammonium tetrafluoroborate (TEABF$_4$) as electrolyte no such passivation layers develop. The drawback of this system is, however,

that the gold layer undergoes slight anodic dissolution in the first few sweeps.

8. Summary

The influence of pressure on the properties of thin dielectric layers is investigated by surface plasmon spectroscopy. The main objective is set on the development of the measurement technique at elevated pressures. For this reason this study has two aspects: From the material's viewpoint, hydrogels, DNA hybridisation, and the polymer-supercritical carbon dioxide interaction are studied. From the application point of perspective, a sol-gel procedure is introduced to accommodate for silane binding chemistry on metal surfaces, a fluorescence detection procedure is added to the high pressure SPS set-up, and HPSPR is introduced to a supercritical fluid mixture environment. Additionally, another part covers the design and development of a new pressure cell that combines the measurement techniques surface plasmon spectroscopy and electrochemistry.

The preparation of thin sol-gel silica layers on planar metal surfaces is studied first. It comprises three assembly steps that are characterised and optimised separately. Different thicknesses of the silica films can easily be adjusted by the concentration of TMOS in the sol. AFM and x-ray reflectometry experiments reveal that the surfaces are very homogenous and show low surface roughness. As a result, the stability of the sol-gel modified metal surfaces in PBS buffer is quite remarkable. Furthermore, no degradation due to elevated pressures can be determined.

An application of these layers is given in terms of the characterisation of N-isopropylacrylamide gels, which are bound via silane chemistry to the silica film. These thermoresponsive polymer gels have a volume phase transition whose properties are altered by pressure. The confinement of the hydrogel to the surface additionally influences the transition behaviour. It is found that the transition temperature at low ionisable co-monomer concentration is lower than in bulk gels. High co-monomer concentrations lead to the opposite effect. Most likely, there exists a characteristic length scale over which the effects of the substrate are felt by the gel film. The confinement also results in a different pressure

dependence of the phase transition as compared to bulk gels. In contrast to the latter, thin films have no discontinuous phase transition; the transition width rather increases monotonously with pressure.

The characterisation of DNA hybridisation reactions at surfaces and at elevated pressures is firstly studied by means of an SPR set-up capable of fluorescence detection. The architecture of the molecular sensor involves the assembly of a streptavidin binding matrix, onto which the 5' end biotinylated probe oligonucleotide binds. For the final characterisation of the hybridisation process it is therefore of importance that the stability of the underlying layers is ascertained. The thiol layer, which provides a mediating layer between the metal and the streptavidin, is found to be stable in the instrumental temperature and pressure range. The streptavidin layer also shows no significant dependence on the pressure, however at temperatures between 45 °C and 50 °C the layer destabilises due to a weakened biotin-streptavidin bonding. These values are about 5 °C larger than the ones found in literature, which attributed to pressure stabilising the biotin-streptavidin interaction.

Subsequent binding of fluorescent-labelled probe DNA is recorded utilising the fluorescence signal of the labels being excited in the surface plasmon field. Temperature and pressure variation leads to a decrease and an increase of the signal, respectively. The single strand DNA can be assumed to have a random conformation. Entropic reasons and varying solute-solvent interactions are made responsible for the signal changes. When a fluorescent-labelled DNA target with one mismatching base is injected to interact with an unlabelled probe, immediate hybridisation occurs. This process can be described in the Langmuir picture. Increasing the temperature to a value closer to the melting temperature of the duplexes leads to a drop of fluorescence signal due to desorption of molecules. With pressure, on the other hand, the signal increases, implying that pressure favours the hybridisation process. The hybridisation is thus coupled to a negative volume change. A zero mismatch target provides further evidence for this argumentation. This duplex is only slightly influenced by temperature and pressure. The higher binding affinity between both DNA strands results in an almost saturated surface coverage and the shifts of the Langmuir isotherm in response to temperature and pressure changes has no effect on the fluorescence signal.

Supercritical carbon dioxide as solvent possesses technological potential due to its re-

markable chemical and physical properties and its environmental inertness. Within the context of this study the refractive index of carbon dioxide is measured up to 200 MPa and compared to existing formulas describing the refractive index/density correlation. Of the empirical equations the one given by Gladstone and Dale fits the data best. The commonly used description of a virial expansion of the Lorentz-Lorenz equation yields good agreement of the first virial coefficient with literature if constant second and third virial coefficients are extracted from literature. In a different set of experiments the refractive index changes and the swelling behaviour of PMMA films in $scCO_2$ and $scCO_2$/MMA mixtures are investigated. With increasing pressure PMMA absorbs a higher an amount of carbon dioxide, which swells the polymer film. As a consequence, the refractive index of the polymer film decreases since the refractive index of CO_2 is lower than the one of PMMA. Calculations based on the assumption of an ideal mixture qualitatively describe the behaviour of the refractive index changes.

In the second part of this study the development of a new high-pressure surface plasmon spectroscopy cell is described. The combination with electrochemical experiments that can now be performed simultaneously can lead to new insight in electrochemical processes that influence the optical properties the reaction medium near the working electrode. The cell is tested on the potassium hexacyanoferrate(III)-(II) system. Reproducible cyclic voltammograms can be recorded at various sweep rates and pressures. The peak current is a linear function of the square root of the sweep rate and the peak potential does not depend on the scan rate. From the pressure dependence of the peak current the molar volume change of the electrochemical reaction is determined. The value, though, is rather high, which is attributed to the properties of the working electrode. The diffusion coefficient of the reactants is calculated from the peak potential/pressure relation. The coefficients lie in reasonable range for solutes in fluids and decrease with increasing pressure. The peak potential separation, on the other hand, is found to be slightly above the value of a reversible reaction due to the rather imperfect gold working electrode surface.

After the cell has been shown to be reliable with respect to electrochemistry, first results on the pressure dependence of the electropolymerisation of thiophene are presented. At atmospheric pressure, the simultaneous recording of the surface plasmon reflectivity signal shows an increasing thickness as the potential is repeatedly cycled to the oxidation potential. At elevated pressures, however, an initial negative reflectivity response is found,

which is reasoned to be a result of a passivated electrode. This behaviour still has to be investigated in more detail as the restricted time for this project limited the amount of data that could be collected.

List of Figures

164

List of Tables

Bibliography

[1] E. Kato. *Journal of Chemical Physics* **106** (9) 3792–3797, 1997.

[2] K. Zosel. *Patent* **2,079**, 261, 1971.

[3] O. Prucker, S. Christian, H. Bock, J. Rühe, C. W. Frank und W. Knoll. *Macromolecular Chemistry and Physics* **199** (7) 1435–1444, 1998.

[4] G. Kleideiter. *Oberflächenplasmonen- und Wellenleitermoden-Spektroskopie unter hohen hydrostatischen Drücken.* Ph.d. thesis, 1999.

[5] G.M. Eichenbaum, P.F. Kiser, S.A. Simon und D. Needhan. *Macromolecules* **31** 5084–5093, 1998.

[6] Y. Hirokawa und T. Tanaka. *Journal of Chemical Physics* **81** (12) 6379–6380 J CHEM PHYS, 1984.

[7] T. Liebermann und W. Knoll. *Colloids and Surfaces a-Physicochemical and Engineering Aspects* **171** (1-3) 115–130, 2000.

[8] R. G. Wissinger und M. E. Paulaitis. *Journal of Polymer Science Part B-Polymer Physics* **25** (12) 2497–2510, 1987.

[9] P. D. Condo und K. P. Johnston. *Journal of Polymer Science Part B-Polymer Physics* **32** (3) 523–533, 1994.

[10] H. Wieder. *Festkörperunterstützte Lipid-Modellmembranen auf Gold zur Rekonstitution von Membranproteinen.* Ph.d. thesis, 2000.

[11] A. Baba, R. Advincula und W. Knoll. *Polymeric Materials: Science & Engineering* **84** 369–370, 2001.

[12] D. Axelrod, T.P. Burghardt und N.L. Thompson. *Annual Reviews in Biophysics and Bioengineering* **13** 247–268, 1984.

[13] E. Burstein, W. P. Chen, Y. J. Chen und A. Hartstein. *Journal of Vacuum Science & Technology* **11** (6) 1004–1019, 1974.

[14] C. Kittel. *Introduction to solid state physics.* John Wiley & Sons Inc. London, 1953.

[15] E. Kretschmann. *Optics Communications* **6** (2) 185–187, 1972.

[16] J. R. Sambles, G. W. Bradbery und F. Z. Yang. *Contemporary Physics* **32** (3) 173–183, 1991.

[17] A. Otto. *Zeitschrift für Physik* **216** 398–410, 1968.

[18] E. Kretschmann. *Zeitschrift für Physik* **241**, 313, 1971.

[19] H. Raether. In G. Hass, M.H. Francombe und R.W. Hoffmann, (Eds.), *Physics of Thin Films* Band 9, . Academic Press New York, 1977.

[20] R. Petit. *Electromagnetic theory of gratings.* Springer Verlag, 1980.

[21] L. Kayandjian. *Physical Review E* **54** (6) 6902–6915, 1996.

[22] K. A. Peterlinz und R. Georgiadis. *Optics Communications* **130** (4-6) 260–266, 1996.

[23] W. Knoll. In R.E. Hummel und P. Wißmann, (Eds.), *Handbook of Optical Properties* Band II, Optics of Small Particles, Interfaces, and Surfaces 373–399. CRC Press Boca Raton, New York, London, Tokyo, 1997.

[24] P. K. Tien. *Reviews of Modern Physics* **49** (2) 361–420, 1977.

[25] W. Knoll. *Annual Review of Physical Chemistry* **49** 569–638, 1998.

[26] P.K. Tien, R. Ulrich und R.J. Martin. *Applied Physics Letters* **14** (9) 291–294, 1969.

[27] M. Born und E. Wolf. *Principles of Optics.* Pergamon Press Oxford 6th edition, 1980.

[28] W. Karthe und R. Müller. *Integrierte Optik.* Akademische Verlagsgesellschaft Geest & Portig, 1991.

[29] H.A. Lorentz. *Wied. Ann.* **9**, 641, 1880.

[30] L. Lorenz. *Wied. Ann.* **11**, 70, 1880.

[31] D. Dale und F. Gladstone. *PHil. Trans.* **148**, 887, 1885.

[32] M.J.F. Kykman. *Recueil. Frav. Chim. Pays-Bas* **14**, 185, 1895.

[33] G. Jaeckel. In E. Gehrke, (Ed.), *Handbuch der physikalischen Optik* Band 1 186–218. Barth Leipzig, 1922.

[34] K. Vedam und P. Limsuwan. *Journal of Chemical Physics* **69** (11) 4762–4771, 1978.

[35] H. J. Achtermann, G. Magnus und T. K. Bose. *Journal of Chemical Physics* **94** (8) 5669–5684, 1991.

[36] J. Obriot, J. Ge, T. K. Bose und J. M. Starnaud. *Fluid Phase Equilibria* **86** 315–350, 1993.

[37] H. Eisenberg. *Journal of Chemical Physics* **43** (11) 3887–3892, 1965.

[38] A. Proutiere, E. Megnassan und H. Hucteau. *The Journal of Physical Chemistry* **96**, 3485, 1992.

[39] P.G. Tait. *Physical Chemistry* **2** (1), , 1889.

[40] J. H. Dymond und R. Malhotra. *International Journal of Thermophysics* **9** (6) 941–951, 1988.

[41] M. Schmidt und F. H. J. Maurer. *Journal of Polymer Science Part B-Polymer Physics* **36** (6) 1061–1080, 1998.

[42] R.Z. Chang, C.H. Chen und K.S. Su. *Polym. Eng. Sci.* **36**, 1789, 1996.

[43] R. Simha und P.S. Wilson. *Kolloid Zeitschrift* **251**, 402, 1973.

[44] W.G. Cutler, R.H. McMickle, W. Webb und R.W. Schiessler. *The Journal of Chemical Physcs* **29**, 727, 1958.

[45] T. Yamashita. *Japanese Journal of Applied Physics Part 1-Regular Papers Short Notes & Review Papers* **33** (7A) 4025–4031, 1994.

[46] V.S. Nanda und R. Simha. *The Journal of Chemical Physics* **21**, 1884, 1964.

[47] R. Simha und T. Somcynsky. *Macromolecules* **2**, 342, 1969.

[48] T. Somcynsky und R. Simha. *The Journal of Applied Physics* **42**, 4545, 1971.

[49] R.K. Jain und R. Simha. *Macromolecules* **13**, 1501, 1980.

[50] J.R. Lakowicz. *Principles of Fluorescence Spectroscopy.* Plenum Press New York, 1983.

[51] I.B. Berlman. *Energy Transfer Parameters of Aromatic Molecules.* Academic Press London, 1973.

[52] H. Kuhn. *Journal of Chemical Physics* **53**, 101, 1970.

[53] C.F. Eagen, W.H. Weber, S.L. McCarthy und R.W. Terhune. *Chemical Physics Letters* **75**, 274, 1980.

[54] P.W. Atkins. *Physical Chemistry.* 6th edition, 1998.

[55] G. Kleideiter, O. Prucker, H. Bock, C. W. Frank, M. D. Lechner und W. Knoll. *Macromolecular Symposia* **145** 95–102, 1999.

[56] G. Kleideiter, M. D. Lechner und W. Knoll. *Macromolecular Chemistry and Physics* **200** (5) 1028–1033, 1999.

[57] M. Kreiter. *Oberflächenplasmonen-artige Resonanzen auf metallischen Gittern.* Ph.d. thesis, 2000.

[58] T. Neumann. *Strategies for Detecting DNA Hybridisation Using Surface Plasmon Fluorescence Spectroscopy.* Ph.d. thesis, 2001.

[59] G. Kleideiter, Z. Sekkat, M. Kreiter, M. D. Lechner und W. Knoll. *Journal of Molecular Structure* **521** 167–178, 2000.

[60] G. Binning, C.F. Quate und C. Gerber. *Physical Review Letters* **56** (9) 930–933, 1986.

[61] H. Kiessig. *Annalen der Physik* **10** (769), , 1931.

[62] L.G. Parrat. *Physical Review B* **95**, 359, 1954.

[63] A. Naudon, J. Chihab, P. Goudeau und J. Mimault. *Journal of Applied Crystallography* **22**, 460, 1989.

[64] P. Alluri, J. Conner, B.Y. Nguyen, L. Prabhu, J. Schaeffer, J. Formica, L. Vu, D. Berman, A. Dikopoltsev und B. Yokhin. *Future Fab International* (10) 257–259, 2000.

[65] X. Mai, R. Moshrefzadeh, U.J. Gibson, G.I. Stegeman und C.T. Seaton. *Applied Optics* **24** (19) 3155–3161, 1985.

[66] L. Holland. *Vacuum Deposition of Thin Films.* Chapmann and Hall Ldt. London, 1966.

[67] A. Badia, S. Arnold, V. Scheumann, M. Zizlsperger, J. Mack, G. Jung und W. Knoll. *Sensors and Actuators B-Chemical* **54** (1-2) 145–165, 1999.

[68] C.D. Bain und G.M. Whitesides. *Advanced Materials* **4**, 110, 1989.

[69] J. W. Robertson, M. Cai und J. E. Pemberton. *Advanced Materials* **13** (9) 662–667, 2001.

[70] D. K. Kambhampati, T. A. M. Jakob, J. W. Robertson, M. Cai, J. E. Pemberton und W. Knoll. *Langmuir* **17** (4) 1169–1175, 2001.

[71] W. R. Thompson, M. Cai, M. K. Ho und J. E. Pemberton. *Langmuir* **13** (8) 2291–2302, 1997.

[72] W. R. Thompson und J. E. Pemberton. *Chemistry of Materials* **7** (1) 130–136, 1995.

[73] C.J. Brinker und G.W. Scherer. *Sol-Gel Science: The Physics and Chemistrz of Sol-Gel Processing.* Academic Press San Diego, 1990.

[74] M.E. Harmon, T.A.M. Jakob, W. Knoll und C.W. Frank. *Macromolecules (accepted),* .

[75] J. J. Zheng, T. Odake, T. Kitamori und T. Sawada. *Analytical Chemistry* **71** (21) 5003–5008, 1999.

[76] P.C. Weber, D.H. Ohlendorf, J.J. Wndoloski und F.R. Salemme. *Science* **243** 85–88, 1989.

[77] A. Chilkoti und P. S. Stayton. *Journal of the American Chemical Society* **117** (43) 10622–10628, 1995.

[78] M. Wilchek und E.A. Bayer. In *Methods in Enzymology* Band 184, . Academic Press San Diego, 1990.

[79] W.A. Hendrickson, A. Pähler, J.L. Smith, Y. Satow und E.A. Merritt. *Proceedings of the National Academy of Science USA* **85** 2190–2194, 1989.

[80] R.C. Ebersole, J.A. Miller, J.R. Moran und M.D. Ward. *Journal of the Americal Chemical Society* **112**, 3239, 1990.

[81] C.K. Chignell, D.K. Starkweather und G.K. Sinha. *Biological Chemistry* **250** 5622–5630, 1975.

[82] W. Müller, H. Ringsdorff, E. Rump, X. Zhang, L. Angermaier, W. Knoll und J. Spinke. *Journal of Biomaterial Science - Polymer Edition* **6**, 481, 1994.

[83] W. et al. Knoll. *Colloids and Surfaces A* **161** 115–137, 2000.

[84] J. Spinke, M. Liley, F. J. Schmitt, H. J. Guder, L. Angermaier und W. Knoll. *Journal of Chemical Physics* **99** (9) 7012–7019, 1993.

[85] T. Liebermann. *Oberflächenplasmonen-Fluoreszenzspektroskopie zur Detektion molekularer Erkennungsreaktionen.* Ph.d. thesis, 1998.

[86] J.D. Watson und F.H.C. Crick. *Nature* **171** 737–738, 1953.

[87] W. Saenger. *Principles of Nucleic Acid Structure.* Springer New York, 1983.

[88] V.J. Krukonis und M.A. McHugh. *Supercritical Fluid Extraction: Principles and Practice.* Butterworth-Heineman Boston 2nd edition, 1994.

[89] K.F. Shaffer und J.M. DeSimone. *Trends in Polymer Science* **3**, 146, 1995.

[90] S.A. Cretté und J.M. DeSimone. *Nachrichten aus der Chemie* **49** (4) 462–466, 2001.

[91] J. L. Kendall, D. A. Canelas, J. L. Young und J. M. DeSimone. *Chemical Reviews* **99** (2) 543–563, 1999.

[92] F. Rindfleisch, T. P. DiNoia und M. A. McHugh. *Journal of Physical Chemistry* **100** (38) 15581–15587, 1996.

[93] J.A. Hyatt. *Journal of Organic Chemistry* **49** 5097–5101, 1984.

[94] K. O'Shea, K. Kirmse, M. Fox und K. Johnston. *Journal of Physical Chemistry* **95**, 7863, 1991.

[95] J. M. Desimone, Z. Guan und C. S. Elsbernd. *Science* **257** (5072) 945–947, 1992.

[96] V. Krukonis. *Polymer News* **11** 7–16, 1985.

[97] J.B. McClain, D.E. Betts, D.A. Canelas, E.T. Samulski, J.M. DeSimone, J.D. Londono, H.D. Cochran, G.D. Wignall, D. Chilluran-Martino und R. Triolo. *Science* **274**, 2049, 1996.

[98] C. Shi, Z. Huang, S. Kilic, J. Xu, R.M. Enick, E.J. Beckman, A.J. Carr, R.E. Melendey und A.D. Hamilton. *Science* **286**, 1540, 1999.

[99] K.P. Johnston, K.L. Harrison, M.J. Clarke, S.M. Howdle, M.P. Heity, F.V. Bright, C. Cartier und T.W. Randolph. *Science* **271**, 624, 1996.

[100] Y. Kamiya, K. Mizoguchi, K. Terada, Y. Fujiwara und J. S. Wang. *Macromolecules* **31** (2) 472–478, 1998.

[101] R. G. Wissinger und M. E. Paulaitis. *Journal of Polymer Science Part B-Polymer Physics* **29** (5) 631–633, 1991.

[102] P. D. Condo, D. R. Paul und K. P. Johnston. *Macromolecules* **27** (2) 365–371, 1994.

[103] U. Fehrenbacher, T. Jakob, T. Berger, W. Knoll und M. Ballauff. *Fluid Phase Equilibria* **accepted**, , 2001.

[104] A. Fugishima. *Electrochemistry*. Gihodo Tokio, 1984.

[105] X. Chen, X.E. Zhang, Y.Q. Chai, W. Hu, Z. Zhang, X. Zhang und A.E.S. Cas. *Biosensors and Bioelectronics* **13** 451–458, 1998.

[106] T.M. Herne und M.J. Tarlov. *The Journal of the American Chemical Society* **119** 8916–8920, 1997.

[107] C.E. Jordan, A.G. Frutos, A.J. Thiel und R. Corn. *Analytical Chemistry* **69** 4939–4947, 1997.

[108] M. Zizlsperger und W. Knoll. *Progress in Colloid and Polymer Science* **109** (1) 244–253, 1998.

[109] P. Plueddemann. Plenum Press New York 2nd edition, 1991.

[110] M. Chee, R. Yang, E. Hubbell, A. Berno, X.C. Huang, D. Stern, J. Winkler, D.J. Lockhart, M.S. Morris und S.P.A. Fodor. *Science* **271** 610–614, 1996.

[111] S.P.A Fodor. *Science* **277** 393–395, 1997.

[112] O. Prucker und J. Ruhe. *Langmuir* **14** (24) 6893–6898, 1998.

[113] M. Biesalski und J. Rühe. *Macromolecules* **32** 2309–2316, 1999.

[114] W. R. Thompson und J. E. Pemberton. *Chemistry of Materials* **5** (3) 241–244, 1993.

[115] J. J. Cras, C. A. Rowe-Taitt, D. A. Nivens und F. S. Ligler. *Biosensors & Bioelectronics* **14** (8-9) 683–688, 1999.

[116] M. Shibayama und T. Tanaka. In K. Dusek, (Ed.), *Advances in Polymer Science* Band 109 1–62. Springer-Verlag Berlin, 1993.

[117] L.C. Dong und A.S.J. Hoffman. **31** (21-31), , 1990.

[118] N. Reber, R. Spohr, A. Wolf, H. Omichi, M. Tamada und M. Yoshida. *The Journal of Membrane Science* **140** 275–281, 1998.

[119] T. Okano, N. Yamada, M. Okuhara, H. Sakai und Y. Sakurai. *Biomaterials* **16** 297–303, 1995.

[120] N.A. Plate, T.L. Lebedeva und L.I. Valuev. *Polymer Journal* **31** 21–27, 1999.

[121] C. Nakamoto, T. Kitada und E. Kato. *Polymer Gels Networks* **4** 17–31, 1996.

[122] E. Kato, T. Kitada und C. Nakamoto. *Macromolecules* **26** (7) 1758–1760, 1993.

[123] A. Suzuki und S. Kojima. *Journal of Chemical Physics* **101** (11) 10003–10007, 1994.

[124] E. Wischerhoff, T. Zacher, A. Laschewsky und E.D. Rekai. *Angewandte Chemie, International Edition* **39** 4602–4604, 2000.

[125] B. Peng, D. Johannsmann und J. Rühe. *Macromolecules* **32** 6759–6766, 1999.

[126] J. Hoffman, M. Plotner, D. Kuckling und W.-J. Fischer. *Sensors and Actuators A* **77** 139–144, 1999.

[127] X. Zhong, Y. X. Wang und S. C. Wang. *Chemical Engineering Science* **51** (12) 3235–3239, 1996.

[128] D.R. Lide, (Ed.). *CRC Handbook of Chemistry and Physics*. CRC-Press Cleveland 74th edition, 1994.

[129] J.E. Mark, (Ed.). *Polymer Data Handbook*. Oxford University Press Oxford, 1999.

[130] L.H. Adams. *Journal of the American Chemical Society* **53** 3769–3813, 1931.

[131] J.-H. Zhao, M. Kiene, C. Hu und P.S. Ho. *Applied Physics Letters* **77** 2843–2845, 2000.

[132] S. Hirotsu und A. Onuki. *Journal of the Physical Society of Japan* **58** (5) 1508–1511, 1989.

[133] M.E. Harmon, T. Jakob, W. Knoll und C.W. Frank. *Presented at AIChE Annual Meeting*, , 2000.

[134] O. Prucker, M Schimmel, G. Tovar, W. Knoll und J. Rühe. *Advanced Materials* **10** 1073–1077, 1998.

[135] M.E. Harmon, D. Kuckling und C.W. Frank. *Submitted for Presentation at AIChE Annual Meeting*, , 2001.

[136] D. N. Dubins, A. Lee, R. B. Macgregor und T. V. Chalikian. *Journal of the American Chemical Society* **123** (38) 9254–9259, 2001.

[137] C.G. Hedén, T. Lindahl und I. Toplin. *Acta Chemica Scandinavia* **18** 1150–1156, 1964.

[138] B. Weida und S.J. Gill. *Biochimica Biophysica Acta* **112** 179–181, 1966.

[139] E. Nordmeier. *The Journal of Physical Chemistry* **96** 1494–1501, 1992.

[140] M. C. Lin, P. Eid, P. T. T. Wong und R. B. Macgregor. *Biophysical Chemistry* **76** (2) 87–94, 1999.

[141] R. B. Macgregor. *Biopolymers* **48** (4) 253–263, 1998.

[142] R.B. Macgregor, J.Q. Wu und R. Najaf-Zadeh. In J. Markley, D.B. Northrop und C.A. Royer, (Eds.), *High Pressure Effects in Molecular Biophysics and Enzymology* 274–297. Oxford, New York, 1996.

[143] T. V. Chalikian und K. J. Breslauer. *Biopolymers* **48** (4) 264–280, 1998.

[144] A. Kumar. *Biochemistry* **34** (40) 12921–12925, 1995.

[145] D.K. Kambhampati. *Investigating Nucleic Acid Hybridization Interactions on 2D and 3D Sensor Surfaces Using Surface Plasmon Resonance and Fluorescence Spectroscopy.* Dissertation, 2001.

[146] B. Neumann und P. Pollmann. *Physical Chemistry Chemical Physics* **3** (20) 4508–4514, 2001.

[147] B. Neumann und P. Pollmann. *Physical Chemistry Chemical Physics* **3** (6) 943–951, 2001.

[148] J.M.L. Penninger, M. Radosz, M.A. McHugh und V.J. Krukonis. *Supercritical Fluid Technology.* Elsevier Science Publishers B.V. Amsterdam, 1985.

[149] E. Kirian und J.F. Brennecke, (Eds.). *Supercritical Fluid Engineering Science: Fundamentals and Applications* Band 514 von *ACS Sympsium Series.* American Chemical Society Washington D.C., 1993.

[150] G.M. Schneider, E. Stahl und G. Wilke. *Extraction with Supercritical Gases.* Verlag Chemie Weinheim, 1980.

[151] S.K. Moore. *Chemical Week*, , 1999.

[152] I.S. Liau und M.A. McHugh. In J.M.L. Penninger, M. Radosz, M.A. McHugh und V.J. Krukonis, (Eds.), *Supercritical Fluid Technology* 417–434. Elsevier Science Publishers B.V. Amsterdam, 1985.

[153] G. K. Fleming und W. J. Koros. *Macromolecules* **19** (8) 2285–2291, 1986.

[154] A.S. Michaels, W.R. Vieth und J.A. Barrie. *Journal of Applied Physics* **34**, 1, 1963.

[155] W.R. Vieth, H.H. Alcalay und A.J. Frabetti. *Journal of Applied Polymer Science* **8**, 2125, 1964.

[156] S. A. Stern und A. H. Demeringo. *Journal of Polymer Science Part B-Polymer Physics* **16** (4) 735–751, 1978.

[157] G. Morel und D. R. Paul. *Journal of Membrane Science* **10** (2-3) 273–282, 1982.

[158] W. J. Koros, G. N. Smith und V. Stannett. *Journal of Applied Polymer Science* **26** (1) 159–170, 1981.

[159] D.L. Canelas, D.E. Betts, J.M. DeSimone, M.Z. Yates und K.P. Johnston. *Macromolecules* **31** (6794), , 1998.

[160] M.L. O'Neill, M.Z. Yates, K.P. Johnston, C.D. Smith und S.P. Wilkinson. *Macromolecules* **31**, 2848, 1998.

[161] U. Fehrenbacher, O. Muth, T. Hirth und M. Ballauff. *Macromolecular Chemistry and Physics* **201** (13) 1532–1539, 2000.

[162] J.S. Ham, M.C. Bolen und J.K. Hughes. *Journal of Polymer Science* **57**, 25, 1962.

[163] D.H. Moffat und K.E. Weale. *Fuel* **34**, 449, 1955.

[164] A. Angus, B. Armstrong und K.M. DeReuck, (Eds.). *IUPAC: International Thermodynamic Table of Fluid State: Carbon Dioxide.* Pergamon Press Oxford, 1976.

[165] A. Michels und J. Hamers. *Physica IV* (10) 995–1006, 1937.

[166] E.P. Kholodov, N.I. Timoshenko und A.L. Yamnov. *Thermal Engineering* **19**, 126, 1972.

[167] J.M. St.-Arnaud und T.K. Bose. *Journal of Chemical Physics* **71**, 4951, 1979.

[168] W. B. Li, P. N. Segre, R. W. Gammon, J. V. Sengers und M. Lamvik. *Journal of Chemical Physics* **101** (6) 5058–5069, 1994.

[169] R.W. Galland. *Physical Properties of Hydrocarbons* Band 2. Gulf Publisher Houston, 1970.

[170] T. Sasuga und M. Takehisa. *Journal of Macromolecular Science-Chemistry* **A12** (9) 1321–1331, 1978.

[171] K.-H. Hellwege, W. Knappe und P. Lehmann. *Kolloid Zeitschrift* **183**, 110, 1962.

[172] J. Brandrup, E.H. Immergut und E.A. Grulke, (Eds.). *Polymer Handbook.* John Wiley & Sons, Inc. New York 4th edition, 1999.

[173] L. Spiccia und T.W. Swaddle. *Inorganic Chemistry* **26**, 2265, 1987.

[174] I.S. Crick und P.A. Tregloan. *Inorganic Chimica Acta* **142**, 291, 1988.

[175] B. E. Conway und J. C. Currie. *Journal of the Electrochemical Society* **125** (2) 252–257, 1978.

[176] B. E. Conway und J. C. Currie. *Journal of the Electrochemical Society* **125** (2) 257–264, 1978.

[177] M. T. Cruañes, H. G. Drickamer und L. R. Faulkner. *Journal of Physical Chemistry* **96** (24) 9888–9892, 1992.

[178] M. Fleischmann, W. B. Gara und G. J. Hills. *Journal of Electroanalytical Chemistry* **60** (3) 313–321, 1975.

[179] J. Sachinidis, R. D. Shalders und P. A. Tregloan. *Journal of Electroanalytical Chemistry* **327** (1-2) 219–234, 1992.

[180] W.A. Eaton, P. George und G.I.H. Hanania. *The Journal of Physical Chemistry* **71** (7) 2016–2021, 1967.

[181] P. Kulesza, T. Jędral und Z. Galus. *Journal of Electroanalytical Chemistry* **109** 141–149, 1980.

[182] E.L. Goldstein und M.R. Van de Mark. *Electrochimica Acta* **27** (8) 1079–1085, 1982.

[183] Internet Michigan State University. *http://poohbah.cem.msu.edu/courses/cem419/ cem372cyclicvoltammetry.pdf*, .

[184] P. Krasiński, M. Tkacz, B. Baranowski und Z. Galus. *Journal of Electroanalytical Chemistry* **308** (1-2) 189–202, 1991.

[185] J. Roncali. *Journal of Chemical Review* **92**, 711, 1992.

[186] J.L. Segura. *Acta Polymerica* **49**, 319, 1998.

[187] Z. Bao, Y. Feng, A. Dodabalapur, V.R. Raju und A.J. Lovinger. *Chemistry of Materials* **9**, 1299, 1997.

[188] K. Uehara, T. Ichikawa, T. Serikawa, S. Yoshikawa, S. Ehara und M. Tsunooka. *Thin Solid Films* **322**, 198, 1998.

[189] M. Kabasakaloglu, T. Kiyak, H. Toprak und M. L. Aksu. *Applied Surface Science* **152** (1-2) 115–125, 1999.

[190] D. Goncalves und E. A. Irene. *Langmuir* **17** (16) 5031–5038, 2001.

[191] B.D. Cahan, H.M. Villullas und E.B. Yaeger. *Journal of Electroanalytical Chemistry* **306**, 213, 1991.

[192] C. Visy, J. Kankare und E. Krivan. *Electrochimica Acta* **45** (22-23) 3851–3864, 2000.